Investigation of Functionally Graded Materials Developed by Wire Arc Additive Manufacturing Process Assisted by Friction Stir Processing

A Thesis submitted in the fulfilment of the requirements for the degree of

Doctor of Philosophy

in

Mechanical Engineering

Submitted by

Manish Singh

Registration No.: 951808001

Under the supervision of

Dr. Ratnesh Kumar Raj Singh

Associate Professor, MED

Prof. Dheeraj Gupta

Professor, MED

THAPAR INSTITUTE
OF ENGINEERING & TECHNOLOGY
(Deemed to be University)

DEPARTMENT OF MECHANICAL ENGINEERING,

THAPAR INSTITUTE OF ENGINEERING AND TECHNOLOGY, PATIALA-147004, INDIA

(DEEMED TO BE UNIVERSITY)

MARCH, 2024

Table of Contents

Table of Contents ii

Acknowledgement x

Abstract xi

List of Figures xiii

List of Tables xix

List of Abbreviations xx

Chapter 1 1

INTRODUCTION AND OVERVIEW 1

1.1 EVOLUTION OF FUNCTIONALLY GRADED MATERIAL 1

1.2 FUNCTIONALLY GRADED MATERIAL 2

1.3 CLASSIFICATIONS OF FGM 3

1.3.1 Classification According to Physical State 3

1.3.2 Classification According to Structural Gradient 4

1.3.3 Classification According to Area of Application 5

1.4 MANUFACTURING TECHNIQUES OF FGM 5

1.4.1 Additive Manufacturing 6

1.4.1.1 Advantages of Additive Manufacturing 7

1.4.1.2 Limitations of AM 8

1.5 METAL ADDITIVE MANUFACTURING 9

1.5.1 Classification of Metal AM Based on Material Feed System....9

1.5.1.1 Powder Bed AM....9
1.5.1.2 Powder Feed AM....9
1.5.1.3 Wire Feed AM....10

1.5.2 Classification of Metal AM Based on Energy Source....10

1.5.2.1 Laser AM Techniques for Metal FGMs....10
1.5.2.2 Electron Beam Based Additive Manufacturing for Metal FGMs....11
1.5.2.3 Arc Based Additive Manufacturing of Metal FGMs....12

1.6 POST PROCESSING TREATMENT....13

1.7 THESIS OUTLINE....14

Chapter 2....16

LITERATURE REVIEW AND PROBLEM FORMULATION....16

2.1 FGM DEVELOPMENT....16

2.2 TYPES OF FGMs....17

2.3 APPLICATIONS OF METAL BASED FGMs....19

2.4 FABRICATION OF METAL BASED FGMs....22

2.5 WIRE ARC ADDITIVE MANUFACTURING....23

2.5.1 Classification of Wire Arc Additive Manufacturing....24

2.6 GTAW BASED WAAM....25

2.6.1 GTAW Process Parameters and Their Effects....27

2.6.1.1 Shielding Gas Flow Rate Control....29
2.6.1.2 Weld Pool Control....29

2.7 METAL USED IN WAAM....30

2.8 TYPES OF SUPER ALLOYS USED FOR DEVELOPMENT OF FGM....31

2.8.1 Ni-Fe-based Superalloys....31
2.8.2 Co-based Superalloys....31
2.8.3 Ni-based Superalloys....31
2.9 TYPES OF Ni BASED SUPERALLOYS....32
2.9.1 Inconel 625....32
2.9.2 Inconel 718....33
2.9.3 ERNiCr-Mo-10....34
2.10 DEVELOPMENT OF METAL BASED FGMs USING WAAM....34
2.11 Challenges in WAAM Fabricated Components....40
2.11.1 Post Processing Treatment in WAAM....41
2.12 Friction Stir Processing....45
2.12.1 Advantages of FSP....45
2.13 RESEARCH GAPS AND PROBLEM FORMULATION....46
2.14 RESEARCH OBJECTIVES....46
2.15 METHODOLOGY....47
SUMMARY....48
Chapter 3....49
MATERIAL SELECTION AND THEIR CHARACTERIZATIONS....49
3.1 SELECTION OF MATERIALS....49
3.1.1 Inconel 625....49
3.1.2 ERNiCrMo-10....49

3.1.3 Nichrome 80:20 50

3.1.4 Pure Nickel 50

3.1.5 Selection of Substrate Material 50

3.2 CHARACTERIZATION TECHNIQUES 51

3.2.1 Metallurgical Characterization 51

3.2.1.1 Optical Microscopy 51
3.2.1.2 Scanning Electron Microscopy 51
3.2.1.3 Electron Backscatter Diffraction 52
3.2.1.4 X-Ray Diffraction 52
3.2.1.5 Residual Stress Measurement by using X-Ray Diffraction 53

3.2.2 Mechanical Characterization 54

3.2.2.1 Vicker's Microhardness Test 54
3.2.2.2 Tensile Test 54

3.3 CHARACTERIZATION OF THE MATERIALS 55

3.3.1 Characterization of Raw Material 55

3.3.2 FGM Characterization 56

SUMMARY 56

Chapter 4 57

EXPERIMENTAL PROCEDURE AND FEASIBILITY FOR FGM DEVELOPMENT 57

4.1 EXPERIMENTAL SETUP 57

4.1.1 WAAM Setup 57

4.1.2 FSP Setup 58

4.2 PROCESS PARAMETERS OPTIMIZATION 59

4.2.1 Gas Tungsten Arc Welding Parametric Investigation 59

4.2.2 Friction Stir Process Parametric Investigation 61

4.3 FGM SAMPLE PREPARATION STRATEGY 64

4.3.1 FGM Type-I: FGM by varying Ni and Cr Elements along the Deposition 65

4.3.2 FGM type-II: FGM by varying Ni, Cr and Mo Elements along the Deposition 67

4.4 DEVELOPMENT OF FGM 67

4.4.1 Development of FGM by GTAW WAAM Process without FSP and with FSP 67

4.4.2 Development of FGM by GTAW-WAAM Process with FSP and Different Cooling Environment 68

SUMMARY 69

Chapter 5 70

METALLURGICAL AND MECHANICAL CHARACTERIZATION OF DEVELOPED FGMs AT OPTIMIZED PARAMETERS AND CONDITIONS 70

5.1 METALLURGICAL CHARACTERIZATION OF FGM TYPE- I 70

5.1.1 Microstructural Investigation (OM/SEM) 71

5.1.2 EDS Analysis 73

5.1.3 EBSD Analysis 75

5.1.4 XRD Analysis 76

5.2 MECHANICAL CHARACTERIZATION 77

5.2.1 Vicker's Microhardness Investigation 77

5.2.2 Tensile Strength Assessment 79

5.3 METALLURGICAL CHARACTERIZATION OF FGM TYPE-II 81

5.3.1 Microstructural Investigation (OM and Grain Size) 81

5.3.2 SEM Analysis 83

5.3.3 EDS Analysis 85

5.3.4 XRD Analysis 87

5.4 MECHANICAL CHARACTERIZATION OF FGM TYPE-II 88

5.4.1 Vicker's Microhardness Investigation 88

5.4.2 Tensile Strength Assessment 90

SUMMARY 92

Chapter 6 93

DEVELOPMENT OF TRIMETALLIC FGMS BY USING GMAW AND THEIR CHARACTERIZATIONS 93

6.1 INTRODUCTION 93

6.2 EXPERIMENTAL SETUP OF GMAW-WAAM 93

6.3 FGM SAMPLE PREPARATION STRATEGY 94

6.4 DEVELOPMENT OF TRIMETALLIC FGMs 95

6.5 METALLURGICAL CHARACTERIZATION 96

6.5.1 Microstructural Investigation (OM/SEM) 96

6.5.2 EBSD Analysis 99

6.5.3 EDS Analysis 100

6.5.4 Temperature Profile 101

6.6 MECHANICAL CHARACTERIZATION 102
6.6.1 Vicker's Microhardness Investigation 102
6.6.2 Tensile Strength Assessment 104
6.6.2.1 Fracture Surfaces of Tensile Sample 106
SUMMARY 106
Chapter 7 108
CONCLUSIONS AND RECOMMENDATIONS OF FUTURE WORK 108
7.1 CONCLUSIONS 108
7.1.1 The Findings from FGM Type-I 108
7.1.2 The Findings from FGM Type-II 109
7.1.3 The Findings from Trimetallic FGM: 110
7.2 FUTURE SCOPE 111
REFERENCES 112
VISIBLE RESEARCH OUTPUT 123
APPENDIX 124

Declaration

I, **Manish Singh**, Roll no. 951808001, hereby declare that the thesis entitled "**Investigation of Functionally Graded Materials Developed by Wire Arc Additive Manufacturing Process Assisted by Friction Stir Processing**" submitted to the Department of Mechanical Engineering at Thapar Institute of Engineering & Technology, Patiala for the award of the degree of Doctor of Philosophy in Mechanical Engineering is a record of original bonafide research work carried out by me under the supervision of **Dr. Ratnesh Kumar Raj Singh** and **Prof. Dheeraj Gupta**. All the requirements for the submission of this thesis have been fulfilled as per institute norms. No part of the matter embodied in this report has been submitted to any other university or institute for the award of any degree.

Date: 12-03-2024

Manish Singh
Roll no. 951808001

It is certified that the above statement made by the student is correct to the best of our knowledge and belief.

Dr. Ratnesh Kumar Raj Singh
Associate Professor
Mechanical Engineering Department
TIET, Patiala-147004, India

Prof. Dheeraj Gupta
Professor
Mechanical Engineering Department
TIET, Patiala-147004, India

Acknowledgement

First of all, I would like to express my gratitude to my supervisors Dr. Ratnesh Kumar Raj Singh, Associate Professor, Mechanical Engineering Department, Thapar Institute of Engineering and Technology, Patiala and Prof. Dheeraj Gupta, Professor, Mechanical Engineering Department, Thapar Institute of Engineering and Technology, Patiala for their invaluable guidance, moral support and encouragement during the entire period of this research which cannot adequately be expressed in words in this acknowledgement.

I would like to extend my acknowledgment to my doctoral committee member Dr. Tarun Kumar Bera (Head, Department of Mechanical Engineering), Dr. Ratnesh Kumar Raj Singh, Prof. Dheeraj Gupta, Prof. Vivek Jain, Dr. Vishal Gupta and Prof. Haripada Bhunia for their valuable observations, suggestions, and feedback. I am very much grateful to my friends Dr. Mandeep Kumar, Mr. Parveen Kumar, Mr. Hemant Kaundal, Mr. Khalid Bashir and Mr. Avtar Singh for their help and support.

I would like to thank my parents, Sh. Yadvendra Singh and Smt. Satyawati Singh whose consistent love and support motivated me throughout the period of research. I would also like to thank my brother, Mr. Ashish Singh for her understanding, patience and valuable support which helped me in achieving the goal.

Special thanks to my wife Mrs. Sonal Singh for her understanding and support during the entire period of research program. Special thanks to my daughter Adwika Singh who was the source of my motivation.

Above all, I thank almighty whose blessings have enabled me to accomplish this research work.

Manish Singh

Abstract

The demand of advanced materials is growing in a very steeped manner, especially in the engineering sectors like, aerospace, nuclear, automobile and power generation. The materials of these components are required to serve in harsh working conditions. The working life of such industrial components are very important and possibilities of catastrophic failures of these components cannot be accepted in such sectors. The development of materials for these applications, is very time consuming and costly process. Hence, functionally gradient materials (FGM) can be one of the possible solutions. Many additive manufacturing (AM) has applied to fabricate bulk metal based FGM. However, wire arc additive manufacturing would be one of the most prominent and economical fabrication methods.

In this work, Ni-based FGMs specific alloys such as Inconel 625, ERNiCrMo-10, Nichrome 80/20, and pure Ni weld spools were selected as a raw material. The development of Ni-Cr-Mo-based functionally graded materials (FGMs) was carried out by using gas tungsten arc welding (GTAW) based wire and arc additive manufacturing (WAAM) process. The GTAW process parameters for FGMs were optimized to get good weld bead geometry. The optimized process parameters are used for further development of FGMs. The post treatment of developed FGMs were also carried out by using innovative approach of friction stir processing (FSP). This post treatment is mainly intended for mitigation of developed stresses during FGMs development and maintained the material homogeneity in the FGMs structure. The FSP process parameters has been optimized and based on the observations, rotation speed is the most influencing parameter to control the intentions. The effect of water cooling is also investigated on the developed FGMs. The developed FGMs were investigated in detailed by using various metallurgical and mechanical tools and techniques. The microstructural evolution of FGMs produced through WAAM, observing a combination of dendritic and columnar grains in the as-deposited samples. Through, FSP post-processing, these structures transform into fine recrystallized grains with oriented deformation direction after FSP. It also affects the distribution of $CrNi_3$ and $MoNi_4$ precipitates. The microhardness gradually increases from the bottom to top of the samples in the as-deposited state. The FSP processed samples shown significant improvement in the microhardness. The investigations reveal variations in tensile strength along the gradient direction of the FGMs, with increasing Cr and Mo content correlating with higher tensile strength and microhardness.

Further, the trimetallic FGMs using stainless steel (ER316L), duplex steel (ER2205), and Inconel 718 (IN718) via gas metal arc welding (GMAW) based WAAM has been also investigated. The metallurgical examinations uncover distinct boundaries between different alloy compositions and the presence of metal carbides and Lave phases. The mechanical characterization of these FGMs demonstrates a steady increase in hardness along the built direction, with variations at alloy interfaces. The tensile tests reveal increased tensile strength along the built direction, accompanied by reduced strain.

Keywords: Additive Manufacturing, Wire Arc Additive Manufacturing, Friction Stir Processing, Functionally Graded Material, Characterisation.

List of Figures

Figure 1.1: Development of engineering materials from pure metal to towards FGM [1].....2

Figure 1.2: Natural example of FGMs contain structures with the graded properties [13].....2

Figure 1.3: Classification of FGMs according to state during manufacturing [16].....3

Figure 1.4: Schematic diagrams illustrating: (a) Continuous graded and (b) discontinuous (stepwise) graded FGMs.....4

Figure 1.5: Schematic diagrams illustrating: (a) discontinuous FGMs and (b) continuous FGMs, (c), (d) and (e) schematic diagrams showing discontinuous FGMs that contain interfaces with gradual change in composition, grain orientation and volume fractions, respectively, (f), (g) and (h) schematic diagrams showing continuous FGMs in absence of interfaces and with gradual change in grain size, fibre orientation and volume fraction of second-phase particles [8].....4

Figure 1.6: Functionally graded materials: fields of application and examples [24].....5

Figure 1.7: Various manufacturing techniques of FGM [27].....6

Figure 1.8: Schematic diagrams showing (a) powder bed systems, (b) powder feed systems, and (c) wire feed systems [31].....10

Figure 1.9: Schematic diagram of laser based metal AM process [32].....11

Figure 1.10: (a) Schematic of the of electron beam based metal AM, (b) Schematic diagram of Mo–Mo + TiC–Mo sandwich FGM sample [33].....12

Figure 1.11: (a) six-axis welding robot and (b) deposition system retrofitted onto former friction stir welding machine[38].....13

Figure 1.12: Post processing techniques (a) interpass cold rolling, (b) machine hammer peening (MHP), (c) heat treatments (d) different rolling methods, and (e) interpass rolling [42-45]...14

Figure 2.1: Historical overview of relevant milestones in the research and development of FGMs [49].....17

Figure 2.2: Possible material combinations used in FGMs [50].....17

Figure 2.3: Depicts a finite element model of automobile valve made of 304L stainless steel stems connected to an Inconel 625 valve with (a) graded composition and (b) sharp interface joined by friction stir welding (FSW) [52] 19

Figure 2.4: Schematic cross sectional view showing (a) conventionally designed dissimilar metal welded joining, and (b) functionally graded additively manufactured joint [58] 20

Figure 2.5: Applications of functionally graded materials in aerospace sector [59] 21

Figure 2.6: Applications of functionally graded materials in automotive sector [62] 22

Figure 2.7: Schematic diagram of the (a) GMAW, (b) GTAW, and (c) PAW process [75-77] 25

Figure 2.8: Integrated GTAW-AM process 26

Figure 2.9: (a) depicts the variations in weld-bead size corresponding to changes in welding current (b)) illustrates the relationship between weld size and welding speed [87] 29

Figure 2.10: Microstructure of Inconel 625 (a) conventional manufacturing process and (b) DED process[102] 33

Figure 2.11: Inconel 718 microstructure (a) conventional and (b) DED manufacturing process[105] 33

Figure 2.12: EBSD image of inverse pole map for (a) As-built, (b) H10, and (c) H60, All EBSD results were analysed based on the 8 μm step size [123] 42

Figure 2.13: (a) Schematic diagram of hybrid forced interpass cooling assisted WAAM, (b) WAAM fabricated wall at different processing condition and (c) average hardness [42] 43

Figure 2.14: (a) Schematic diagram of hybrid interpass rolling assisted WAAM, inverse pole figure β orientation maps of Hybrid WAAM fabricated Ti-6Al-4V (b) as build and (c) with cold rolling applied between every deposited layer [45] 44

Figure 2.15: (a) Schematic diagram of hybrid machine hammer peening assisted WAAM, inverse pole figure maps of Hybrid WAAM fabricated Ti-6Al-4V (b) as build and (c) with MHP applied between every deposited layer [125] 44

Figure 2.16: Friction stirs processing technique 45

Figure 2.17: Proposed research methodology used in the present research work 48

Figure 3.1: Schematic diagram showing the position of sample with reference to XRD detector at (a) ψ = 0. (b) ψ = ψ (sample rotated through some known angle ψ) (D = x-ray detector, S = x-ray source and N = normal to the surface).....53

Figure 3.2: Tensile sample dimensions according to ASTM E8M standard 55

Figure 4.1: (a) schematic representation of GTAW based WAAM set up, and (b) AC/DC GTAW welding machine 58

Figure 4.2: The details of FSP setup showing; (a) FSP, (b) vertical milling machine and (c) tool used 58

Figure 4.3: illustrates the key steps of this process.....59

Figure 4.4: GTAW deposited single layer samples at different welding parameters and their cross-sectional view 60

Figure 4.5: FSP processed sample at different rpm; (S1- 350, S2- 560, S3- 710, S4- 900, and S5-1120) with a constant feed of 100 mm/min.....62

Figure 4.6: Average grain size (μm) of as-deposited and FSP samples (S1-350 rpm, S2-560 rpm, S3-710 rpm, S4-900 rpm and S5-1120 rpm) 62

Figure 4.7: (a) samples with and without FSP, and (b) cross sectional view and (c) Sample height before and after 63

Figure 4.8: Hardness of as deposited with and without FSP and (b) Residual stress of as deposited with and without FSP 64

Figure 4.9: Developed FGM type-I sample in two different processing condition (a) as deposited condition and (b) as deposited with FSP condition 68

Figure 4.10: Developed FGM type-II sample in two different processing condition (a) as deposited condition, (b) FSP condition and (c) FSP-W condition.....69

Figure 5.1: (a) Cross-sections of developed FGM showing examination locations, and (b) the sample extraction locations for metallurgical examination and tensile testing 70

Figure 5.2: Microstructure evolution of as-deposited sample showing (a) cross sectional view, and microstructure at (b) location-1, (c) location-2, (d) location-3, and (e) location-4.....71

Figure 5.3: Microstructure evolution of FSP sample showing (a) cross sectional view, and microstructure at (b) location-1, (c) location-2, (d) location-3, and (e) location-4 72

Figure 5.4: SEM micrograph of (a) as-deposited (b) as-deposited with FSP samples 72

Figure 5.5: EDS analysis at location-1 showing (a) SEM of the deposited sample (b) EDS mapping, (c) EDS spectra, (d) distribution of Ni, (e) distribution of Cr and (f) distribution of Mo 74

Figure 5.6: EDS analysis at location-2 showing (a) SEM of the deposited sample (b) EDS mapping, (c) EDS spectra, (d) distribution of Ni, (e) distribution of Cr and (f) distribution of Mo 74

Figure 5.7: EDS analysis at location-3 showing (a) SEM of the deposited sample (b) EDS mapping, (c) EDS spectra, (d) distribution of Ni, (e) distribution of Cr and (f) distribution of Mo 74

Figure 5. 8: % of alloying elements in (a) as-deposited and (b) FSP sample 75

Figure 5.9: EBSD analysis of (a) as-deposited, (b) FSP, misorientation in (c) as-deposited and (d) FSP samples 76

Figure 5.10: The XRD spectra of (a) as-deposited and (b) FSP samples 77

Figure 5.11: Location of microhardness measurement in (a) as deposited and (b) FSP samples 78

Figure 5.12: (a) Vicker's microhardness profile along the deposition direction, and (b) average microhardness at different locations 78

Figure 5.13: (a) Dimension of tensile sample and (b) fabricated tensile sample before testing and (c) fabricated tensile sample after testing.....79

Figure 5.14: Stress-strain curves of as-deposited sample at (a) location-1, (b) location-2 and (c) location-3 and FSP sample at (d) location-1, (e) location-2, and (c) location-3.....80

Figure 5.15: (a) The sample extraction locations for microstructural examination and tensile testing, and (b) cross-sections of developed FGM showing examination locations.....81

Figure 5.16: Macro and microstructure evolution of (a) As-deposited, (b) FSP and (c) FSP-W 82

Figure 5.17: (a) Average grain size distribution and (b) nature of grains (%).....83

Figure 5.18: Microstructure of (a) as deposited, (b) FSP, (c) FSP-W samples (d) precipitates distribution in deposited material (e) precipitates at higher magnification and (f) elemental mapping.....84

Figure 5.19: (a) Macrostructure of the deposited sample, (b) SEM of the deposited sample (c) EDS mapping, (d) variation of Ni, (e) variation of Cr and (f) variation of Mo.....86

Figure 5.20: (a) Macrostructure of FSP sample, (b) SEM of FSP sample, (c) EDS mapping, (d) variation of Ni, (e) variation of Cr and (f) variation of Mo.....86

Figure 5.21: (a) Macrostructure of FSP-W sample, (b) SEM of FSP-W sample, (c) EDS mapping, (d) variation of Ni, (e) variation of Cr and (f) variation of Mo.....87

Figure 5.22: The XRD spectra of (a) as-deposited, (b) FSP and (c) FSP-W.....88

Figure 5.23: Microhardness distribution along the deposition direction from the substrate to the top layer, (a) as deposited, (b) FSP, (c) FSP-W.....89

Figure 5.24: Average microhardness at (a) location-1, (b) location-2 and (c) location-3.....89

Figure 5.25: Stress-Strain diagram along the deposition direction from substrate to the top layer (a) as deposited, (b) FSP, (c) FSP-W.....90

Figure 5.26: Fracture surface of tensile sample at low magnification in (a) as-deposited, (b) FSP, (c) FSP-W and at high magnification (d) as-deposited, (e) FSP and (f) FSP-W.....91

Figure 6.1: (a) Schematic representation of GMAW-WAAM setup, and (b) GMAW-WAAM machine.....94

Figure 6. 2: GMAW-WAAM deposited trimetallic FGM sample.....95

Figure 6.3: (a) schematic diagram of specimen extraction, (b) tensile test specimen and (c) dimensions of tensile sample.....96

Figure 6.4: (a) Fabricated trimetallic FGM sample, Microstructure at different location (b and c) ER316L zone, (d and e) ER2205 zone and (f and g) IN718 zone.....98

Figure 6.5: (a) Trimetallic FGM sample showing the location of microstructural evaluation at (b) ER316L, (c) the interface of ER316L and ER2205, (d) ER2205, (e) the interface of ER2205 and IN718, (f) IN718, and (g) magnified microstructure of IN718.....98

Figure 6.6: EBSD micrograph of (a) ER2205-IN718 interface, (b) colour contrast, (c) grain boundary map and (d) misorientation angle v/s number of fraction histogram.....99

Figure 6.7: EDS mapping of IN718: (a) SEM image showing precipitates and Laves phase (b) mapping of the element, (c) EDS element peaks and individual mapping of elements (d) titanium, (e) chromium, (f) iron, (g) nickel, (h) niobium, and (i) molybdenum.....100

Figure 6.8: EDS mapping at ER2205-IN718 interface zone: (a) SEM image, (b) mapping of the element, (c) EDS element peaks of (d) chromium, (e) iron and (f) nickel 101

Figure 6.9: (a) Schematic representation of location of thermocouple during fabrication of FGM and (b) temperature profile.....102

Figure 6.10: Microhardness profile along the built direction, (b) location of hardness reading, (c) line mapping, (d) location of line mapping and (e) principal alloying element profile ...103

Figure 6.11: Hardness at the interface of ER2205-IN718 103

Figure 6.12: Stress-strain curve of (a) ER316L, (b) ER2205, (c) IN718, (d) along the built direction, and (e) maximum tensile strength and % strain along the built direction and (f) tensile samples before and after test.....105

Figure 6.13: Fracture surfaces of tensile samples across the built direction of (a) IN718, (b) ER2205, (c) ER316L and (d) fracture surfaces of tensile samples along the built direction 106

Figure A-1 Optical Microscopy (Make: Radical Scientific Equipment, Model: RMM-8T, Photo Courtesy: Surface Engineering and Tribology Research Lab, Mechanical Engineering Department, TIET, Patiala).....124

Figure A-2 Scanning Electron Microscopy (Make: Sigma - ZEISS Field Emission SEM, Photo Courtesy: Electron Microscopy laboratory, TIET, Patiala).....124

Figure A-3 X-Ray Diffractometer (XRD) (Make: SmartLab Rigaku, Japan, Model: SmartLab SE, Photo Courtesy: School of Physics and Materials Science, Thapar Institute of Engineering & Technology).....125

Figure A-4 Vickers Micro-Hardness Tester (Make: Meta-Tech, Model: MVH1) Photo Courtesy: A.M. Lab, Thapar Institute of Engineering & Technology) 126

Figure A-5 Universal testing machine (Make: Enkay Enterprises, Model: EKE591 Series) Photo Courtesy: A.M. Lab, Thapar Institute of Engineering & Technology).....126

List of Tables

Table 2.1: Comparison of various WAAM techniques [40]. 24

Table 2.2: Metals used with WAAM process under different industrial applications [94] 30

Table 2.3: Research work carried out in the field of WAAM process 36

Table 2.4: Common defect associated with WAAM fabrication [40, 94, 123] 40

Table 3.1: Percentage composition of alloying element of filler wires 55

Table 3.2: Mechanical properties of wire spools 55

Table 4.1: Specifications of the vertical milling machine 58

Table 4.2: Selected Parameters for deposition of material for fabrication of FGM. 60

Table 4.3: Friction stir processing parameters and their values 62

Table 4.4: Combination of wire and calculated compositions of each layer 66

Table 4.5: Combination of wire and calculated compositions of each layer 67

Table 5.1: Comparison of mechanical properties of fabricated sample with published research articles data 79

Table 6.1: Chemical compositions of wire spool 94

Table 6.2: Mechanical properties of wire spool 94

Table 6.3: Welding parameters for fabrication of FGM 95

Table 6.4: Comparisons of tensile properties of trimetallic FGM with feedstock wire 105

List of Abbreviations

Abbreviate		Full form
AM	=	Additive Manufacturing
ALM	=	Additive Layer Manufacturing
AC	=	Alternating Current
CVD	=	Chemical Vapor Deposition
Cr	=	Chromium
CMT	=	Cold Metal Transfer
CAD	=	Computer Aided Design
DC	=	Direct Current
DLMD	=	Direct Laser Metal Deposition
DED	=	Directed Energy Deposition
DMWs	=	Dissimilar Metal Welds
EBF	=	Electron Beam Formation
EBSM	=	Electron Beam Selective Melting
EDXS	=	Energy Dispersive X-Ray Spectroscopy
EBM	=	Electron Beam Melting
FSP	=	Friction Stir Processing
FSP-W	=	Friction Stir Processing- water
FGM	=	Functionally Graded Material
FCC	=	Face-Centered Cubic
GTAW	=	Gas Tungsten Arc Welding
GMAW	=	Gas Metal Arc Welding
HEA	=	High Entropy Alloy
ITS	=	Iso-Variable Transition Strategy
ICDD	=	International Centre for Diffraction Data
IPF	=	Inverse Pole Figure
LWRs	=	Light Water Reactors
LMD	=	Laser Metal Deposition
LENS	=	Laser-Engineered Net Shaping
LC	=	Laser Cladding

LPBF	=	Laser Powder Bed Fusion
MS	=	Mild Steel
MIG	=	Metal Inert Gas
MHP	=	Machine Hammer Peening
MC	=	Metal Carbide
Mo	=	Molybdenum
Ni	=	Nickel
OM	=	Optical Microscope
OTS	=	Optimized Transition Strategy
PM	=	Powder Metallurgy
PVD	=	Physical Vapor Deposition
PAW	=	Plasma Arc Welding
RPV	=	Reactor Pressure Vessel
(SFF)	=	Solid Free-Form Fabrication
SLS	=	Selective Laser Sintering
SEM	=	Scanning Electron Microscopy
SMAW	=	Shielded Metal Arc Welding
SMAW	=	Submerged Arc Welding
SOD	=	Standoff Distance
SPE	=	Solid Particle Erosion
SS	=	Stainless Steel
T-WAAM	=	Twin-Wire Arc Additive Manufacturing
TEM	=	Transmission Electron Microscopy
TIG	=	Tungsten Inert Gas
TMP	=	Thermo Mechanical Processing
UTM	=	Universal Testing Machine
TBC	=	Thermal Barrier Coatings
UTM	=	Universal Testing Machine
WAAM	=	Wire Arc Additive Manufacturing
XRD	=	X-ray Diffraction

Chapter 1

INTRODUCTION AND OVERVIEW

Functionally graded material (FGM) is a heterogeneous material that exhibits a gradual variation in composition and/or microstructure, resulting in tailored mechanical, thermal, electrical, and optical properties. Their versatility and adaptability allow precise customization to meet specific performance requirements, addressing challenges like thermal stress and interface compatibility. Compared to regular alloys, FGMs allow for smoother load transfer across interfaces, which lowers stress concentrations and improves reliability. In addition, they eliminate the problems associated with mismatches in thermal expansion coefficients. Additionally, FGMs are better than traditional composites because they allow a smooth transition between different phases. Thus, FGMs emerge as promising alternatives to alloys and composites in various engineering applications.

1.1 EVOLUTION OF FUNCTIONALLY GRADED MATERIAL

The pure metals are inherently soft and weak, which causes restriction of their use in wider engineering applications. To improve the suitability of a material for some particular applications, metals are often alloyed with other metals or nonmetals in their molten state. However, owing to thermodynamic equilibrium constraints, a material can only dissolve to a limited extent in solution with another material [1]. To address this issue, researchers have developed powder metallurgy (PM) techniques that mixes and matches alloying elements in a various proportion. This approach facilitates the creation of components with desired properties [2]. However, despite these advantages, powder metallurgy cannot be used to manufacture intricate shapes/structures. Consequently, a new class of materials has emerged to address this issue, namely composite materials [3]. A composite material is formed by the amalgamation of one or more solid-state materials, resulting in unique physical and chemical properties distinct from those of its components. These composites often demonstrate one of the important benefits such as an enhanced strength-to-weight ratio [4]. Despite their numerous advantages, composite materials have sharp interfaces that can lead to fiber delamination from the matrix under harsh working conditions (high stress and high temperatures) [5]. The researchers have developed FGMs to address these challenges by replacing sharp interfaces with gradient

interfaces [6, 7]. The FGMs are engineered materials intentionally formed to have a progressive change in composition or structure in one or more directions that result in a gradual change in properties which can be tailored for enhanced performance [8]. The visual representation in Figure 1.1 showcases the historical evolution from pure metal to functionally graded metals.

Figure 1.1: Development of engineering materials from pure metal to towards FGM [1]

1.2 FUNCTIONALLY GRADED MATERIAL

Functionally graded materials are heterogeneous materials characterized by a gradual variation in mechanical and physical properties over volume. It can be achieved by incorporating gradual changes in composition or structure within a single component. This unique feature allows FGMs to exhibit varying mechanical, thermal, and tribological characteristics in specific regions, rendering them adaptable for numerous applications [9]. Therefore, it is used for corrosion-resistant, wear-resistant and thermal barrier coatings, which are applicable in defense [10, 11], aerospace, nuclear, electromagnetic, and photoelectric engineering fields [12].

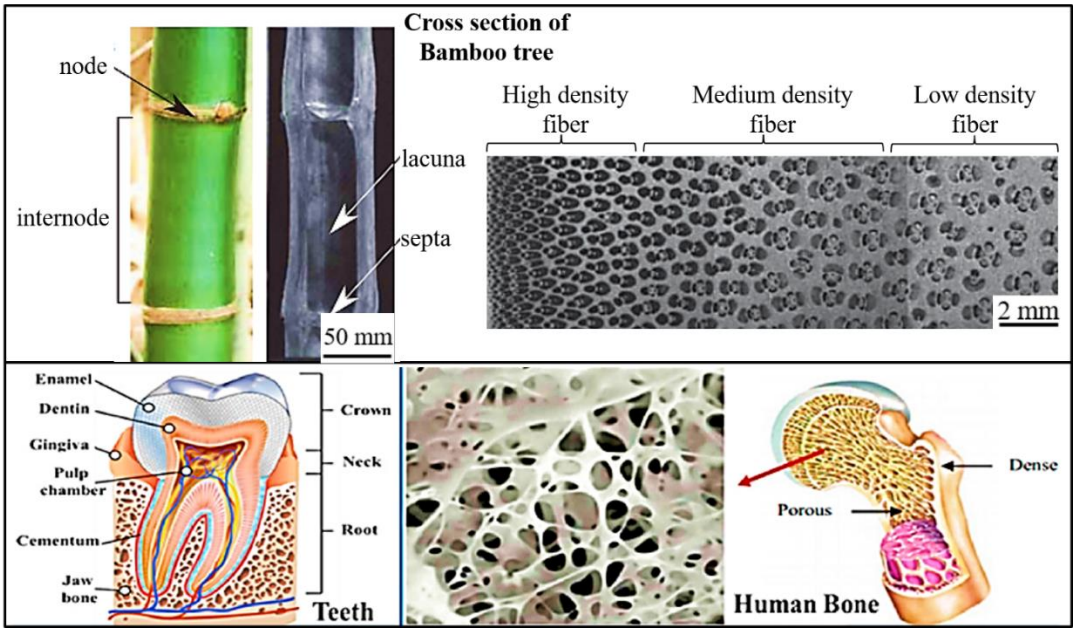

Figure 1.2: Natural example of FGMs contain structures with the graded properties [13]

The concept of structures with graded properties is not novel, finding parallels in nature provides compelling examples. Natural instances of functionally graded structures are abundant, with human body parts such as bones, teeth, and skin serving as crucial examples. These biological components exhibit gradation in properties, encompassing hardness and ductility. Additionally, bio-tissues of animals and trees further exemplify the inherent concept of functionally graded structures in nature [14, 15]. The Figure 1.2 illustrate natural examples and engineering applications that benefit from smooth-graded properties in FGMs.

1.3 CLASSIFICATIONS OF FGM

1.3.1 Classification According to Physical State

FGM processing methods can be broadly categorized into solid-state, liquid-state, and deposition processes. The Figure 1.3 enumerates various processing methods falling under these classifications. Extensive research has been conducted across different FGM production techniques covering all processing states. The deposition methods, characterized by high precision, are employed for the fabrication of small and intricately detailed products. On the other hand, liquid-state processes are typically employed for more oversized products, where precise property control is of relatively lower priority. The solid-state-based FGMs find application in producing thermo-mechanical components subjected to high-stress conditions [16].

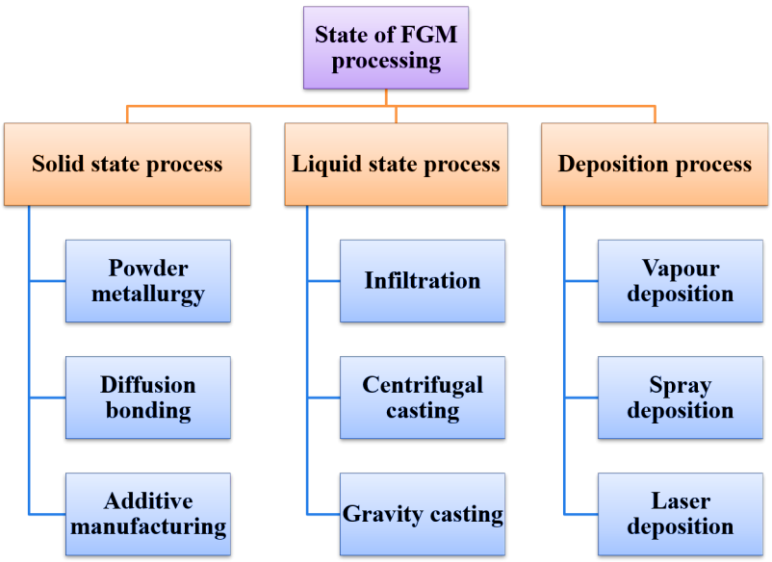

Figure 1.3: Classification of FGMs according to state during manufacturing [17]

1.3.2 Classification According to Structural Gradient

FGMs are categorized into two groups based on a structural gradient, continuous and discontinuous as shown in Figure 1.4. In the continuous structural gradient (Figure 1.4a), the absence of clear, distinct zones/interfaces within the material hinders the differentiation of properties in each zone so that continuously graded properties can be achieved. In the second group, material ingredients undergo a discontinuous stepwise gradation (Figure 1.4b), called layered or discrete FGM [18]. The continuous and discrete classifications can be further delineated into three types: composition gradient, orientation gradient, and fraction gradient.

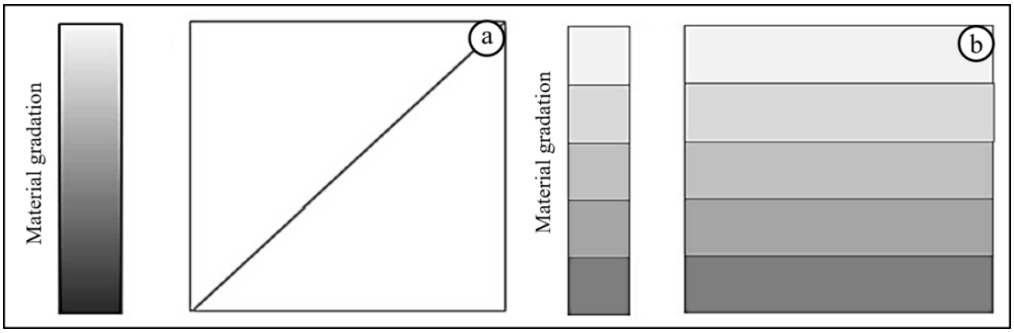

Figure 1.4: Schematic diagrams illustrating: (a) Continuous graded and (b) discontinuous (stepwise) graded FGMs [18]

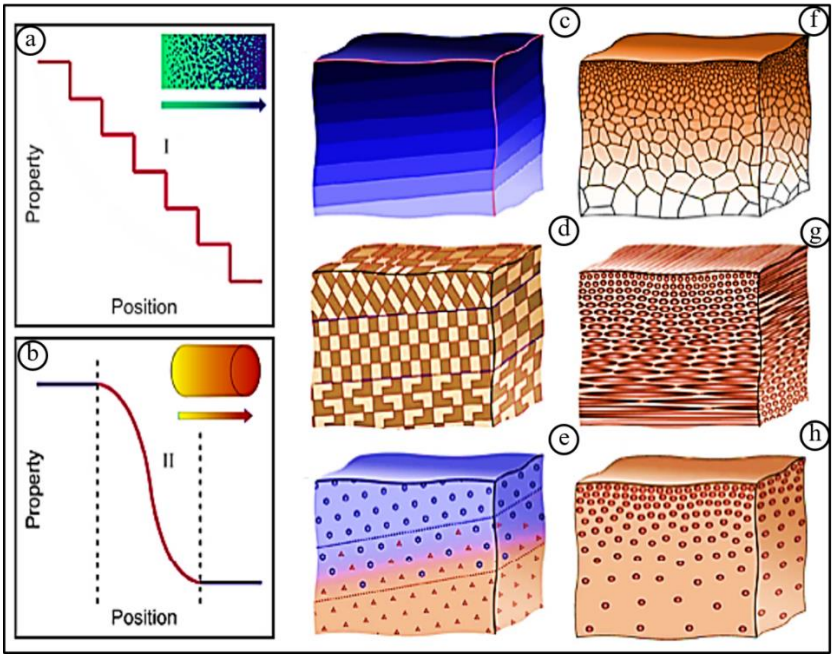

Figure 1.5: Schematic diagrams illustrating: (a) discontinuous FGMs and (b) continuous FGMs, (c), (d) and (e) schematic diagrams showing discontinuous FGMs that contain

interfaces with gradual change in composition, grain orientation and volume fractions, respectively, (f), (g) and (h) schematic diagrams showing continuous FGMs in absence of interfaces and with gradual change in grain size, fibre orientation and volume fraction of second-phase particles [8]

The Figure 1.5 (a), (c), (d) and (e) schematic diagrams showing discontinuous FGMs that contain interfaces with gradual change in composition, grain orientation and volume fractions, respectively while as Figure 1.5 (b), (f), (g) and (h) showing continuous FGMs in absence of interfaces and with gradual change in grain size, fibre orientation and volume fraction of second-phase particles.

1.3.3 Classification According to Area of Application

As outlined in the previous section, FGMs have been identified and utilized in various applications characterized by severe operating conditions or susceptible requirements. The broad examples encompass, heat exchangers, heat-resisting elements in spacecraft, fusion reactors, and biomedical implants [19]. The diverse combinations of typically incompatible functions can be harnessed to create novel materials applicable in aerospace, chemical plants, nuclear energy reactors, and other domains [20]. Based on their areas of application, FGMs can be categorized into biomaterials [21], aerospace materials, automotive components [22], defence applications [23], cutting tools, nuclear reactor components [24], smart structures [6], turbine blades, and sports equipment [9]. The Figure 1.6 provides an overview of the classification according to the major fields of applications.

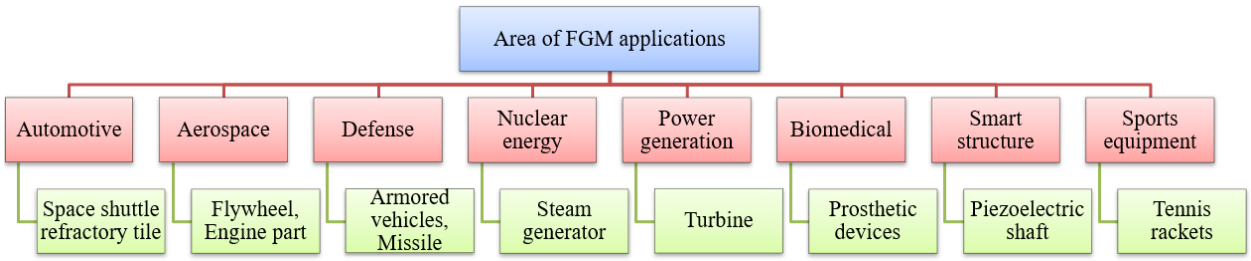

Figure 1.6: Functionally graded materials: fields of application and examples [25]

1.4 MANUFACTURING TECHNIQUES OF FGM

Various techniques have been used to fabricate FGM, such as powder metallurgy, chemical and physical vapor deposition techniques, solid free-form fabrication (SFF) techniques, laser

deposition methods and selective laser sintering [26]. However, it is observed that traditional manufacturing techniques are challenging to adopt for the development of FGM. To solve the limitations associated with traditional production techniques, additive manufacturing (AM) approaches might be used [27].

In recent years, the implementation of AM methods has emerged as a transformative approach to impact the development of FGMs, moving away from the conventional metal production model that relies on sophisticated layer-by-layer machinery to a more streamlined process [28]. The versatility of AM methods has become increasingly prevalent across various applications, including architecture, medical fields, robotics, automotive, space exploration, energy, and sports applications, where the need for graded properties is essential due to the ability to process a diverse range of materials [29]. The different manufacturing methods which are used for manufacturing of FGM as shown in Figure 1.7.

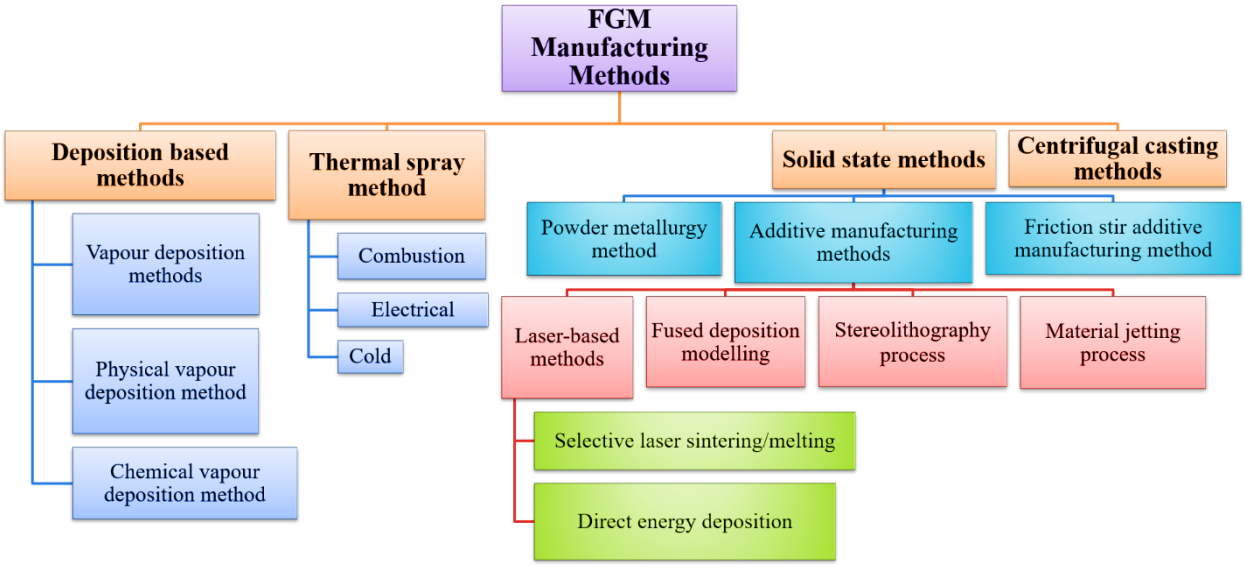

Figure 1.7: Various manufacturing techniques of FGM [28]

1.4.1 Additive Manufacturing

The additive Manufacturing processes construct three-dimensional (3D) parts by incrementally adding layers of materials under the guidance of a digital model. This unique characteristic produces intricate or customized parts directly from the design in a single step, eliminating the necessity for costly tooling such as punches, dies, or casting moulds. Additionally, AM facilitates a notable reduction in the part count by eliminating or minimizing the assembly of

multiple components. The AM eliminates unnecessary welds and joints, resulting in smoother property gradients and greater design flexibility. Moreover, AM offers the advantage of on-demand production, thereby reducing spare inventory and shortening lead times for critical or obsolete replacement components.

Thus, AM has gained widespread acceptance as a new paradigm for designing and producing high-performance components across the aerospace, medical, energy, and automotive industries. In aerospace applications, it includes intricate fuel injector nozzles that previously required the assembly of multiple parts and lightweight engineered structures, leading to significant cost savings [30]. In the medical field, AM-produced implants and dental prosthetics offer notable enhancements in integration, biocompatibility, and the potential for patient-specific devices derived from medical imaging [31]. High-temperature materials are employed in AM to fabricate mixing and swirling burner tips with complex shapes, resulting in energy savings, extended component lifetimes, and reduced system repair and downtime.

1.4.1.1 Advantages of Additive Manufacturing

Additive Manufacturing represents a revolutionary production method enabling the fabrication of near-net shape intricate components without the necessity for dies or extensive machining. This approach significantly reduces lead time, waste generation, and overall costs.

AM has gained increased attention in recent years due to its rapid prototyping capacity and near-net-shape component fabrication. The following vital factors delineate the potential benefits of AM within the aerospace manufacturing domain:

- Additive Manufacturing is a process that creates near-net shape components directly from powder or wire, requiring minimal finishing operations.
- The absence of tooling requirements, such as forging dies, enables the manufacture of complex shapes in shorter timeframes and at lower costs than traditional methods, which often involve lengthy tool design and production periods.
- AM offers unparalleled geometric design flexibility, allowing for the production of intricate shapes that are not feasible with conventional methods. Control over deposition direction, spot size, powder feed rate, and heat source movement enable optimization of component geometry, leading to significant weight reductions.

- In sectors like aviation, characterized by low-volume manufacturing needs, AM is economically advantageous due to reduced costs associated with producing customized components.

- The ratio of mass of raw material to mass of final product (i.e. buy-to-fly ratio) for AM-produced components is typically between 1.5 and 5, significantly lower than the 10 to 20 ratio seen in conventional ingot cast-roll-forging and machining processes [32]. This reduction in material waste, especially with expensive reactive materials like Titanium, Cobalt, Nickel, and Chromium-based alloys, translates to substantial cost savings.

- AM promotes sustainability by allowing excess powder reuse from the printing process. This reduces raw material consumption by up to 90% compared to traditional manufacturing methods.

1.4.1.2 Limitations of AM

The following main factors outline the limitations of AM in different manufacturing industry,

- Powder bed additive manufacturing exhibits a relatively slow deposition rate and limited build volume. In contrast, wire deposition offers faster deposition rates but may not be suitable for producing intricately designed parts [33].

- The Electron Beam Surface Melting (EBSM) process requires substantial initial investment and operates under high vacuum conditions.

- Ensuring control over defects like pores and lack of fusion is crucial in additive manufacturing processes[34].

- Achieving repeatability and reproducibility in part quality ensures consistency and reliability.

- The absence of reliable test standards poses a challenge in assessing the quality and performance of additive manufactured parts.

1.5 METAL ADDITIVE MANUFACTURING

The diversified requirements of the engineering components for various industrial applications are required to serve in harsh working conditions. The metal-based components can be the right choice to satisfied these requirements. Metal-based AM parts are now widely utilized in various sectors, including automotive engineering, aerospace assemblies, power tools, and manufacturing equipment such as jigs, fixtures, and drill guides.

1.5.1 Classification of Metal AM Based on Material Feed System

On the basis of material feed system, AM for metallic materials are divided into three categories, namely [35]:

i. powder bed systems,

ii. powder feed systems, and

iii. wire feed systems

1.5.1.1 Powder Bed AM

A powder bed AM is a process in which part is fabricated by spreading powder evenly across the work area as shown in Figure 1.8 (a). The energy source, whether an electron beam or a laser beam, is precisely controlled to apply energy to the surface of the powder bed, causing it to melt or sinter into the desired shape[36]. The powder is then spreaded across the work area, and the process is repeated to build a solid three-dimensional (3D) component. This system offers several advantages, including creating high-resolution features and internal passages and maintaining precise dimensional control.

1.5.1.2 Powder Feed AM

Powder feed systems are more adaptable to scale up their build volumes than powder bed units. In these systems, powders are conveyed through a nozzle onto the build surface, where a laser is employed to melt one or more layers of the powder into the desired shape as shown in Figure 1.8 (b). This process is repeated to fabricate a solid three-dimensional component. The advantages of this system include its larger build volume and suitability for refurbishing worn or damaged components[37].

1.5.1.3 Wire Feed AM

A schematic representation of a wire feed unit is illustrated in Figure 1.8 (c). This unit utilize wire as the feedstock material, with energy sources including electron beams, laser beams, and welding arcs. Initially, a single bead of material is deposited, and subsequent passes build upon it to form a three-dimensional structure. Generally, wire feed systems are well-suited for high deposition rate processing and offer large build volumes[38]. However, the fabricated product often requires extensive machining than powder bed or powder feed systems.

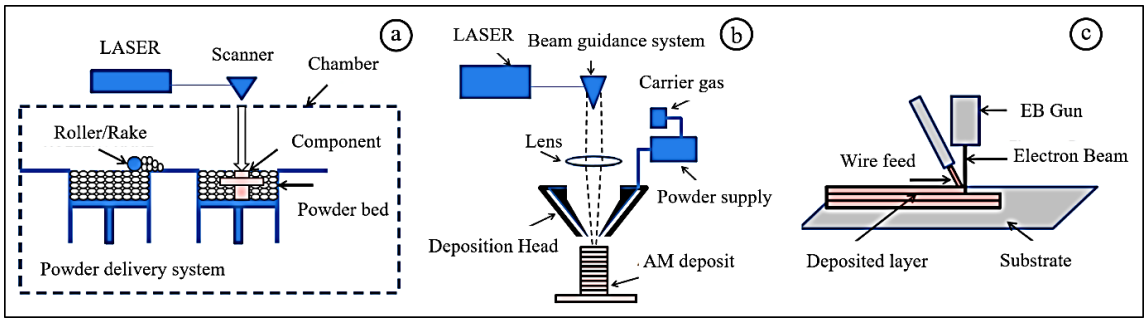

Figure 1.8: Schematic diagrams showing (a) powder bed systems, (b) powder feed systems, and (c) wire feed systems [35]

1.5.2 Classification of Metal AM Based on Energy Source

Metal AM techniques can be classified into laser AM, electron beam AM, or Wire Arc Additive Manufacturing (WAAM) based on the heat source.

1.5.2.1 Laser AM Techniques for Metal FGMs

The Laser based AM (Figure 1.9) employs a high-energy laser as the heat source and utilizes either metal wire or powder as the raw material. This process involves stacking the materials layer by layer until complete parts are formed directly. The laser AM can be categorized into two main methods based on how the raw material is supplied: laser-directed energy deposition (DED) and laser powder bed fusion (LPBF).

In the laser DED technique, a laser is utilized as the heat source to create a molten pool in the deposition area, moving at high speed. The raw materials, whether wire or powder, are fed directly into the high-temperature melt area for rapid melting and solidification, ultimately resulting in the fabrication of complete parts through layer-by-layer deposition. Variations of

the DED technique includes laser metal deposition (LMD), direct laser metal deposition (DLMD), laser-engineered net shaping (LENS), and laser cladding (LC).

By employing the DED technique, it becomes possible to prepare FGMs by controlling parameters such as the feeding rate ratio of different raw materials (powder, wire) or adjusting the laser scanning strategy. Currently, DED stands as the most suitable Additive Manufacturing process for fabricating metal FGMs.

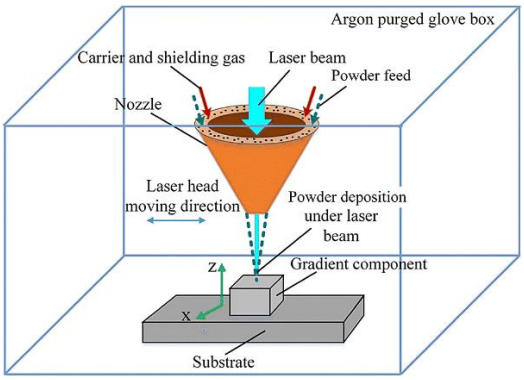

Figure 1.9: Schematic diagram of laser based metal AM process [39]

1.5.2.2 Electron Beam Based Additive Manufacturing for Metal FGMs

The electron beam AM (Figure 1.10) process utilizes a high-energy-density electron beam for heating, accompanied by wire or powder raw materials. These materials are placed within a vacuum environment and deposited along a predetermined path to create finished parts. This technique encompasses variations like electron beam formation (EBF) and electron beam selective melting (EBSM). By adjusting the ratio of different raw materials, the electron beam AM method allows for producing FGMs (Figure 1.10 (b)). This approach offers notable benefits for Additive Manufacturing of refractory metals and active metals under high-temperature conditions.

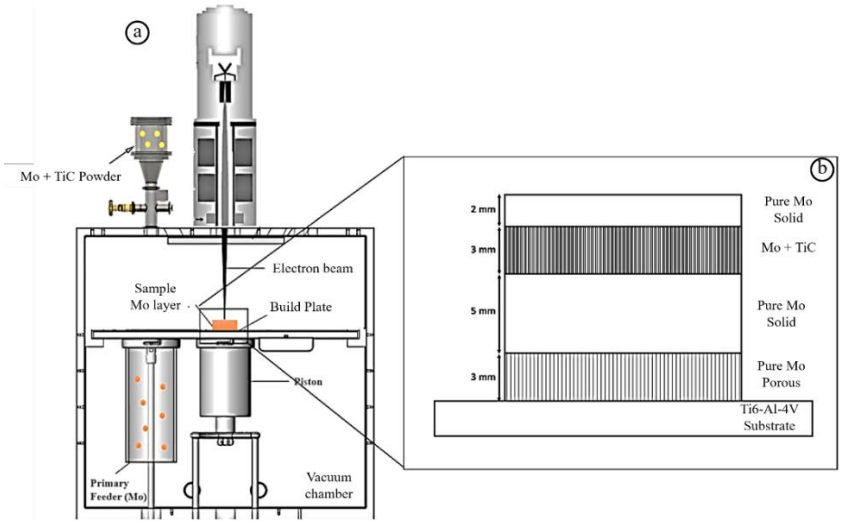

Figure 1.10: (a) Schematic of the of electron beam based metal AM, (b) Schematic diagram of Mo–Mo + TiC–Mo sandwich FGM sample [40]

Metal additive manufacturing falls into three categories based on energy source: laser-based, arc welding-based, and electron beam-based as discussed above. Laser-based systems have been widely adopted for their precision; however, they exhibit poor energy efficiency, typically ranging from 2% to 5% [41]. Electron beam systems offer slightly higher energy efficiency, ranging from 15% to 20%, but require a high vacuum working environment, making them more suitable for aerospace applications [42]. In contrast, arc welding processes such as gas metal arc welding (GMAW) or gas tungsten arc welding (GTAW) processes boast significantly higher energy efficiency, reaching up to 90% in certain circumstances [43]. Additionally, traditional arc welding equipment is relatively cost-effective compared to laser or electron beam equipment [44].

1.5.2.3 Arc Based Additive Manufacturing of Metal FGMs

A process that uses an electric arc as a heat source and wire as a feedstock is commonly known as wire arc additive manufacturing. It has been investigated for AM purposes since 1990s [45], with the first patent filed in 1925 [46]. The WAAM hardware typically utilizes standard welding equipment readily available in the market, including welding power sources, torches, and wire feeding systems. The motion control can be achieved through robotic systems (as shown in Figure 1.11 (a)) or computer numerically controlled gantries. Additionally, Figure 1.11 (b) illustrates a friction stir welding machine retrofitted with a metal inert gas (MIG) power source.

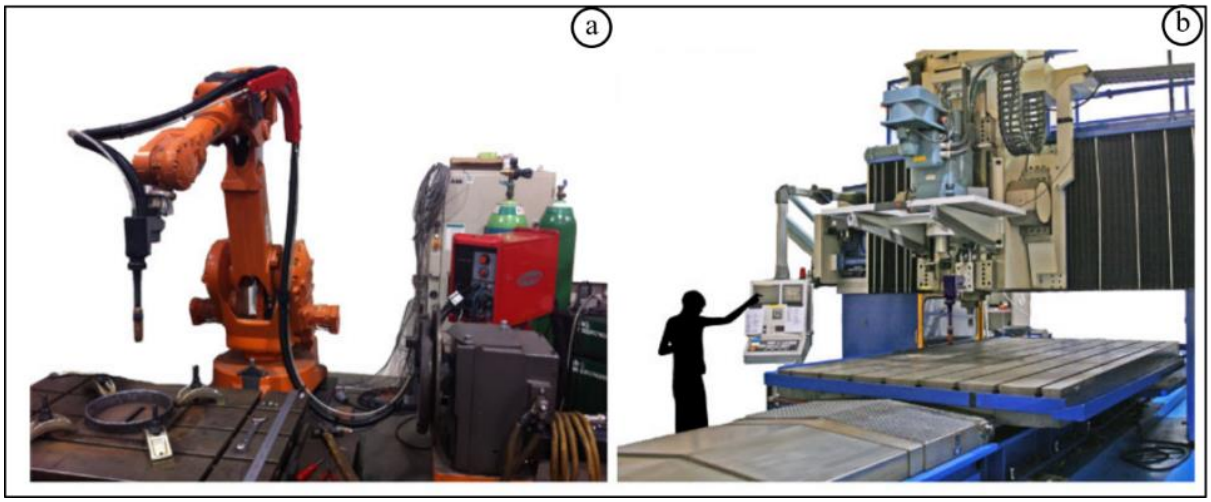

Figure 1.11: (a) six-axis welding robot and (b) deposition system retrofitted onto former friction stir welding machine[45]

1.6 POST PROCESSING TREATMENT

AM of metals frequently displays various defects such as porosity, cracking, delamination, and residual stresses [47]. These defects can evident due to several factors, such as suboptimal process parameters, thermal cycle, quality of selected feedstock materials, contamination of feedstock material, and inadequate working conditions. Most of the issues affecting deposition quality can be addressed effectively through the cautious application of post-processing treatments [48]. Numerous post-processing technologies have been identified to enhance part quality in the AM products, including, interpass cooling [49], machine hammer peening (MHP) [50], heat treatment [51] and interpass cold rolling [52] as shown in Figure 1.12 (a-e).

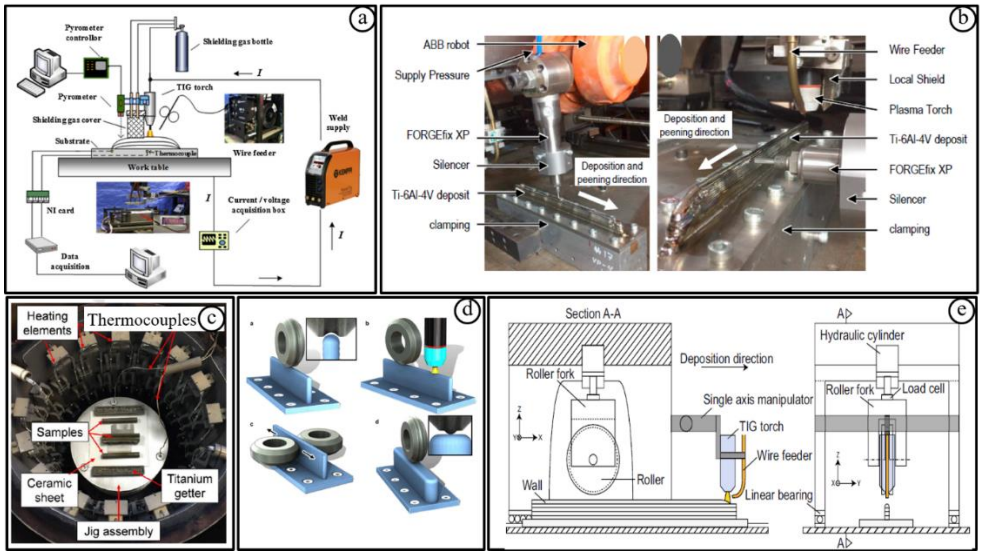

Figure 1.12: Post processing techniques (a) interpass cold rolling, (b) machine hammer peening (MHP), (c) heat treatments (d) different rolling methods, and (e) interpass rolling [49-52]

1.7 THESIS OUTLINE

The current thesis work has been divided into the following chapters:

Chapter 1: This introductory chapter serves as a foundation for understanding FGM and their manufacturing methodologies. The discussion begins by explaining the fundamental concepts of FGM, highlighting the significance of their tailored material properties and applications in engineering.

Chapter 2: This chapter provides a comprehensive summary of recent research findings on FGM developed through various additive manufacturing techniques. A meticulous literature review has been conducted to assess the current state of research in this field, focusing on recent advancements and methodologies employed by researchers. The review critically evaluates and synthesizes existing knowledge, offering a technical perspective on ongoing developments, challenges, and innovations in FGM fabrication using additive manufacturing.

Chapter 3: This chapter outlines the basis for selection of materials along with their various characterization techniques using for materials and developed FGM has been discussed. The detailed design and fabrication processes utilized in the development of Functionally Graded Materials (FGM) are also highlighted and discussed in detail.

Chapter 4: This chapter provides a detailed experimental procedure for the development of FGMs, encompassing the optimization of process parameters for Gas Tungsten Arc Welding (GTAW) and post Friction Stir Processing (FSP) techniques. It also explores into a thorough discussion of the strategic approach to FGMs development, emphasizing material selection and strategic planning for composition variation, aiming to achieve seamless property transitions and optimized material performance for diverse engineering applications.

Chapter 5: This chapter outlines the metallurgical and mechanical characterization of developed Ni-based FGMs. The results obtained by using suitable techniques and standards to analyze the microstructure, distribution of alloying elements, phase formation, microhardness, and tensile strength are presented and discussed in detail.

Chapter 6: This chapter outlines the basis of material selection, the GMAW setup and fabrication strategy for developing ER316L-ER2205-IN718-based trimetallic FGM. The metallurgical and mechanical characterization of developed trimetallic FGM was carried out. The results obtained by using suitable techniques and standards to analyze the microstructure, segregation of intermetallic compounds at interface, phase formation, microhardness, and tensile strength are presented and discussed in detail.

Chapter 7: The conclusions on the findings from the present research work have been discussed. The major outcomes of the present work and future scope have been also highlighted.

Chapter 2

LITERATURE REVIEW AND PROBLEM FORMULATION

This chapter extensively reviews the functionally graded materials establish a dynamic research domain that has gain significant attention within the materials science and engineering community. Recent years have witnessed notable advancements in the manufacturing methods of FGMs, with a spectrum of processing techniques, ranging from conventional to advanced. In this context, the current chapter provide an overview of recent research findings on development of FGMs and their mechanical and metallurgical characteristics.

2.1 FGM DEVELOPMENT

The exploration of gradient materials traces back to 1972 when M.B. Bever initiated deliberate research on graded materials [53]. However, functionally graded materials were first proposed in 1984 by Japanese material scientists M. Ninno and A. Kumakawa primarily to enhance thermal barrier coatings[54]. The necessity for advanced thermal barrier coatings (TBC) emerged in 1987 with the inception of commercial supersonic space shuttle development programs, driving the first comprehensive investigations into gradient materials [55]. The subsequent development of FGM is shown in Figure 2.1.

FGMs have gained importance due to their tailored properties and lack of distinct boundaries or sharp interfaces, which is a major challenge with traditional composite materials. In conventional composites, higher local interlaminar stresses often result in layer separation, disrupting the load transfer mechanism between the matrix and reinforcement. This leads to reduced stiffness and compromised structural integrity, ultimately resulting in functional and structural failure. FGMs offer a promising opportunity to reduce mechanical and thermal stress concentrations in various structural materials designed for specific applications [56].

FGMs offer numerous applications, such as biomaterial implants, thermal barriers, energy conversion materials, metal cutting tools, mechanical components like gears, and optical/optoelectronic devices.

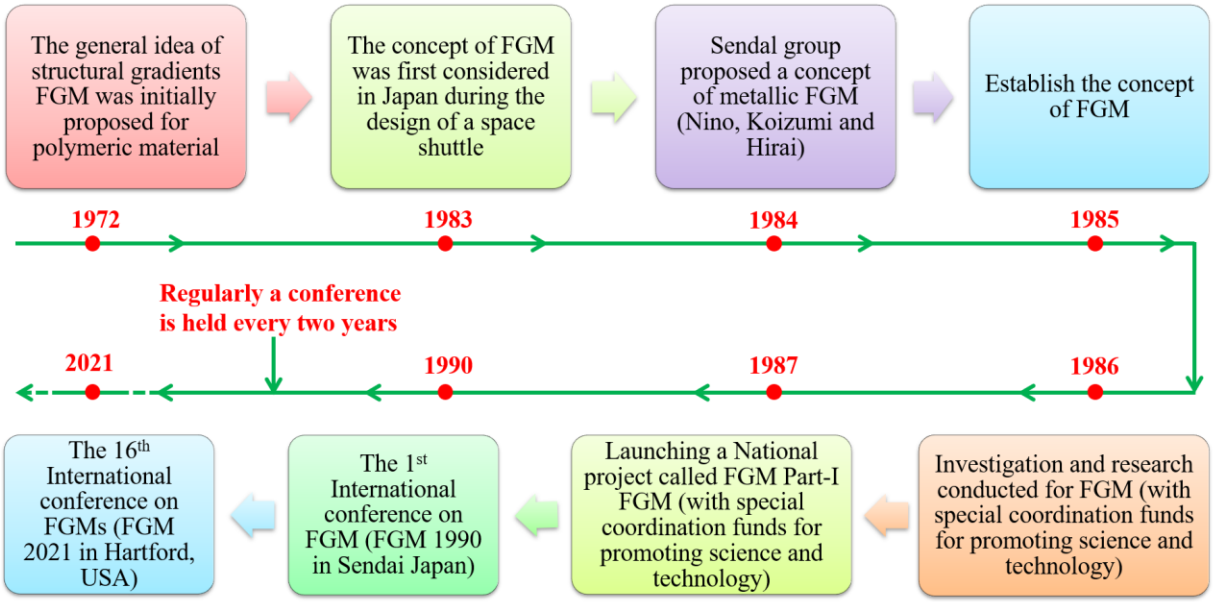

Figure 2.1: Historical overview of relevant milestones in the research and development of FGMs [57]

2.2 TYPES OF FGMs

According to material combination FGM is divided in four broad category such as metal–metal, metal–ceramic, ceramic–ceramic, and ceramic–polymer, as depicted in Figure 2.2. ceramic-ceramic FGMs are effective thermal barrier coatings in high-temperature environments due to their excellent heat insulation properties. Moreover, in biomedical implant applications, polymer-ceramic FGMs are preferred for their combination of biocompatibility from polymers and strength from ceramics.

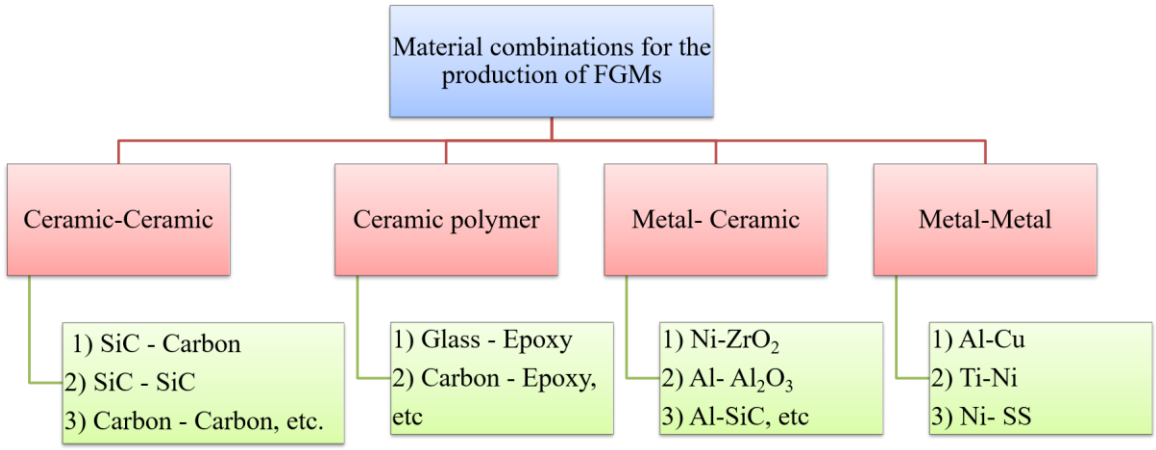

Figure 2.2: Possible material combinations used in FGMs [58]

Metal-ceramic FGMs are found to be extensively used in aerospace applications due to their toughness and high-temperature resistance. For instance, *Ruys et al.* [59] developed a metal-ceramic FGM (Cu-SiC) specifically for thermoelectric converter applications. On the other hand, metal-metal FGMs are widely employed in aviation, nuclear power, and automotive sectors, particularly in scenarios requiring the joining of dissimilar metals. Metal based FGMs are characterized by a gradual distribution of metal compositions, resulting in distinctive mechanical and physical property gradients. FGMs with a gradient interface are preferred over dissimilar joints or conventional composite materials with sharp interfaces. This preference is due to several advantages, including higher toughness and lower residual stress levels resulting from the gradual transition in physical, metallurgical, and mechanical properties between adjacent layers. These characteristics enhance structural performance and prolong component life. Consequently, FGMs find widespread application in industries requiring varied and sometimes conflicting properties within specific components, such as the energy sector, aerospace, automotive, optoelectronics, and medicine. Many metal-based (continuous and discontinuous) FGMs have been developed, and this section presents some of them.

Hofmann et al. [60] studied the performance of a gradient transition joint from 304L stainless steel to Inconel 625, comparing it with a friction-welded joint of the same materials for an automobile valve stem. Their study revealed a significant reduction in stress concentration, nearly tenfold, when using the gradient transition joint compared to the friction-welded joint at an operating temperature of 1000 K (Figure 2.3). *Lu et al*. [27] developed a Ti-Ni based FGM with a continuous variation from TA1 (100%) to Inconel 625 (100%) in the steps of 10%. It has significant potential for use in aerospace and nuclear applications under extreme environmental conditions. *Rodriguez et al*.[61] investigated the development of a FGM based on SS316L and a Ni alloy. Various configurations were analyzed, including a hard transition (discontinuous) and a smooth transition (continuous) with a region comprising 50% SS316L and 50% Ni80-20. The metallographic analysis of both hard and smooth transition SS316L-Ni80:20 FGM, smooth transition FGM exhibited superior performance attributed to its continuous chemical composition change within the structures. *Li et al*.[62] fabricated a metallic FGM composed of SS316L and Inconel718. The FGM exhibited 10 layers with continuous compositional variation, transitioning from 100% SS316L at the bottom layer to 100% Inconel718 at the top layer.

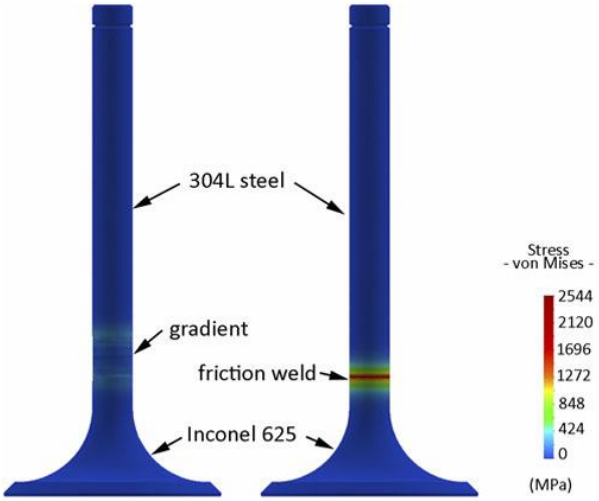

Figure 2.3: Depicts a finite element model of automobile valve made of 304L stainless steel stems connected to an Inconel 625 valve with (a) graded composition and (b) sharp interface joined by friction stir welding (FSW) [60]

2.3 APPLICATIONS OF METAL BASED FGMs

FGMs present an optimal solution to address the rising demand for applications requiring dissimilar properties within single components. In certain scenarios, dissimilar metal welds (DMWs) become necessary, leading to potential high-stress concentrations, particularly in high-temperature environments. Conversely, some components mandate graded mechanical properties, necessitating high hardness on their outer surfaces while retaining high ductility internally. Therefore, FGMs with gradient properties find extensive utilization across diverse industries, spanning aerospace, automotive, coatings, electronics, and cutting tools.

Once, the technological and metallurgical obstacles of functionally graded metals are conquered, their potential applications become limitless. A particularly promising short-term use is substituting problematic DMWs with additively manufactured graded transition joints. In industries such as nuclear and aerospace, issues restricting from failures at joints and interfaces between dissimilar metals are dominant [63]. Traditional joining methods often result in abrupt gradients in composition and properties, exacerbating failure mechanisms during service. The assembling of numerous parts of varying materials to meet spatially diverse service and cost requirements further limits design flexibility, especially for low-volume, high-complexity components. Incorporating functional grading with additive manufacturing emerges as an attractive solution.

The most common challenges in the nuclear energy sector are ferritic-austenitic joints, which have been a persistent materials concern for years. Present-day coolant systems in light water reactors (LWRs) necessitate joining ferritic steel nozzles on the reactor pressure vessel (RPV) to austenitic stainless-steel piping [64]. However, the thermal expansion mismatch and compositional disparities between these steel types pose difficulties for existing welding methods. A conventional DMW design for this application involves an A508 carbon steel RPV pipe nozzle connected to a 316L SS pipe using a nickel-based filler metal, such as Alloy 52M [65]. Despite employing strategies like buttering layers, nickel-based weld metal, and post-weld heat treatments to mitigate residual and thermal stresses, these joints remain prone to thermal sensitization and stress corrosion cracking in the reactor environment, often leading to coolant leaks. The gradual change in composition along the part's length would eliminate the sharp interfaces as illustrated in the schematic in Figure 2.4 (a and b).

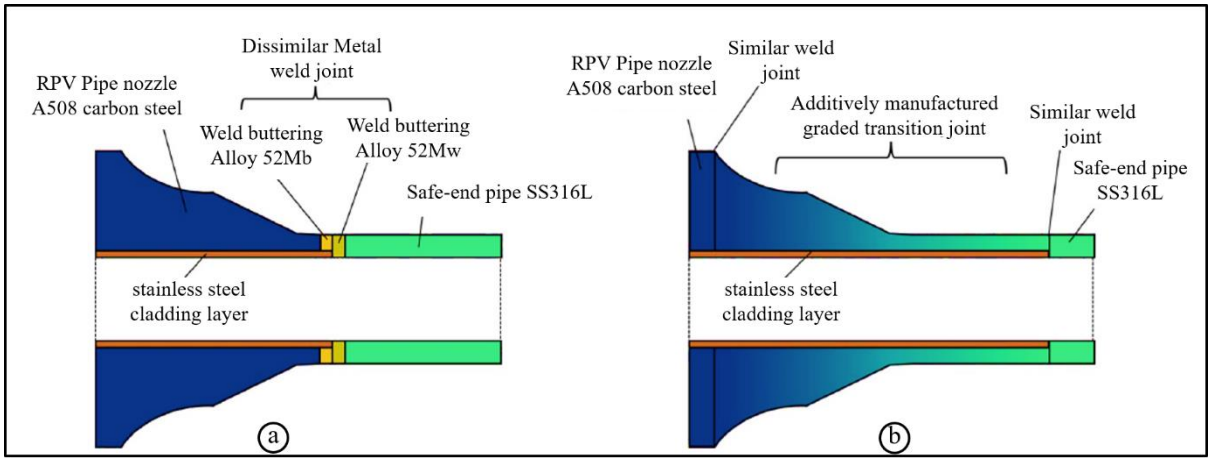

Figure 2.4: Schematic cross sectional view showing (a) conventionally designed dissimilar metal welded joining, and (b) functionally graded additively manufactured joint [66]

In aerospace applications, dissimilar joints are critical in optimizing strength, high-temperature resistance, and weight reduction, particularly in aircraft jet engines. To address these challenges, FGMs give a better alternative approach. Therefore, most spacecraft and aircraft components currently employ FGMs with gradient properties. These include critical elements such as rocket engines, spacecraft gear structures, and heat exchange plates, as well as various structural components like reflectors, solar panels, camera mounts, turbine wheels, turbine blade coatings, nose covers, and the leading edges of missiles and space shuttles, as illustrated in Figure 2.5.

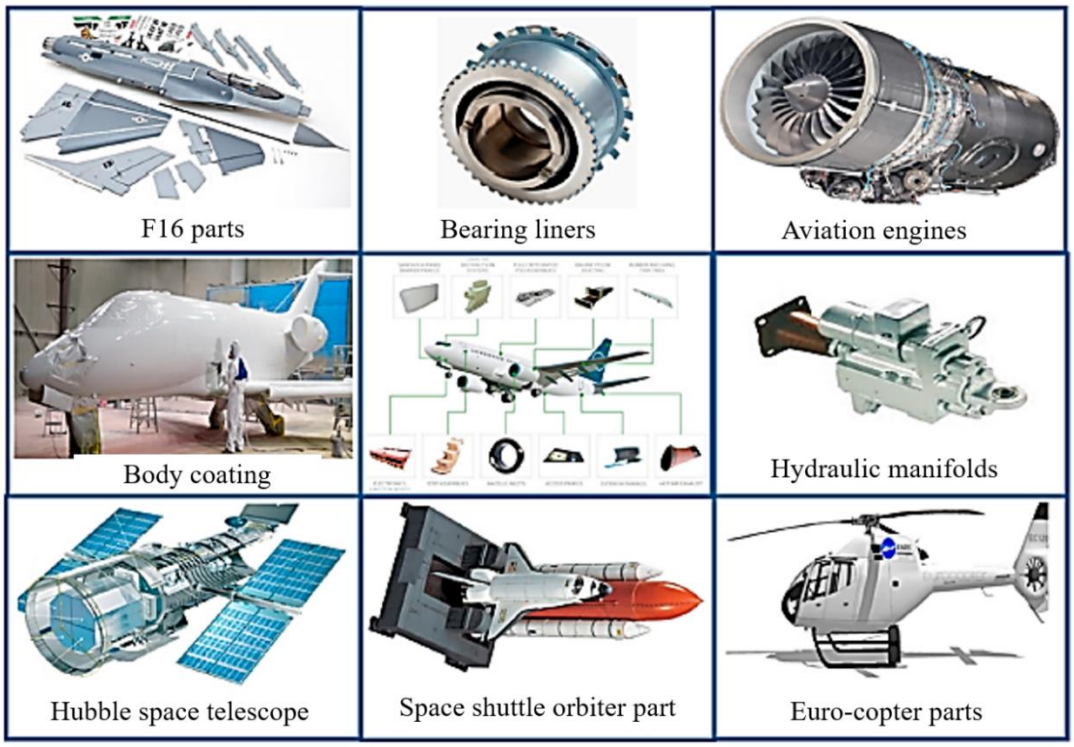

Figure 2.5: Applications of functionally graded materials in aerospace sector [67]

Various automotive components, including diesel engine pistons, cylinder liners, combustion chambers, racing car brakes, driveshafts, and flywheels, often require graded thermal, pressure, or stress resistance properties. FGMs are well-suited for these applications, as depicted in Figure 2.6. FGMs with graded properties also hold potential for automotive body coatings. However, due to high costs, the utilization of FGMs in automotive contexts is limited and generally restricted to critical parts.

In recent years, FGM compositions such as FG WC/Co and TiCN WC/Co have gained prominence in producing cutting tools like turning tools, grinding and milling cutters, and twist drills. These materials improve surface wear resistance and hardness, increasing tool lifespan and feed rate during machining operations and reducing machining time [68]. Heavy machinery and tooling sector also hold significant potential to use FGMs with a graded structure. FGMs are extensively utilized in manufacturing various engineering components, including cutting tools, metal forming moulds, and machine engine blocks. They offer significant enhancements in strength, thermal, wear, and corrosion resistance for these components [69].

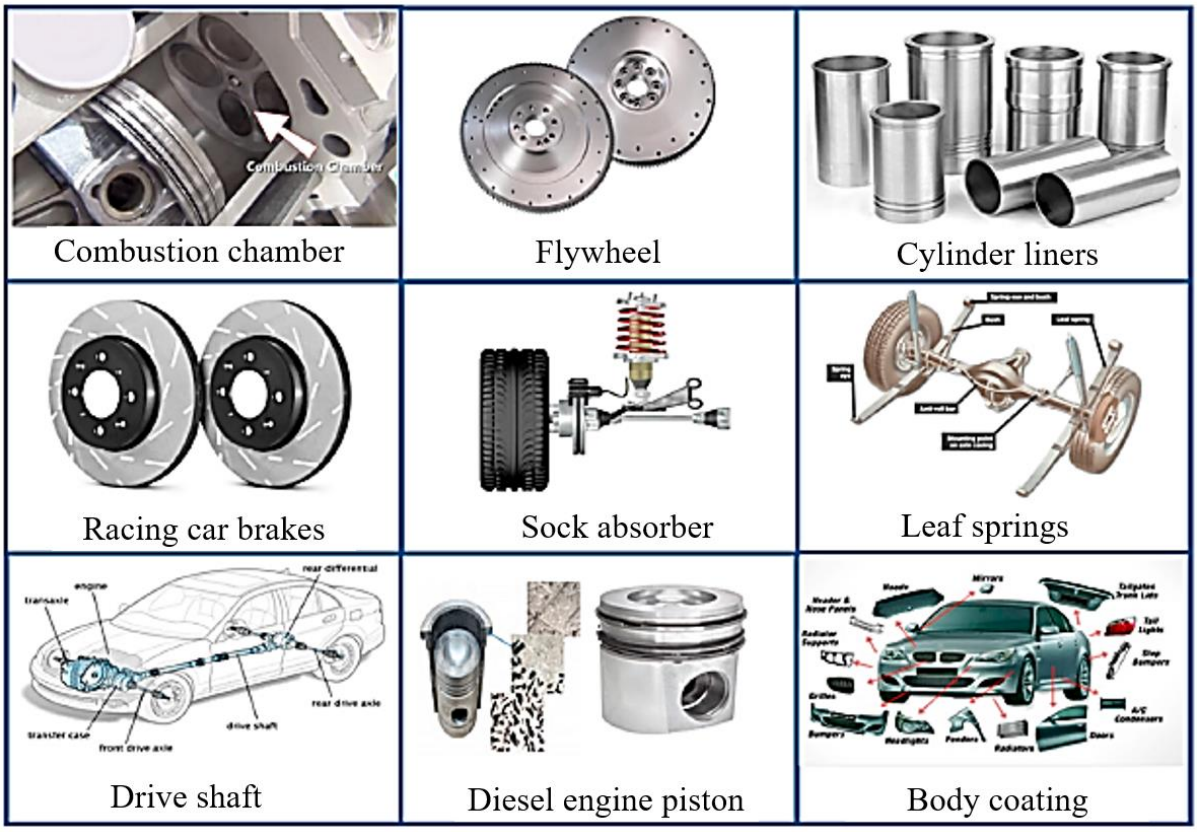

Figure 2.6: Applications of functionally graded materials in automotive sector [70]

2.4 FABRICATION OF METAL BASED FGMs

The abrupt transition in microstructure and properties of dissimilar metals poses challenges such as lack of fusion, compromised mechanical properties due to non-uniform melting and rapid solidification, and micro-segregation of alloy elements [12]. To address these issues, various studies have proposed AM techniques for the fabrication of FGMs [66, 71-73]. *Cesar et al.*[74] explored the fabrication of multi-material structures using Ti-6Al-4V and copper through the electron beam melting (EBM) based AM. They developed a novel method involving multiple build sequences to accommodate both materials.

The co-axial deposition capability of laser engineered net shaping (LENS) facilitates the fabrication of smart and functional components, providing enhanced compositional precision and improved properties [75]. It is uses a focused laser beam as heat source and it create a liquid metal pool on a substrate in which the metal feedstock (powder/wire) is supplied [76]. *Meng et al.* [39] investigated the gradation strategy during the fabrication of a FGM from Inconel 625 to Ti6Al4V using LMD. *Bayode et al.* [77] investigated the application of LMD

for the development of a FGM based on stainless steel. This study employed two grades of stainless-steel powder: AISI 316L and 17-4 PH. Both metal powders were fed together through a coaxial delivery nozzle, converging at a single liquid metal pool. Varying flow rates were employed to achieve the intended gradient of alloys. Rapid melting and solidification occur during the LMD process, increasing the possibility of intermetallic compound formation while fabrication of FGM. This issue requires attention and mitigation strategies. It was observed that cracks occurred in the transition zone between 80% Inconel 625 and 20% Ti6Al4V, as well as between 70% Inconel 625 and 30% Ti6Al4V for non-preheated samples due to the formation of massive Cr- and Mo-enriched phases. In contrast, no cracks were detected in preheated gradient samples.

Gunasekaran et al.[78] reviewed the application of selective laser melting techniques to fabricate various metal based FGM such as aluminium alloys, magnesium alloys, titanium alloys and various grades of steel. *Bobbio et al.* [79] developed FGM composed of Ti6Al4V, and Invar using direct energy deposition (DED). *Yoo et al.*[80] observed that the fabrication of bimetallic structures using LMD alone is slower and time taking. Consequently, many researchers have turned to WAAM as an alternative method which has several advantages, including its relatively low cost, elimination of the need for a vacuum chamber (unlike electron beam methods), economical applicability to large operating volumes, and higher deposition rates [81].

2.5 WIRE ARC ADDITIVE MANUFACTURING

The concept of wire arc additive manufacturing originates from additive layer manufacturing (ALM), wherein the part is built up through the deposition of material layer by layer [82]. The roots of the WAAM process can be traced back to the 1920s when Baker [46] proposed using an electric arc as the heat source and filler wires as feedstock materials to deposit metal ornaments. WAAM offers several advantages over other additive manufacturing processes, such as the ability to work with materials or produce parts with metals that are challenging to machine, faster production speeds compared to other metal additive manufacturing methods, direct production of metallic parts from CAD models, and high productivity.

2.5.1 Classification of Wire Arc Additive Manufacturing

The WAAM process is classified on the basis of the heat source, which are commonly three types [83] : gas metal arc welding (GMAW), gas tungsten arc welding (GTAW) and plasma arc welding (PAW). These power sources have specific features as listed in Table 2.1. The deposition rate of GMAW- based WAAM is 2 to 3 times higher than that of GTAW-based or PAW- based methods. However, the GMAW-based WAAM is less stable and generates more weld fume and spatter due to the electric current acting directly on the feedstock. The choice of WAAM technique directly influences the processing conditions and production rate for a target component.

Table 2.1: Comparison of various WAAM techniques [47]

WAAM Method	Energy source	Features	References
GTAW Based	Arc	Non-consumable electrode; Separate wire feeder required; Typical deposition rate: 1-2 kg/hour; Simultaneous control of Wire feeder and welding torch needed;	
GMAW Based	Arc	Consumable wire spool electrode; Typical deposition rate 3-4 kg/hour; Poor arc stability, higher weld spatter;	
Cold metal transfer (CMT)	Arc	Reciprocating consumable wire electrode; Typical deposition rate: 2-3 kg/hour; Low heat with zero spatter, High process tolerance;	
Twin wire GMAW	Arc	Two consumable wires electrodes; Typical deposition: 6-8 kg/hour; Easy mixing to control composition for intermetallic materials manufacturing;	
PAW based	Plasma	Non-consumable electrode; Separate wire feed process; Typical deposition rate 2-4 kg/hour;	

Wire and torch rotation are needed;

A schematic diagram illustrating the GMAW, GTAW, and PAW processes is depicted in Figure 2.7. GMAW involves an electric arc formation between a consumable wire electrode and the workpiece metal, with the wire typically positioned perpendicular to the substrate as shown in Figure 2.7 (a). Metal transfer in GMAW occurs through various methods such as globular, short-circuiting, spray, and pulsed spray, each with distinct characteristics. Additionally, the cold metal transfer (CMT) technique, a modified GMAW variant utilizing a controlled dip transfer mode, has been widely adopted in additive manufacturing because of its high deposition rate and low heat input [84].

In contrast, GTAW and PAW employ a non-consumable tungsten electrode for welding. Unlike GMAW, the orientation of wire feed in GTAW and PAW is variable, influencing deposit quality and complicating process planning. The disparities between the plasma arc and GTAW arc are illustrated in Figure 2.7 (b and c), with the plasma arc exhibiting a narrower high-temperature zone, resulting in relatively narrower weld beads. Plasma welding also offers higher arc energy than GTAW welding, resulting in less weld distortion and smaller, faster welds [85].

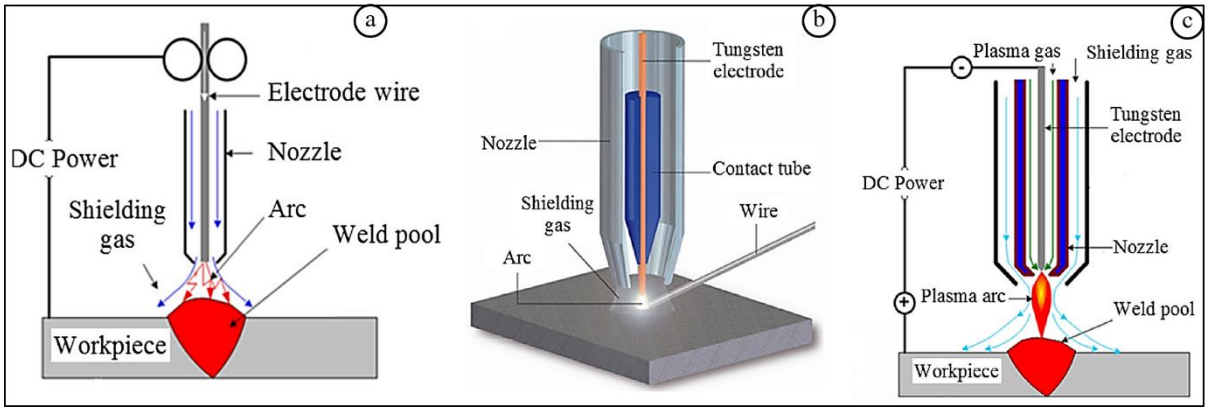

Figure 2.7: Schematic diagram of the (a) GMAW, (b) GTAW, and (c) PAW process [83-85]

2.6 GTAW BASED WAAM

The GTAW utilizes a non-consumable tungsten electrode to generate the welding arc (Figure 2.8). A weld made with this process is stronger, and more reliable than one made with shielded metal arc welding (SMAW) or GMAW [86]. Despite being more challenging and notably

slower than other welding techniques, the need for multi-wire feeding in a single arc mandated GTAW to develop Ni-Cr-Mo-based FGM. In recent years, the GTAW process has been successfully implemented in AM processes for manufacturing various alloy parts, with various control methods developed to optimize its application.

In general, the quality of a weld is assessed based on its microstructure and various factors, including the presence of spatter, overfill, or underfill [87]. Although these characteristics are not easily quantifiable, they are often linked to factors such as the cooling rate of the molten pool, metal transfer mode, bead geometry, and surface quality of substrate. Moreover, many of these attributes are influenced by the mass and heat transfer during the welding process to the weld pool, and the thermal cycling processes during deposition play a significant role in determining the chemical composition, microstructure, and mechanical properties of the fabricated materials [88]. As a result, the integrated control of GTAW for wire-based metal additive manufacturing can be categorized into three main sections: control of welding parameters, control of the welding pool, and control of filler material. It has been demonstrated that different combinations of these processing parameters can achieve a deposited layer with similar geometry [89].

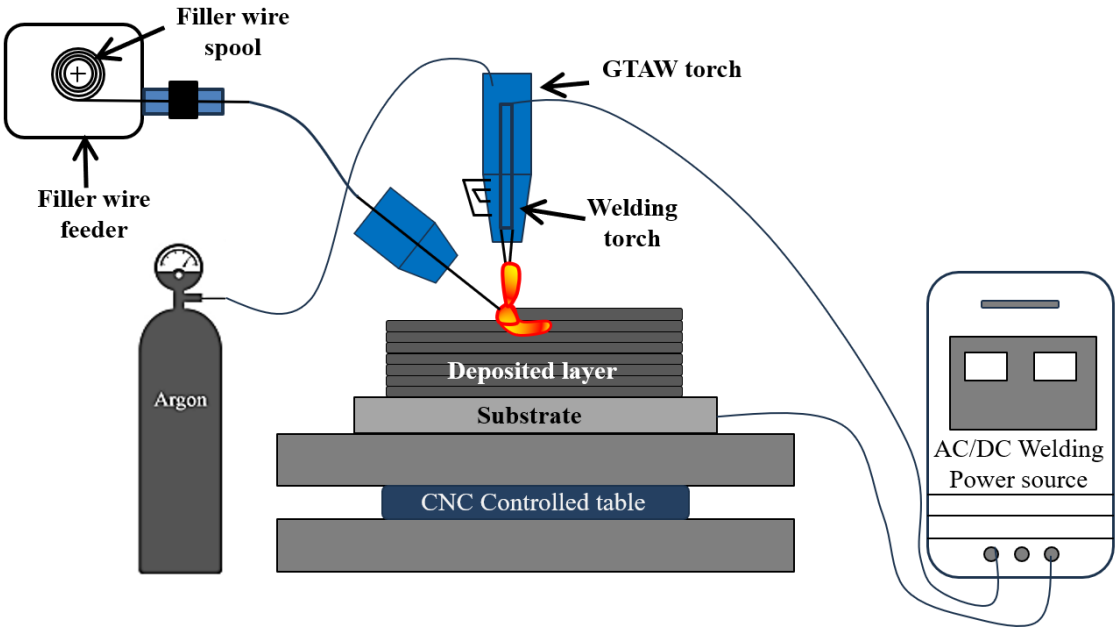

Figure 2.8: Integrated GTAW-AM process

2.6.1 GTAW Process Parameters and Their Effects

In the GTAW process, welding parameters typically include welding current, voltage, travel speed, and shielding gas flow rate. However, for GTAW-powered additive manufacturing processes, additional parameters such as preheating temperature and interpass temperature control become necessary. These parameters directly influence the molten pool's dimensions (depth and width) and the deposited material's quality during the deposition process [90]. Controlling these parameters ensures an appropriate thermal cycling field throughout the multi-pass fabrication process. Welding current primarily impacts the penetration depth rather than the width of the welds [91]. Selecting the appropriate welding current depends on substrate thickness, material type, travel speed, and joint configuration, aiming to deliver the proper energy input into the weld pool. The resistance heat generated during deposition can be calculated using the equation below [92], where Q_r represents resistance heat, 'I' denote welding current, 'R' signifies the equivalent resistance of the welding arc, and 'T' denotes the welding time at the welding position.

$$Q_r = I^2 R T \text{ -------- } Eq\text{-}i$$

In practical AM operations, linear heat input is a more applicable parameter compared to resistance heat.

$$Q = \eta \frac{VI}{v} \text{ -------- } Eq\text{-}ii$$

In this equation, Q represents welding heat, V denotes welding voltage, I stands for welding current, v represents specific welding speed, and η signifies the heat transfer efficiency of the welding arc to the molten pool. For direct current (DC) GTAW processes, the heat input efficiency typically ranges between 78% and 85%, while for alternating current (AC) processes, it ranges between 68% and 85% [93].

In conjunction with the welding current, a higher welding voltage can lead to an increased width of welds due to the larger cross-section of the torch. In certain operations, welding voltage is primarily influenced by the arc length between the tungsten electrode and the workpiece. A longer arc length can result in wider welds while slightly reducing welding penetration. Maintaining an appropriate arc length is crucial for GTAW processes; excessively long arc lengths can lead to weld porosity and inadequate gas protection for the workpiece,

whereas too short arc lengths can make it challenging for welders to observe the molten pool during deposition. They may cause issues such as short circuits, contamination of the tungsten electrode by the filler material, and excessive burning loss of the tungsten electrode. By controlling the arc length, the shape of the welding pool can be managed, leading to improved welding performance [35]. In butt welding, the optimal arc length is typically approximately equal to the diameter of the tungsten electrode [27]. In specific GTAW operations, the relationship between the appropriate welding voltage and welding current can be described by the empirical formula as given in Eq.3 [94]. Where, V is a voltage across the welding arc and l is an arc length.

$$V = 10 + 0.04\, l \text{ -------- } Eq\text{-}iii$$

Kumar et al. demonstrated the influence of GTAW process parameters on bead geometry, revealing that the bead width increased almost linearly with welding current while other parameters remained constant. Figure 2.9(a) depicts the variations in weld-bead size corresponding to changes in welding current. Moreover, an increase in penetration depth was observed alongside a slight decrease in weld height as the welding current increased. Notably, the rate of increase in bead width surpassed the rate of change in penetration depth or weld height. It was noted that weld width decreased with increasing welding speed, while penetration depth exhibited minimal variation (Figure 2.9(b)). Conversely, weld height decreased as welding speed increased, providing insights into the complex interplay of process parameters on weld characteristics.

Dilution increased with rising heat input when achieved through increased welding current at a constant speed. Conversely, reducing welding speed at a constant current led to a decrease in dilution with increasing heat input. At lower currents (<150A), dilution remained below 15%, whereas it exceeded 50% at higher currents (>230A), underscoring uncertainties associated with TIG welding's dilution behaviour. Remarkably, controlling welding parameters yielded significant differences in dilution levels for the same heat input, emphasizing the nuanced effects of welding current versus welding speed adjustments.

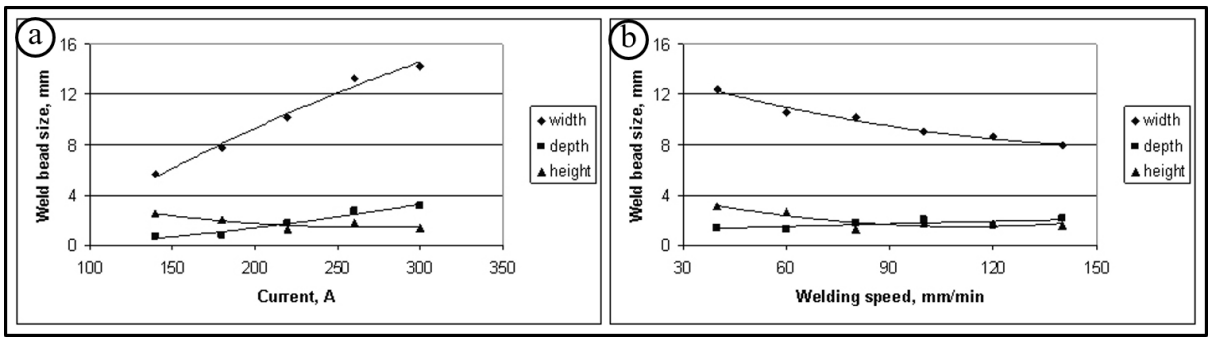

Figure 2.9: (a) depicts the variations in weld-bead size corresponding to changes in welding current (b)) illustrates the relationship between weld size and welding speed [95]

2.6.1.1 Shielding Gas Flow Rate Control

The flow rate of the shielding gas is a critical factor in achieving optimal GTAW bead quality [88]. Maintaining a suitable flow rate is essential to ensure the protection gas forms a laminar flow characterized by good rigidity and a wide coverage area. Insufficient flow rates can lead to low wind resistance during outdoor welding, while excessively high flow rates can cause turbulence in the welding torch, potentially resulting in weld porosity. In certain scenarios, trailing shielding gas may be required to ensure complete protection of the welding bead after solidification.

2.6.1.2 Weld Pool Control

The shape of the welding pool plays a significant role in influencing the welding temperature field, the quality of the weld bead, and sometimes even the phase composition of the fabricated material [96]. In GTAW processes, the molten droplet transfer typically occurs in either globular transfer mode or bridging without interrupting transfer mode. In the globular transfer mode, molten droplets are bigger than the diameter of the filler wire and drop away from the welding wire due to gravity when sufficiently large. This mode yields comparatively uniform weld penetration and helps avoid finger-shaped penetration. However, it can compromise welding arc stability and result in an unsatisfactory bead shape, making it less suitable for materials with low weldability. In bridging without interrupting transfer mode, the filler wire first contacts the molten pool, then rapidly detaches due to overheating before directly transferring into the molten pool. This mode offers steady and precise control over weld shape, making it suitable for GTAW-powered wire-feed metal AM processes [97]. However, the

globular transfer mode may be necessary under certain welding conditions. Achieving the desired transfer mode requires a surveillance and tracking controller system. Research has shown that in-situ, digital, and tracking-type controllers are well-suited for welding pool control systems[98]. Unlike laser or electron beam welding, GTAW processes heavily rely on manual operation. However, efforts are underway to automate or remotely control the process due to its complexity and many uncertainties. In the context of AM processes, changes in the position and size of the weld bead and welding penetration instability can significantly impact welding quality, further complicating the process. Various sensing methods for GTAW have been explored to control the welding process automatically, with practical processing algorithms crucial for desirable sensing results[99]. Vision-based and auditory-based sensing methods are the two main categories, with high-speed, accurate image processing and weld pool reconstruction algorithms required for real-time control [100]. Technological advancements, photoelectronic, image processing, and computer technology have revolutionized visual inspection techniques [101].

2.7 METAL USED IN WAAM

Today, WAAM has become a promising manufacturing process for various engineering materials such as titanium-based alloy, aluminium-based alloy, nickel-based alloy and steel. The WAAM process uses commercially available wires which are produced for the welding industry and available in spooled form and in a wide range of alloys as feedstock materials. The Table 2.2 indicates the commonly used alloys and their various applications in WAAM.

Table 2.2: Metals used with WAAM process under different industrial applications [102, 103]

Applications	Metals/ alloys used
Aerospace	Al alloys, Ti alloys, Ni based super alloys and bimetals of Inconel and stainless steel
Marine	Ti alloy, stainless steel, steel alloys
Automotive	Al alloy, steel alloy and bimetals
Food industries	Stainless steel
Corrosion resistance	Ti alloy, stainless steel, Ni alloy and bimetal
High temperature application	Ni based super alloy, Ti alloy, bimetals

Tools and molds	Tool steel, die steel

2.8 TYPES OF SUPER ALLOYS USED FOR DEVELOPMENT OF FGM

Superalloys are a class of high-performance materials known for their exceptional strength, creep resistance, and corrosion resistance at elevated temperatures. These alloys are typically used in extreme environments, such as aerospace turbine engines, gas turbines, nuclear reactors, and chemical processing plants, where conventional materials would fail. Superalloys traditionally fall into three main classes: Ni-Fe based, Cobalt (Co) based and nickel (Ni) based super alloys.

2.8.1 Ni-Fe-based Superalloys

Superalloys traditionally fall into three main classes. The first class, Ni-Fe-based superalloys, was among the earliest developed. These alloys feature high percentages of iron, which serves as a base material alongside nickel [104]. While sharing similarities with Ni-based superalloys regarding solid-solution strengthening mechanisms, Ni-Fe-based superalloys exhibit a different precipitation morphology, forming spherical rather than cuboidal γ' phase strengthening precipitates [105]. They are predominantly used as wrought rather than cast materials [104].

2.8.2 Co-based Superalloys

The second category is Co-based superalloys, these alloys primarily consist of cobalt as the base metal, with additions of other elements such as chromium, tungsten, and nickel to enhance their properties. Cobalt-based superalloys are widely utilized in aerospace, gas turbine engines, and industrial gas turbines, where they endure extreme temperatures and mechanical stresses.

2.8.3 Ni-based Superalloys

The third category comprises Ni-base superalloys, the most currently utilized blade alloys. These alloys can be subdivided based on microstructure and composition, influencing their strengthening mechanisms. Among all these super alloys, Ni-based superalloys are favored for high-temperature applications, reaching up to approximately 1370°C. Ni-Fe-based superalloys, such as the widely used IN718 alloy, are suitable for lower temperatures, up to around 650°C [106]. Due to their lower cost in alloy additions than Ni-based superalloys, Ni-Fe-based

superalloys are more economically viable at lower temperatures. They are preferred for certain applications based on specific strength requirements [107]. The austenitic face-centered cubic (FCC) matrices characteristic nickel demonstrates exceptional capability for dissolving high concentrations of alloying elements compared to other metals [104].

2.9 TYPES OF Ni BASED SUPERALLOYS

Nickel-based superalloys are categorized into several types based on their composition, microstructure, and intended application. Some common types of nickel-based superalloys are Inconel 625, Inconel718 and Ni-Cr-Mo based alloys.

2.9.1 Inconel 625

Inconel 625 is a nickel-based superalloy renowned for its remarkable strength, primarily attributed to the solid-solution hardening effect generated by refractory metals, such as niobium and molybdenum, embedded within a 'nickel–chromium' matrix [108]. This alloy boasts exceptional resistance to hot corrosion, fatigue, and wear, excellent weldability and impressive strength retention at elevated temperatures [109]. Consequently, it finds widespread application in aerospace, chemical, petrochemical, marine, and other industries requiring materials resistant to high temperatures and corrosion [110]. Despite its utility, the intricate shapes of many Inconel 625 components render them costly to produce using conventional methods, primarily due to extensive machining requirements [111]. Inconel 625 displays precipitation hardening on account of the appearance of the metastable phase γ" [Ni_3Nb] that occurs when annealed over an extended period of time between the temperatures of 550– 850 ℃ [15]. Various forms of carbides like MC, M_6C and $M_{23}C_6$, may also precipitate depending upon the temperature and time of aging. The microstructure of Inconel 625 fabricated by conventional manufacturing process and DED is shown in Figure 2.10 (a) and (b) respectively.

Kumar et.al. observed that in Inconel 625, precipitates formation takes place at a temperature between 650°C and 875°C, which significantly impacting the alloy's strength. When stress is applied at elevated temperatures, $M_{23}C_6$-type carbides grow at grain boundaries. At 700°C, c" precipitates emerge, comprising Ni_3(Nb, Ti, Al) with a tetragonal crystal lattice structure, adopting a disk-shaped morphology coherent with the matrix. At 725°C, d-phase precipitates form, consisting of Ni_3(Nb, Mo) within an orthorhombic lattice structure. Both c" and d-phase

precipitates dissolve into the matrix completely at 875°C, enhancing the alloy's creep properties and extending its lifetime.

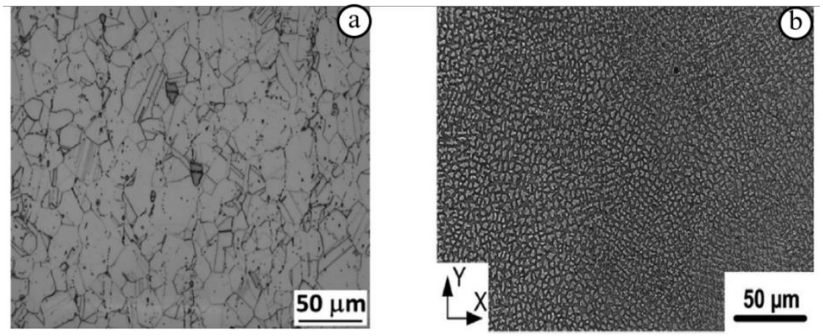

Figure 2.10: Microstructure of Inconel 625 (a) conventional manufacturing process and (b) DED process[112]

2.9.2 Inconel 718

Inconel 718 is a precipitation-hardened nickel–iron alloy with a face-centered cubic structure, modified by the addition of niobium [113]. This alloy is known for its high strength, enhanced creep resistance, and superior fatigue life, particularly at temperatures up to 973 K, along with favorable weldability characteristics [114]. Many of the exceptional properties exhibited by conventional Inconel 718 can be attributed to the precipitation kinetics of the alloy, which are inherently sluggish in nature [115].

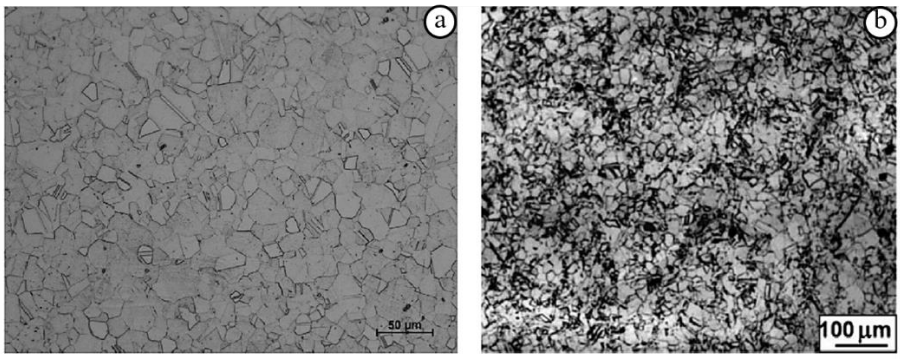

Figure 2.11: Inconel 718 microstructure (a) conventional and (b) DED manufacturing process[116]

The microstructure of Inconel 718 fabricated by conventional manufacturing process and DED is shown in Figure 2.11(a) and (b) respectively. The microstructure of Inconel 718 consists of a face-centered cubic matrix of γ with a significant presence of strengthening carbides and

intermetallic phases, including face centered cubic γ' Ni_3(Al, Ti and Nb), ordered tetragonal γ'' Ni_3Nb, and face centered cubic MX (Nb, Ti) (C, N). Undesirable phases such as hexagonal laves phase A_2: B form (A = Ni, Fe, Cr) and (B = Nb, Mo, Ti) and orthorhombic δ phases Ni_3(Nb, Ti) may also be present. The main strengthening mechanism for Inconel 718 involves coherent metastable phases, γ; and γ'', with specific heat treatment techniques utilized to maximize their precipitation in the nanoscale [117].

2.9.3 ERNiCr-Mo-10

Due to its unique properties, the ERNiCr-Mo-10 material exhibits promising potential for developing Ni-based FGMs. This alloy, composed of Nb-free Ni, Cr and Mo, offers excellent corrosion resistance, high-temperature strength, and good weldability [118]. These attributes make it suitable for applications with a desired gradient of properties, such as in thermal barrier coatings, aerospace components, and chemical processing equipment. By leveraging the compositional versatility of ERNiCr-Mo-10 and controlling processing parameters, engineers can tailor the microstructure and properties along a gradient to meet specific performance requirements, enhancing the functionality and performance of advanced engineering systems.

2.10 DEVELOPMENT OF METAL BASED FGMs USING WAAM

Iron, chromium, and nickel exhibit favorable solubility characteristics, making them suitable alloying element for designing metallic FGMs. A significant interest is being shown in joining stainless steels with nickel-based superalloys to achieve both the elevated temperature strength and cost-effectiveness of the latter. In 1997 *Griffith et al.* [119] prepared precise multi-material processing techniques for depositing FGM structures ranging from SS316 to Inconel 690. This marked one of the earliest instances of laser-deposited metallic FGMs featuring a compositional gradient path transitioning from 100% metal A to 100% metal B. Building on this foundation, *Lin et al.* [120] in 2004 successfully fabricated SS316L/Rene88DT FGMs, varying from 100% SS316L to 100% Rene88DT nickel superalloy. The deposition process involved epitaxial growth of columnar dendrites, a phenomenon which was further investigated.

In the past decade, several studies have focused on steel/Inconel FGMs, exploring various fabrication methods and their effects on material properties. *Carroll et al.* [121] conducted research on SS304L/Inconel 625 FGMs fabricated using LMD without predefined

compositional boundaries. Microstructural analysis revealed a diffused gradient zone without distinct boundaries, and no significant compositional deviations were observed. However, cracks were detected in a region containing approximately 79 wt.% SS304L and 21 wt.% Inconel 625, attributed to the presence of secondary phases.

Shah et al. [72] investigated the manufacturability of SS316L/Inconel 718 FGMs and studied the influence of powder flow rate and laser power on material properties. Various laser power levels ranging from 450W to 750W and powder flow rates of 0.632g/s and 0.834g/s were employed during FGM fabrication. The microstructures of all FGMs exhibited columnar dendritic growth, with the secondary dendrite arm spacing (SDAS) increasing with power and decreasing with powder flow rate. The formation of NbC in regions with higher Inconel content contributed to increased hardness.

Sasikumar et al. [122] conducted a study to manufacture a bimetallic FGM based on SS316L and Inconel625 using GMAW-WAAM. The WAAM process successfully fabricated the FGM without any defects, and no solidification cracking was observed at the bi-metallic interface (IF) region. Microstructural analysis revealed a distinctive transition at the IF, characterized by a discontinuous dendritic structure. This study highlights the potential of WAAM in fabricating FGMs with the desired properties, positioning it as a viable alternative to traditional manufacturing techniques for producing such materials.

In contrast, Zhang et al.[123] explored FGM fabrication method using twin wire GTAW-WAAM. They employed two deposition strategies: iso-variable transition strategy (ITS) and optimized transition strategy (OTS) to produce Inconel625-high strength low alloy (HSLA) steel FGMs. The aim was to utilize FGMs to replace dissimilar joints, reducing challenges with multi-material interfaces. However, FGMs fabricated via ITS using WAAM often suffer from weakened performance or detrimental precipitates due to continuous compositional changes. To overcome this, OTS was employed to refine the fabrication process, successfully eliminating weak-performance-graded regions in FGMs fabricated by ITS.

In a study by Wu et al. [62], two types of SS316L/Inconel 718 FGMs were fabricated with horizontal and vertical gradients. Elemental distribution showed a uniform linear pattern. Microstructural and hardness variations were observed between horizontally and vertically graded FGMs due to differences in cooling effects during fabrication.

Nowadays, WAAM process is extensively used by the research community because of its design flexibility, high deposition rate and low cost. Zhang et al.[123] employed twin wire GTAW-WAAM process to develop an Inconel625-high-strength low-alloy (HSLA) Steel functionally graded material (FGM). After fabrication, chemical composition distribution, microstructure, phase evolution, and mechanical properties of developed FGM were studied. Initially, the chemical composition exhibited a graded distribution with increasing proportions of HSLA Steel. In regions with 20% HSLA Steel, the primary dendrite spacing was observed to be the largest, gradually decreasing after that. The predominant microstructure transitioned from columnar dendrites to equiaxed dendrites across the FGM. Furthermore, the precipitation behaviour varied with the HSLA Steel content. Laves phase precipitated along dendrite boundaries when the HSLA Steel content was below 70%, while Nb-rich carbides precipitated when the content exceeded 70%. Regarding mechanical properties, both microhardness and tensile strength exhibited a gradual decrease with increasing HSLA Steel content, except for a notable improvement observed when the proportion of HSLA Steel increased from 70% to 80%, where there was a drastic enhancement from 159HV to 228HV and 355MPa to 733MPa, respectively.

Rodrigues et al.[124] introduces different deposition strategies, named as direct and smooth-type interfaces for the development of metal FGM. Twin-Wire and Arc Additive Manufacturing (T-WAAM) technique was used to fabricate SS316L/Inconel625 FGM. This combination of materials is of interest in chemical plants, oil & gas, and nuclear applications, where high corrosion and wear resistance are essential requirements. Although these properties are superior in Inconel 625, replacing Inconel with stainless steel in strategic regions of structural components can reduce the overall costs and parts' weight. Both direct and smooth transition interfaces were tested and characterized. Microscopic analysis revealed that each interface and the as-built samples had an austenitic matrix, and every sample was well bonded and free of defects. Different types of microstructures evolved at the interfaces due to distinct gradients in composition. X-ray diffraction measurements showed that the smooth-gradient produced secondary phases, such as δ-phase (Ni_3Nb) and carbides, that were not present with the direct interface strategy. Overall, the properties were superior in the FGM with a direct interface, which experienced higher strengths and elongations upon failure. Table 2.3 represent current research work carried out in the field of WAAM process.

Table 2.3: Research work carried out in the field of WAAM process

Author/ Year of Publication	Work done	Findings from research
Martina *et al.* [125]	In this study, authors attempted to mitigate residual stresses induced during WAAM with high-pressure interpass rolling on Ti–6Al–4V components.	Using interpass rolling has been discovered to be an efficient method for mitigating longitudinal residual stress.
Martina *et al*. [126]	Proposed high-pressure interpass rolling to mitigate or completely eliminate distortion and residual stress produced in WAAM fricated. Ti–6Al–4V components	Interpass rolling can be reducing the longitudinal residual stress, but it has geometrical constraint which limits its uses.
Prado *et al*.[127]	The researchers proposed a cheaper metal additive manufacturing technique than laser or electron beam technologies. It was done by combining CMT welding and CNC milling.	The current investigation focused on determining the optimal process parameters for experimentation, including welding speed, current, and voltage.
Bintao *et al*.[47]	The authors examined microstructure, mechanical properties, process flaws, and post-process treatment in the latest WAAM advances.	To make WAAM more competitive, process stability, deposition flaw reduction, and high-quality components with superior mechanical performance are key research areas.
Paskual *et al*.[128]	They proposed a detailed study on WAAM technology, and they found that it achieves high-quality	The components manufactured by WAAM have shown an anisotropy in the mechanical properties, which must be

	parts with very high deposition rates of up to 5 kg/h in stainless steel or 2.5 kg/h in Ti6Al4V alloy.	taken into account during or after fabrication, either by heat treatment or mechanical treatment.
Seow *et al*.[51]	This study examined whether heat treatments improved the microstructure and tensile properties of WAAM IN718. The study also examined the material's tensile anisotropy with its microstructure.	This study found that the micro-segregation of intermetallic compounds during WAAM deposition causes anisotropic mechanical properties.
Ahsan *et al*.[129]	They proposed that GMAW based multi-material WAAM system to fabricate bimetallic components of low carbon steel and AISI 316L stainless steel (SS).	Significant ductility was reduced and the component needs heat treatment, which can be minimized by pressure and friction processing and eliminate the need of heat treatment
Bintao *et al*.[130]	They fabricate Fe-Ni based bimetallic components by WAAM process and found enhanced mechanical strength of the component, which has yet to be reported.	Conventional welding processes can be used. Dendritic grain growth at an angle 60° from the substrate along the feedstock delivery direction was found, which affects the structural integrity of the component.
Ahsan et al.[131]	This study investigated high-entropy alloy (HEA) developed using GTAW-based WAAM process and found near-optimal process parameters.	The findings from the statistical analysis, microstructure characterisation, and mechanical testing indicate that the GTA-WAAM technique, when using pre-alloyed wire, can serve as a viable alternative method for producing the $Al_{0.1}CoCrFeNi$ HEA with a predefined composition.

Senthil *et al*.[132]	This work used CMT--based WAAM to make an FGM of Inconel 825-SS316L wall.	The authors observed continuous cellular dendritic and discontinuous cellular dendritic grain development in the Inconel 825 region. In contrast, the SS316L region primarily consisted of δ-ferrite within the primary austenitic (γ) dendrites.
Kim *et al*.[131]	This study evaluated the use of DED to additively manufacture a functionally graded material (FGM) with a compositional range of Ni-based alloy (Inconel 718) and Fe-based alloy (SS 316L).	Intermetallic and carbide compounds in ceramic oxides created critical holes and cracks. EBSD and XRD analysis of the FGM indicate thermal and residual stresses at grain borders due to constitutional supercooling and columnar-to-equiaxial transition concentrations.
Ghanavati *et al*.[133]	This research examined the solidification behaviour and microstructure evolution in laser additive manufacturing of thin-walled stainless steel 316L-Inconel 718-graded materials.	This study found that the micro-segregation due to nonequilibrium solidification is susceptible to secondary phases of metal carbides and intermetallic compounds of Laves, which may affect the mechanical characteristics.
Kim *et al*.[134]	The authors described a bimetallic additively produced structure (BAMS) made of Inconel 625 (In625) and SS316L. The structure was created using a GMAW WAAM.	The author revealed that during the deposition of dissimilar metals, the localized strain developed at the bimetallic interface due to the difference in thermal expansion coefficients. As a result of these localized strains, dynamic strain hardening was achieved, resulting

		in a higher level of hardness at the interface.
Zhang *et al*.[135]	This author employed DED to create metallic FGMs by blowing metallic powder into the molten pool while gradually altering powder feed rates.	This study examined DED-machining hybrid FGMs. Dry peripheral milling with a tungsten carbide (WC) milling cutter processed the FGM specimen.
Yoo et al.[80]	The investigation involved the execution of the LMD-WAAM method to manufacture a bimetallic structure composed of IN625-SUS304L.	The authors found that LMD-WAAM samples exhibit favorable mechanical properties and do not exhibit any observable cracks resulting from thermal stresses.

2.11 Challenges in WAAM Fabricated Components

Porosity, high residual stress, and cracking are significant concerns, particularly for parts exposed to extreme environments where these defects can lead to failure, such as high-temperature fatigue. The residual stress can lead to distortion of the part, loss of geometric tolerance, delamination of layers during deposition, as well as deterioration of fatigue performance and fracture resistance of the additively manufactured components. Defects in WAAM can arise from various factors, including inadequate programming strategies, unstable weld pool dynamics due to poor parameter setup, thermal deformation resulting from heat accumulation, environmental influences like gas contamination, and other machine malfunctions. Certain materials exhibit susceptibility to specific defects, for instance, titanium alloys are prone to severe oxidization, aluminum alloys may suffer from porosity, steel can exhibit poor surface roughness, and bimetal components are susceptible to severe deformation and cracks. Some common defects, there causes are listed in Table 2.4.

Table 2.4: Common defect associated with WAAM fabrication [47, 102, 134, 136, 137]

Defects	Remarks

Residual stress and deformation	▪ Residual stress is inheritance with WAAM and it should be minimized. ▪ Many post processing techniques have developed to mitigate residual stress such as rolling treatment, interpass cooling and mechanical hammer peening. ▪ Ultrasonic assistance can also reduce the residual stress of additive metal components. ▪ Cr, Ni and Fe alloy has relatively low residual stress.
Porosity	▪ WAAM inherently have low porosity but due to raw materials surface contamination produces pores after solidification. ▪ Heat supplied influences the porosity formation, lack of heat or higher heat input both causes porosity of the additive parts ▪ By excess shielding gas flow rate and by using optimal heat input, it can be reducing, A novel method called hot-wire arc AM can also reduce porosity
Crack and delamination	▪ Excessive heat input will increase the cracking tendency. ▪ heat sensitive material such as magnesium alloy suffer from hot cracks in fusion welding ▪ Bimetallic materials are prone to crack and delamination due to sharp interface.

Therefore, control and minimization of deformation and residual stress in the developed product the various post processing treatments have been employed which is discussed in subsequent section.

2.11.1 Post Processing Treatment in WAAM

In the preceding section, we examined the defects commonly associated with parts fabricated through WAAM. The WAAM processes inherently generate high levels of heat during fabrication, leading to the accumulation of residual stresses in the finished parts. These residual stresses often result in geometric distortions and compromise the integrity of the fabricated components [138]. Therefore, these issues must be addressed. A detailed discussion of these issues will be presented in this section, along with potential mitigation measures.

Kim et al. [134] developed a bimetallic additively manufactured structure (BAMS) consisting of SS316L and Inconel 625 using GMAW-WAAM technique. Subsequently, post-heat treatments were conducted. A Bulk BAMS underwent heat treatment at 970°C to enhance its mechanical properties. This heat treatment prompted a microstructural transition from delta-ferrite to austenite in SS316L, resulting in improved tensile strength compared to the as-built sample, similarly in crystal structure and lattice constant between Inconel 625 and SS316L facilitated epitaxial growth at the bimetallic interface, leading to the formation of coherent columnar grains with identical crystallographic orientation as shown in Figure 2.12. During the heating and cooling process, the distinct thermal expansion coefficients of both materials created localized strains at the bimetallic interface, contributing to dynamic strain hardening and resulting in higher hardness at the interface.

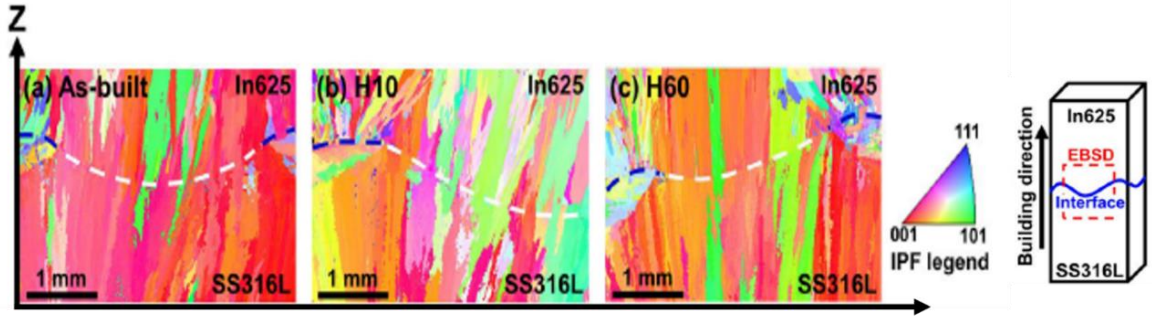

Figure 2.12: EBSD image of inverse pole map for (a) As-built, (b) H10, and (c) H60, All EBSD results were analysed based on the 8 µm step size [134]

Wu et al. [49] proposed forced interpass cooling with the application of compressed CO_2 gas along with WAAM to fabricate a straight wall structure made of Ti6Al4Vas shown in Figure 2.13. This study revealed that increasing the interpass temperature had minimal impact on the deposited metal's microstructural evolution and mechanical properties. However, it led to the widening and flattening of the deposited wall and increased surface oxidation, evident through visible coloration (Figure 2.13 (b)). Conversely, rapid forced cooling using CO_2 between deposited layers resulted in slightly higher hardness values and increased strength (Figure 2.13 (c)). This was attributed to reduced surface oxide and increased density of dislocations due to the formation of large amounts of fine-grained acicular α within the microstructure. Additionally, forced interpass cooling improved deposition properties and enhanced geometrical repeatability and manufacturing efficiency by reducing dwell time between deposited layers.

Colegrove et al.[52] introduced a novel hybrid WAAM technique integrated with interpass rolling (Figure 2.14 (a)). This method incorporates bulk deformation techniques, such as rolling, during the AM process, offering significant advantages, including the reduction of residual stresses and distortion, as well as grain refinement. The latter is especially advantageous for titanium alloys, as it transforms large prior β grains into a fine equiaxed structure (Figure 2.14 (b and c)), resulting in isotropic mechanical properties that may surpass those of the wrought material.

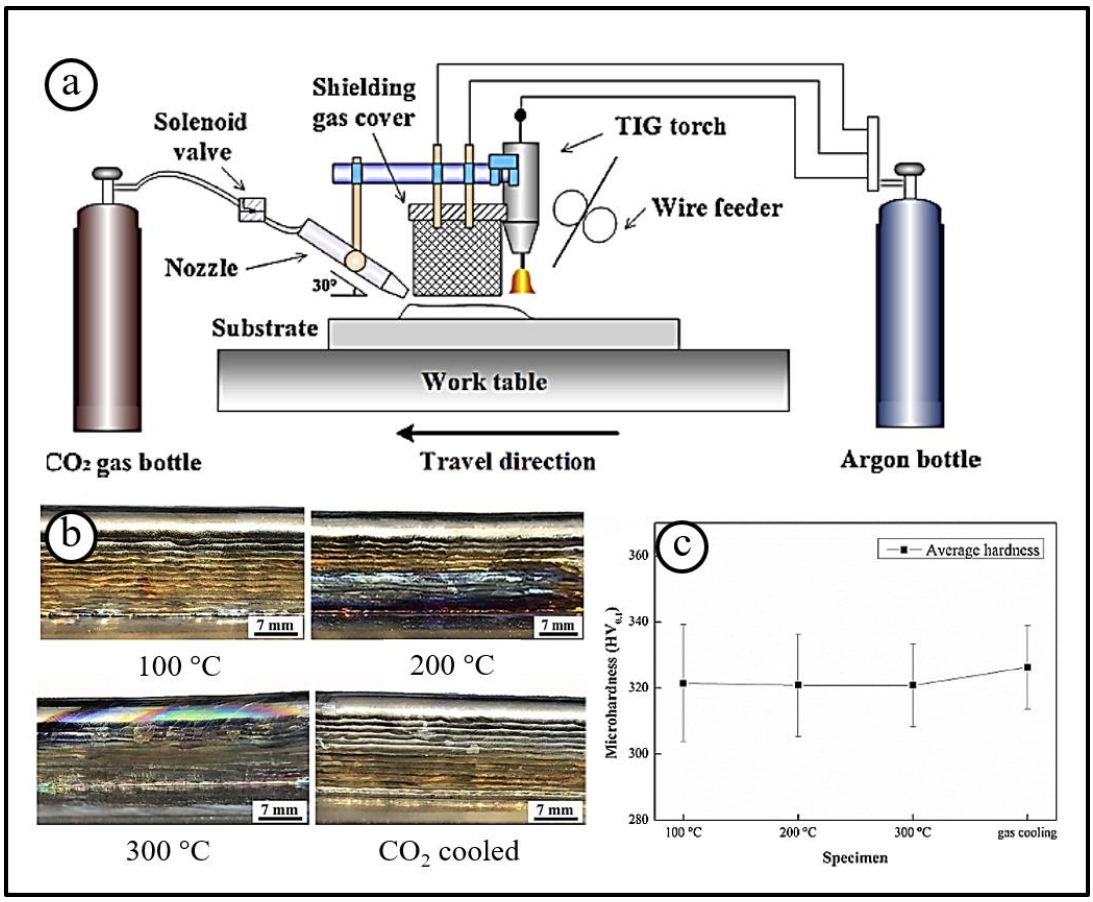

Figure 2.13: (a) Schematic diagram of hybrid forced interpass cooling assisted WAAM, (b) WAAM fabricated wall at different processing condition and (c) average hardness [49]

Hönnige et al. [139] conducted a study to explore the capabilities of novel machine hammer peening (MHP) in process or post process treatment with WAAM (Figure 2.15 (a)). It is an alternate approach of rolling as an interpass cold working technique. These tools offer greater flexibility during operation. The cold working behaviour was evaluated using EBSD (inverse

pole figure maps). The study successfully achieved grain refinement through this approach as shown in Figure 2.15 (b and c).

These studies highlight the significance of both in-process and post-process treatment techniques and their substantial impact on parts fabricated through WAAM. They underline the necessity of such techniques in WAAM for enhancing mechanical and metallurgical properties, mainly through grain refinement and dynamic recrystallization. However, it is acknowledged that every technique has its limitations, indicating the need for further development. In the current research work, a novel hybrid approach combining friction stir processing (FSP) with WAAM has been developed to fabricate FGMs. The subsequent section elaborates on the friction stir processing techniques.

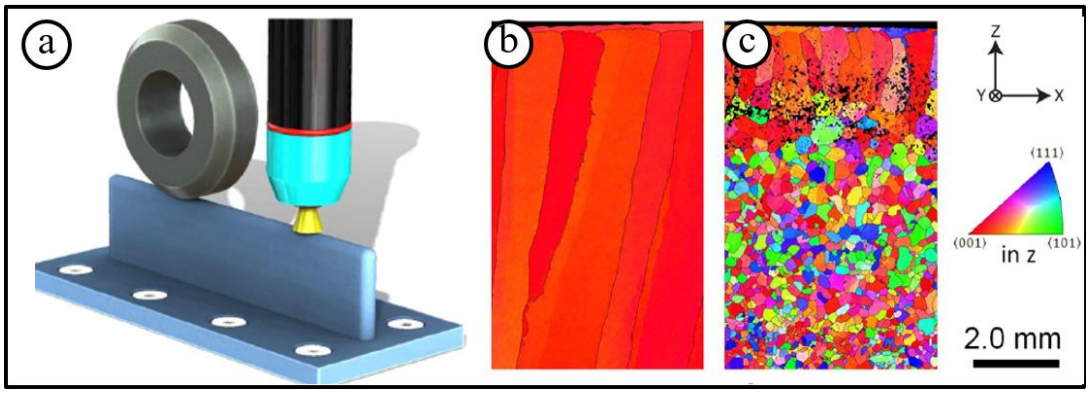

Figure 2.14: (a) Schematic diagram of hybrid interpass rolling assisted WAAM, inverse pole figure β orientation maps of Hybrid WAAM fabricated Ti-6Al-4V (b) as build and (c) with cold rolling applied between every deposited layer [52]

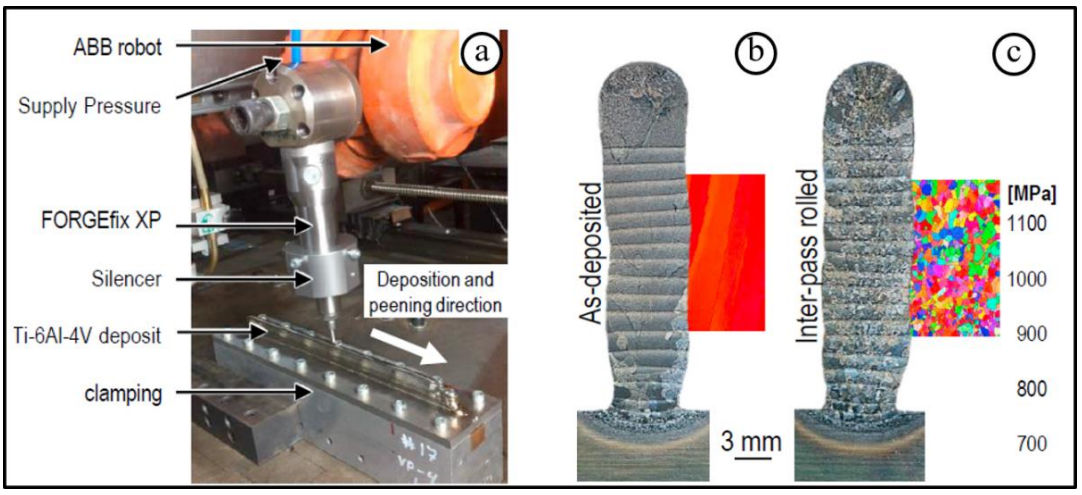

Figure 2.15: (a) Schematic diagram of hybrid machine hammer peening assisted WAAM,

inverse pole figure maps of Hybrid WAAM fabricated Ti-6Al-4V (b) as build and (c) with MHP applied between every deposited layer [139]

2.12 Friction Stir Processing

The Friction stir processing (FSP) is a solid–state hot–shear frictional deformation technique that involves traversing a rotating tool across a workpiece to alter its microstructural properties as shown in Figure 2.16 [140]. This frictional deformation may help to improve the properties of the developed samples. In this processing technique, a rotating pinless tool is moved to the top surface of the fabricated WAAM samples [141]. The heat produced by friction at the shoulder surface softens the WAAM deposited material. This causes plastic deformation, and the flow of plasticized metal as the tool is translated along the processing direction in WAAM processed object. The FSP can change material properties, owing to grain refinement and plastic deformation [142].

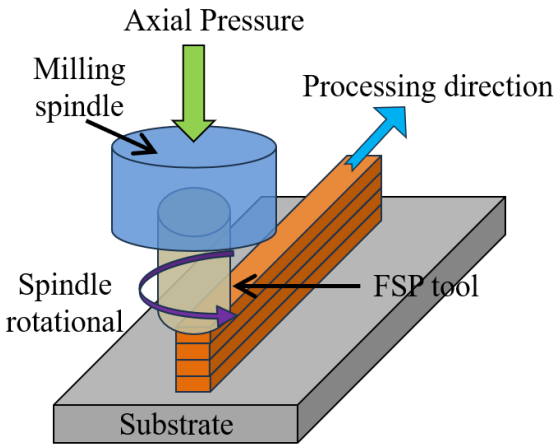

Figure 2.16: Friction stirs processing technique

2.12.1 Advantages of FSP

1. Produce fine-grained equiaxed microstructures [143]
2. Eliminate the majority of liquid-based defects
3. Can be used for a broad material range of ferrous and nonferrous metals [144]
4. Easy to operate and does not involve any environmental pollution
5. High mixing ability process

6. FSP is an easy and high-speed process, so it can provide higher efficiency

2.13 RESEARCH GAPS AND PROBLEM FORMULATION

Based on the literature survey, the following problems have been identified:

1. It is observed from the literature review that a feasibility study is required for the development of FGM using multi wire feed system with GTAW-WAAM processes.

2. The continuous variation of composition and structure is crucial for the performance of FGMs. However, there is limited research focused on the development of such FGMs using WAAM.

3. Friction Stir Processing (FSP) as a post-process treatment has not been investigated in details after WAAM manufactured components.

4. The use and effect of an active cooling environment with FSP during the development of FGMs has not been investigated in details.

5. The comparison of mechanical and metallurgical properties of developed FGMs with and without post-process treatment using FSP is less explored.

2.14 RESEARCH OBJECTIVES

On the basis of research gaps identified through the available literature survey, the proposed research plan was developed and the research objectives have been established, which are given below:

1. Study on feasibility analysis for development of FGM through WAAM process.

2. Optimization of the processing parameters for FGMs development by GTAW process.

3. Optimization of friction stir processing parameters for developed FGMs at optimum conditions.

4. Mechanical and metallurgical characterizations of developed and processed FGMs by using various techniques

2.15 METHODOLOGY

Developing a methodology for WAAM typically involves a series of steps to ensure the successful fabrication of a part or product. The detailed methodology followed while performing research work and experiments according to objectives is discussed and shown in Figure 2.17.

Objective 1: The first objective is to conduct a feasibility analysis for the development of functionally graded materials (FGMs) through the Wire Arc Additive Manufacturing (WAAM) process. Based on the literature review, suitable materials were selected for the fabrication of FGMs. Additionally, numerous trial experiments were performed for determining the most influencing bead characteristics welding process parameters. Subsequently, a sufficient number of trials were conducted for fabrication of multi-layer FGM of the selected material and identified most influencing welding process parameters.

Objective 2: The second objective is to optimize the processing parameters for the development of FGMs by using the Gas Tungsten Arc Welding (GTAW) process. Utilizing the findings on the welding process parameters from trial experiments, the optimal range of welding parameters were determined. The single layer and multi layers samples were deposited accordingly.

Objective 3: Under this objective, Initially, the trial experiments were conducted to select the optimal range of FSP parameters. The FGMs were processed at the optimize Friction Stir Processing (FSP) parameters.

Objective 4: The fourth objective is mechanical and metallurgical characterizations of developed and processed FGMs by using various techniques. In GTAW-WAAM and GMAW-WAAM process, different FGMs (continuous and discontinuous) were fabricated. After fabrication, the metallurgical and mechanical examination were performed. The microstructure of deposited FGMs were analyzed through an optical microscope (OM) and scanning electron microscopy (SEM). For finding the presence of precipitates developed in a deposited sample, etched samples were examined by using SEM and energy dispersive spectroscopy (EDS). To observe the grain boundaries, electron backscatter diffraction (EBSD) is used. For mechanical characterizations of developed FGMs, microhardness and tensile tests were performed.

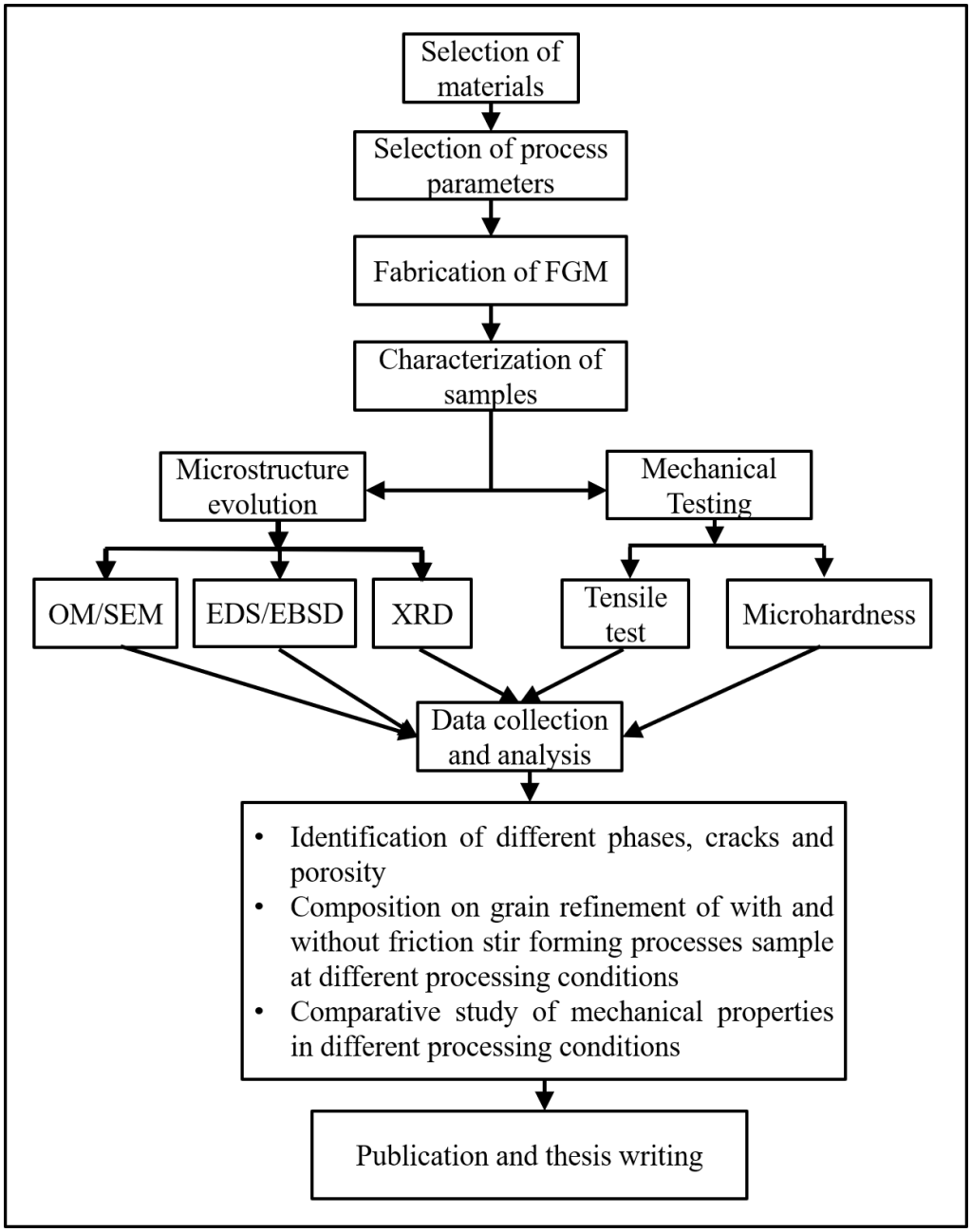

Figure 2.17: Proposed research methodology used in the present research work

SUMMARY

This chapter thoroughly overviews the latest research discoveries regarding FGM achieved through diverse additive manufacturing methods. Through literature review gap and problem formulation have been done. The based upon gap observed from literature review, objectives of research work have been decided.

Chapter 3

MATERIAL SELECTION AND THEIR CHARACTERIZATIONS

3.1 SELECTION OF MATERIALS

Ni-based superalloys are the most popular material studied by the AM research community, mainly due to their high strengths at elevated temperatures and high fabrication cost developed by using traditional methods [145]. The Ni-based superalloys exhibit superior mechanical properties, oxidation resistance, and microstructural characteristics at high temperatures [146]. Because of their remarkable strength and oxidation resistance at temperatures above 550°C, nickel-based superalloys are widely used in the aerospace, aeronautical, petrochemical, chemical, and marine industries [127]. In recent years, various nickel-based superalloys, such as Inconel 718, Inconel 625 have been studied and utilized in the WAAM process. In the development of Ni-based FGMs, specific alloys such as Inconel 625, ERNiCrMo-10, Nichrome 80/20, and pure Ni weld spools were selected for the present work. The criteria for the selection of these elements are as follows;

3.1.1 Inconel 625

Inconel 625 is a wrought nickel-based superalloy that gains its strength primarily from adding carbon, chromium, molybdenum, and niobium [147]. It was designed to operate at temperatures lower than 973 K and combines good manufacturing properties with the high strength that is characteristic of age-hardening nickel-based alloys. This material is used in various sectors, including aerospace, aviation, marine, chemical, and petrochemical, have used it.

3.1.2 ERNiCrMo-10

ERNiCrMo-10 is a solid nickel-based welding wire often used for overlay cladding and welding dissimilar metals, particularly in applications requiring high strength, corrosion resistance, and elevated temperature performance [148]. This alloy typically contains nickel (Ni), chromium (Cr), molybdenum (Mo), and other alloying elements, offering excellent

corrosion resistance and mechanical properties. It is commonly employed in petrochemical, aerospace, and marine engineering industries for joining and repair applications where durability and reliability are critical.

3.1.3 Nichrome 80:20

Nichrome 80/20 is a popular alloy consisting of 80% nickel (Ni) and 20% chromium (Cr). It is renowned for its exceptional resistance to high temperatures and oxidation. It is ideal for heating elements, electrical resistors, and other applications requiring stable electrical resistance over a wide temperature range. Nichrome 80/20 is widely used in industries such as appliance manufacturing, aerospace, and automotive, where precise control of temperature and resistance is essential. Its excellent mechanical properties, corrosion resistance, and ductility make it a versatile material for various engineering applications.

3.1.4 Pure Nickel

The nickel (Ni), is a metallic element known for its excellent corrosion resistance, high ductility, and good thermal and electrical conductivity. It is typically used in various industrial applications where these properties are beneficial, such as in batteries, electroplating, alloying, and in the production of batteries. Its corrosion resistance makes it valuable in chemical processing equipment, while its electrical conductivity makes it useful in electronics and electrical engineering applications.

These materials are chosen based on their unique properties and suitability for specific applications. By incorporating them into the FGM with varying compositions throughout the deposited height, a gradient of properties can be achieved, optimizing performance for different regions within the material.

3.1.5 Selection of Substrate Material

In this experiment, the FGM was deposited onto a mild steel (MS) substrate measuring 200mm x 50 mm x 16mm. The mild steel was chosen as the substrate material due to its availability, low cost, and excellent weldability. Additionally, Ni-based alloys can be readily welded with mild steel substrates.

3.2 CHARACTERIZATION TECHNIQUES

The microstructure, elemental composition, phase orientation, grain size, and hardness significantly influence the response and performance of any material. Therefore, it is crucial to characterize the materials before processing them. While several techniques are available for material characterization, only relevant techniques were employed in this study.

The materials were thoroughly characterized for their metallurgical and mechanical characteristics. This involved utilizing scanning electron microscopy (SEM), energy dispersive X-ray spectroscopy (EDX), X-ray diffraction (XRD), inverted metallurgical microscopy (OM) equipped with image analysis software, Vicker's microhardness testing and universal testing machine (UTM). Detailed specifications and characteristics of the equipment used for characterization are provided in the Appendix (Figure A1-A5).

3.2.1 Metallurgical Characterization

Various instruments /equipment were used for metallurgical characterization of feed stock materials and developed Ni-based FGMs. The details of various instruments used in metallurgical characterization is presented in this section.

3.2.1.1 Optical Microscopy

The specimens for optical microscopy were first finely cut using wire EDM. After cutting, metallographic samples were ground and polished according to standard procedures, then etched by a reagent containing 70% vol. of HCl and 30% vol. of HNO_3. The microstructure has been examined by using optical microscope (OM) (maker: Radical Scientific Equipment, Model: RMM-8T). An illustration of the OM facility is provided in Figure A-1 in Appendix A. These optical microscopy techniques provide valuable insights into the porosity and solidification microstructure of the developed FGM, facilitating comprehensive characterization of the material properties.

3.2.1.2 Scanning Electron Microscopy

The metallographic and fractographic observation of the polished sample and fractured tensile specimens were carried out using a Sigma - ZEISS Field Emission scanning electron

microscope (SEM) under second electron inspection (SEI) mode, operated at 20kV. The chemical composition of the finely polished sample was measured using the Bruker, QUANTAX 200 energy disperse spectrometer (EDS) detector on the SEM. An illustration of the SEM facility is provided in Figure A-2 in Appendix A. The composition testing points were located approximately 50 μm laterally from the hardness testing points.

3.2.1.3 Electron Backscatter Diffraction

Electron Backscatter Diffraction (EBSD) (Model No: Bruker, QUANTAX EBSD 400i) is an advanced microscopy technique used to analyze the crystallographic structure and orientation of materials at a microstructural level. By directing a focused electron beam onto the sample surface, the interaction of electrons with the crystal lattice causes backscattered electrons, whose patterns are then analyzed to determine crystallographic information such as grain size, grain orientation, and phase identification. EBSD provides valuable insights into material properties, including texture, deformation, and recrystallization behaviour, making it vital tool in materials science and metallurgy research.

3.2.1.4 X-Ray Diffraction

X-ray Diffraction (XRD) is a non-destructive and rapid analytical technique primarily employed for phase identification of crystalline materials. In an XRD setup, a cathode ray tube generates X-rays, which are filtered to produce monochromatic radiation directed towards the sample. When incident X-rays interact with the sample, diffracted rays are produced, satisfying Bragg's Law ($n\lambda = 2d\sin\theta$). The Bragg's law describes the relationship between the wavelength of electromagnetic radiation, the diffraction angle, and the lattice spacing within a crystalline sample. The resulting XRD pattern is generated by detecting, processing, and counting these diffracted rays. Software such as X-pert High Score is commonly utilized to identify peaks by comparing the obtained data with reference patterns stored in databases like the latest ICDD (International Centre for Diffraction Data) database. An illustration of the XRD facility is provided in Figure A-3 in Appendix A. Phase characterization was performed using an X-Ray Diffractometer (XRD) (Maker: PANalytical, Almelo, Model: X'Pert PRO) using monochromatic Cu Kα radiation (λ=1.5418 Å); scanning angle (2θ) was set from 10° to 100° with 5 degree/min scanning speed. In the XRD measurements of the present research, the X-ray tube voltage and loading current was set at 35 kV and 28.6 mA, respectively.

3.2.1.5 Residual Stress Measurement by using X-Ray Diffraction

The residual stress was determined using X-ray diffraction techniques, which is represented the arithmetic average stress within a defined volume of material. This volume is determined by the irradiated area, and the X-ray beam's penetration depth. The penetration depth is governed by the linear absorption coefficient of the material used for the radiation, which can vary significantly. In iron, nickel and aluminum-based alloys, about 50% of the radiation is diffracted by a layer approximately 0.005 mm deep when using commonly employed radiations for strain measurements. This shallow penetration depth enables the determination of macro and microscopic residual stresses as functions of depth [149]. Theoretically, any interplanar spacing could be utilized to obtain strain within the crystal lattice, the range of available wavelengths from commercial X-ray tubes constrains the options to a select few planes. The selection of a diffraction peak for residual stress assessment notably influences the accuracy of the technique. Precision increases with higher diffraction angles, typically necessitating angles 2θ exceeding 120° for practical applications. The Figure 3.1 illustrates the diffraction of a monochromatic x-ray beam at a high diffraction angle (2θ) from the surface of a stressed sample at two orientations relative to the X-ray beam. The angle ψ defines the orientation of the sample surface, representing the angle between the normal of the surface and the bisector of the incident and diffracted beams, which is also the angle between the normal to the diffracting lattice planes and the sample surface.

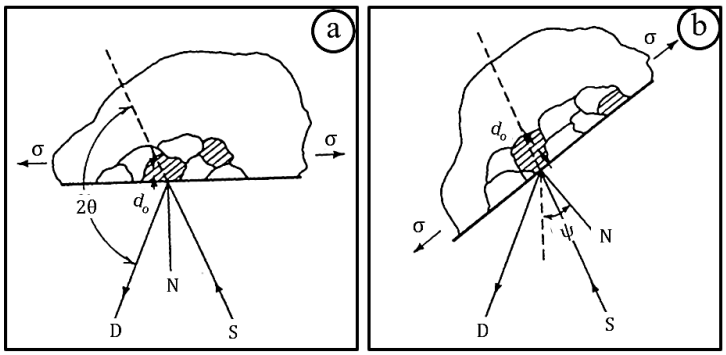

Figure 3.1: Schematic diagram showing the position of sample with reference to XRD detector at (a) ψ = 0. (b) ψ = ψ (sample rotated through some known angle ψ) (D = x-ray detector, S = x-ray source and N = normal to the surface) [150]

In Figure 3.1(a), the sample is depicted in the ψ = 0 orientation. Tensile stress in the sample induces Poisson's ratio contraction, causing a reduction in the lattice spacing and a slight

increase in the diffraction angle, 2θ. Upon rotation of the sample through a known angle ψ (as shown in Figure 3.1(b)), the tensile stress at the surface increases the lattice spacing compared to the stress-free state, resulting in a decrease in 2θ.

3.2.2 Mechanical Characterization

Generally, the experiments conducted in order to investigate mechanical properties of the FGM in the present research work were Vicker's microhardness testing and tensile testing). The basic parameter setups of the testing devices are shown in this section.

3.2.2.1 Vicker's Microhardness Test

Hardness is a measure of a material's resistance to localized plastic deformation resulting from force or abrasion. Typically, materials with higher hardness exhibit greater strength and wear resistance. However, they may also tend to be more brittle and susceptible to fracture. The microhardness of the developed FGMs was assessed using a Vicker's microhardness tester, depicted in Figure A-4 of Appendix A. All the measurements were performed using a load of 200 g applied for 15 s in the gap of 0.5 mm along the height. To minimize error in hardness results, three indentations were made laterally across each layer (50 μm on either side of the central indentation mark), and the average microhardness value was recorded.

3.2.2.2 Tensile Test

Similar to hardness testing, the tensile properties of the multi-layer FGM samples were evaluated at room temperature. For this purpose, a universal testing machine (Make: Enkay Enterprises, Model: EKE591 with a 10 kN loading capacity), depicted in Figure A-5 of Appendix A was utilized. Subsequently, SEM images of the fracture surfaces were acquired for the fracture analysis. The extraction location and direction of the tensile specimens inside the buildup walls will be specified in the corresponding experimental chapters. The tensile specimens were fabricated horizontally in accordance with ASTM E8M standards (Figure 3.2). All tensile sample were then tested at 0.1 mm/min displacement rate. The average tensile value of the three samples from each direction was determined.

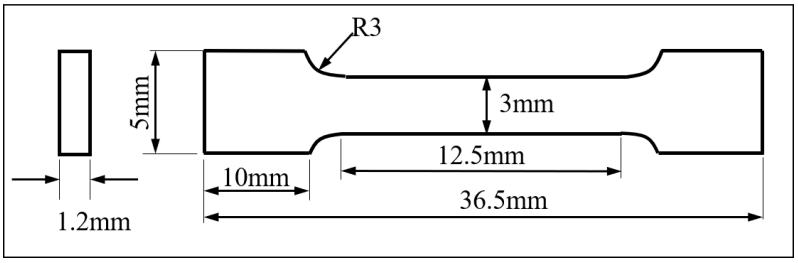

Figure 3.2: Tensile sample dimensions according to ASTM E8M standard

3.3 CHARACTERIZATION OF THE MATERIALS

3.3.1 Characterization of Raw Material

The Inconel 625, ERNiCrMo-10, Nichrome 80:20 and pure nickel wire spools were characterized in its as-received condition to determine its purity and mechanical properties. The spectrometer (Make: WAS, Model: Foundry Master), universal testing machine and microhardness tester were utilized to evaluate the chemical composition, tensile strength and Vicker's microhardness of the substrate material. The results are presented in Table 3.1 and 3.2.

Table 3.1: Percentage composition of alloying element of filler wires

Metal wire	Inconel 625	ERNiCrMo-10	Nichrome 80/20	Ni
Ni	58.00 %	57.00%	80.00%	100%
Cr	20.00%	21.00%	20.00%	-
Mo	9.00%	14.00%	0.00	-
Residues (Fe, Ti, Nb, C, S)	13.00%	08.00%	0.00	-
Wire Diameter (mm)	1.2	1.2	1.2	1.2

Table 3.2: Mechanical properties of wire spools

Metal wire	Inconel 625	ERNiCrMo-10	Nichrome 80/20	Ni
Ultimate tensile strength (MPa)	895±15.3	789.65±12.4	652±12	448±10
Yield strength (MPa)	515±9.6	462.51±8.5	295±5	148±5
Elongation (%)	39±6.1	40.10±3.5%	41±3 %	43±5
Hardness (HV)	210±5.1	223.47±6.2	205±5	134±3

3.3.2 FGM Characterization

The samples for characterizations of developed FGMs at optimized processing parameters were extracted by using wire electric discharge machine (EDM). The extracted specimen underwent initial grinding using emery papers of various grades: 100, 150, 220, 320, 600, and 800. Subsequently, the specimen surface was polished using fine-grade emery papers, starting from 1000 and progressing in series (1500, 2000, and 2500) up to 3000. Afterwards, the specimen underwent polishing using a diamond paste with abrasive particle size of 0.25 μm, applied onto a soft velvet cloth mounted on a disk polisher. The diamond polishing paste was adhered to the velvet cloth using a diamond-lapping compound sprayed onto the cloth. This process aimed to achieve a mirror-like surface finish and eliminate any remaining scratches.

SUMMARY

This chapter provides insights into selection of materials for the development of Ni-based FGM. It also includes different metallurgical and mechanical characterization techniques for testing the raw materials and developed FGM. Finally, selected materials, their compositions, and mechanical properties are presented.

Chapter 4

EXPERIMENTAL PROCEDURE AND FEASIBILITY FOR FGM DEVELOPMENT

The addition of chromium (Cr) and molybdenum (Mo) into pure nickel (Ni) enhances its properties such as corrosion resistance, strength, ductility, toughness, and wear resistance. By varying composition of these elements, the properties of developed material can be modified which can withstand harsh environments. Thus, in this study, a nickel base functionally graded material (FGM) has been developed by using WAAM process and the compositional gradient is designed by altering the proportions of constituent alloying elements. The effect of gradual variation of alloying elements on metallurgical and mechanical properties of developed FGMs has been studied. The post deposition FSP of deposited sample has also been carried out to see the effect of frictional deformation on WAAM fabricated samples.

4.1 EXPERIMENTAL SETUP

4.1.1 WAAM Setup

The GTAW-WAAM setup is shown in Figure 4.1. The Figure 4.1(a) depicts schematic representation of GTAW-WAAM. The setup consists of commercial GTAW welding machine (Make: J K MACHINE TOOLS (GUJ) PVT.LTD, Model: JK GTAW-400), welding torch with non-consumable tungsten electrode and argon gas cylinder. A regulator is fitted in cylinder to control argon gas flow rate and pressure. Welding current and voltage controller is inbuilt at the top of welding machine highlighted in yellow doted rectangular box Figure 4.1 (b). The mild steel plate of size 200 mm x 100 mm x 16 mm was used as a substrate on which the multi layered FGM was deposited.

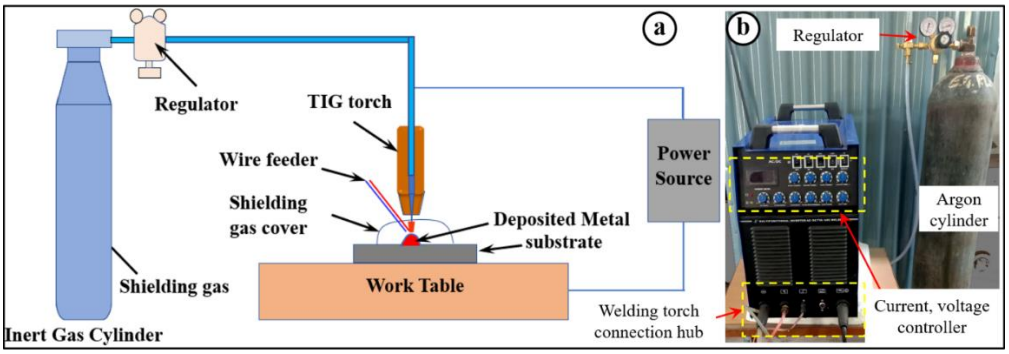

Figure 4.1: (a) schematic representation of GTAW based WAAM set up, and (b) AC/DC GTAW welding machine

4.1.2 FSP Setup

The developed FGM samples are also gone through the post processing frictional deformation and this deformation has been done in customized FSP setup. This setup utilizes a traditional vertical milling machine (Make: HMT Limited, Pinjore India: Model-FN2V), as illustrated in Figure 4.2. The detailed specifications of this machine are comprehensively outlined in Table 4.1. A non-consumable, pinless tungsten carbide tool was used for FSP. This tool is fitted on the spindle of milling machine rigidly by using standard collets. The dimensions of the tool used for FSP is presented in Figure 4.2 (c).

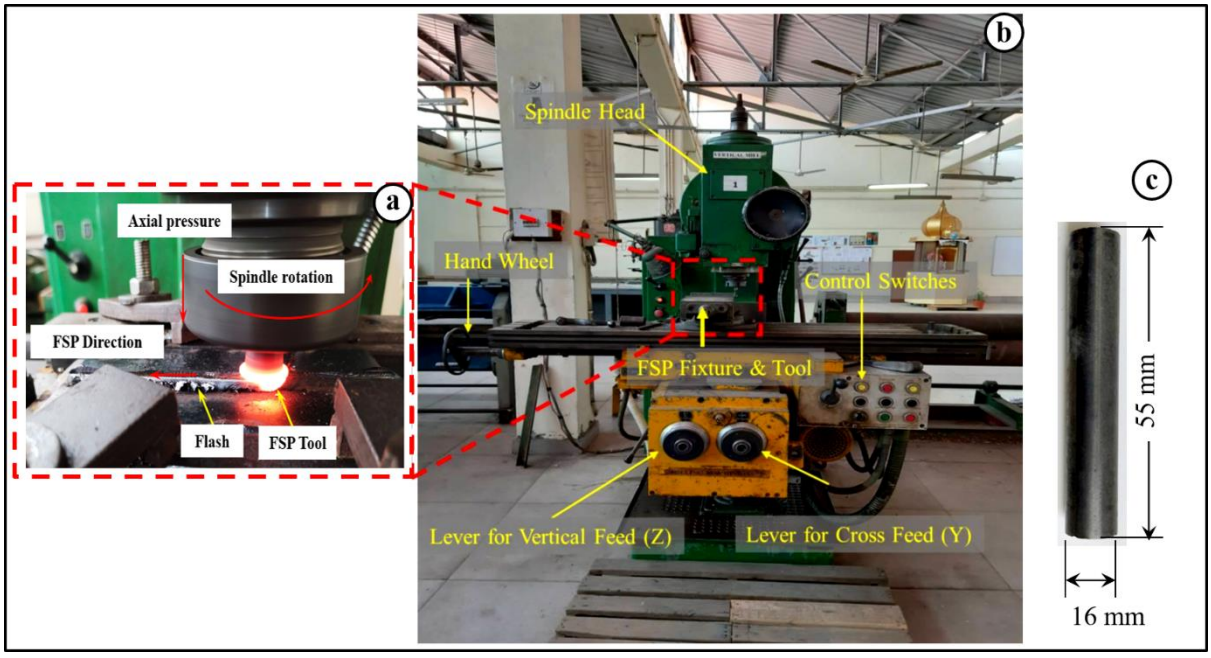

Figure 4.2: The details of FSP setup showing; (a) FSP, (b) vertical milling machine and (c) tool used

Table 4.1: Specifications of the vertical milling machine

Machine Model			FN2/FN2E (H, U, V)
Overall dimensions (L x W)		mm	1520 x 310
Clamping area (L x W)		mm	1350 x 310
Power operated table traverses	longitudinal	mm	800
	transverse	mm	265

	vertical	mm	400
Number of spindle speed			18
Speed range		rpm	35.5-1800
Main Motor		kW/rpm	5.5/1500
Feed Motor		kW/rpm	1.5/1500

The primary objective of this research, is the fabrication of metal-based Functionally Graded Material (FGM) by utilizing the direct energy deposition (DED) approach. The initial trial experiments were conducted for selecting the optimal welding and FSP process parameters. After optimizing these parameters, the minimum number of layers required for performing FSP were optimized by hit and trial experimentations. Afterwards, experimentations were performed, which focused on the development of both continuous and discontinuous FGMs by using GTAW-WAAM under different cooling conditions. A discontinuous trimetallic FGM was also fabricated by using GMAW-WAAM process. Subsequently, mechanical and metallurgical characterizations were conducted on the fabricated samples. The detailed step by step procedure is shown in Figure 4.3.

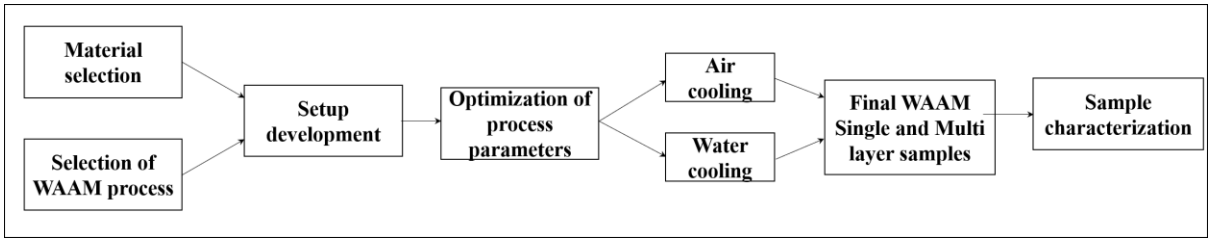

Figure 4.3: illustrates the key steps of this process

4.2 PROCESS PARAMETERS OPTIMIZATION

4.2.1 Gas Tungsten Arc Welding Parametric Investigation

For the development of Functionally Graded Materials (FGM), welding parameters were optimized by depositing a single layer at different welding currents and voltages, as illustrated in Figure 4.4. For the optimization of welding parameters, a single layer samples were deposited at different set of welding currents and voltages, as illustrated in Figure 4.4. After depositing nine single layers, the deposited layer quality is evaluated on the basis of visual inspection and weld bead characteristics. The macroscopic observations showed that porosity defects occurred when the welding voltage ranged from 13 V to 17 V. However, beyond 17 V, no porosity was observed, indicating a significant increase in heat input. While, defect-free

layers were achieved with higher voltages, it was also observed that excessive heat input led to an increase in weld bead size. In additive manufacturing, a larger weld bead is generally not preferred. Therefore, based on considerations of deposited layer smoothness, absence of defects, and appropriate weld bead size the process parameters were optimized. The optimized GTAW welding parameters are presented in Table 4.2.

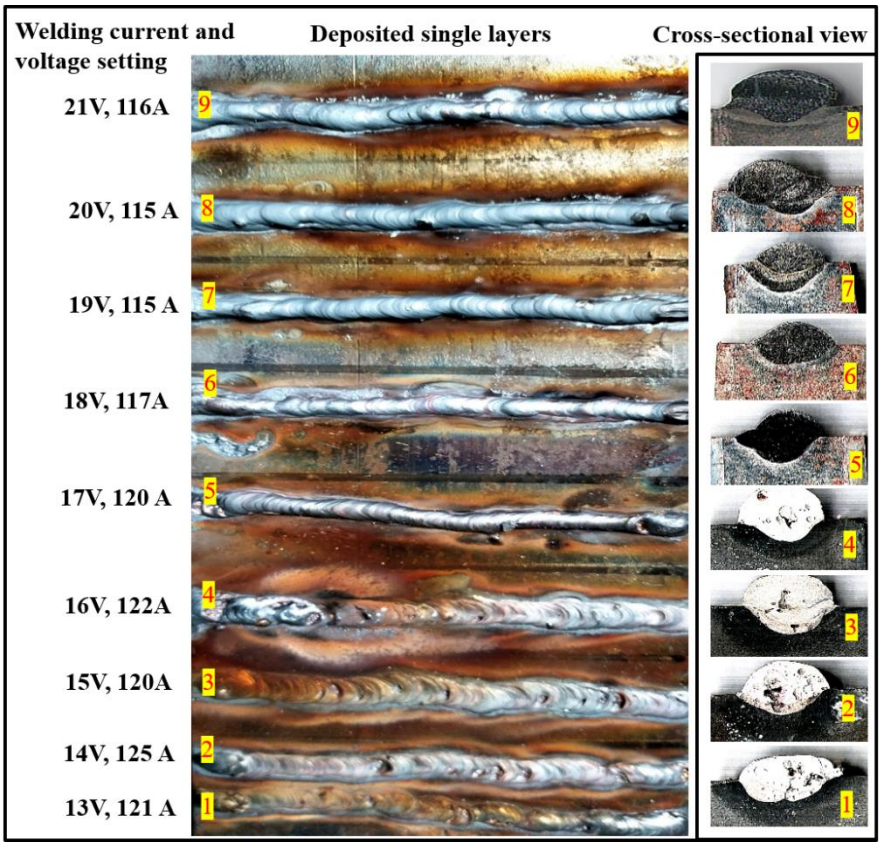

Figure 4.4: GTAW deposited single layer samples at different welding parameters and their cross-sectional view

Table 4.2: Selected Parameters for deposition of material for fabrication of FGM.

Process parameters	Values
Welding current	115 A
Voltage	19 V
Welding speed	Manual
Shielding gas	Argon (> 99% pure)
Gas flow rate	15 *l*/min

4.2.2 Friction Stir Process Parametric Investigation

The single-layer samples were deposited on bead on plate configuration with optimized GTAW-WAAM process parameters as illustrated in Table 4.2 and **s**ubsequently, FSP was conducted. It is observed from the literature [151], that the primary influencing parameters during FSP is tool rotational speed. Hence, the experiments were carried out at varying rotational speeds ranging from 350 to 1120 rpm with a traverse speed of 100 mm/min. After carrying out the experimentation of FSP on bead developed by WAAM process (shown in Figure 4.5 (a-e)), the cross-section of the FSP components were further analyzed for grain size and defects developed at the surface of the FSP components were investigated by visual inspection.

It is well known that the heat generation during FSP fundamentally increases with increase in tool rotational speed [152]. As speeds increases from 350 to 560 rpm, it results in insufficient frictional deformation, due to lack of heat generation (Figure 4.5 (a-b)). Conversely, at a speed of 710 rpm, sufficient of heat generation are during FSP, which is indicated by a blueish processed surface. Hence, sufficient amount of frictional deformation can take place, which is required to cause for grain refinement (Figure 4.5 (c)). However, at higher speeds of 900 rpm and 1120 rpm, very high amount of heat produced, along with excessive flash and burnt surfaces are observed, which are undesirable in processed components (Figure 4.5 (d-e)). Therefore, 710 rpm is considering to be optimum value for FSP. The finalized FSP parameters are represented in Table 4.3.

Figure 4.6 illustrate the correlation between average grain size and FSP tool rotational speed. It is evident from this figure that the WAAM deposited samples shows large grains in as-deposited condition. The grain size reduces due to dynamic recrystallization after FSP at various tool rotational speeds as illustrated in Figure 4.6. It is observed that as the tool rotation increases from 350 to 710 rpm, the grain size decreases due to increases dynamic recrystallization. Further increase in tool rotation from 710 rpm, enhances the heat input, triggering grain coarsening in samples S4 and S5. This surplus of heat culminates in the formation of larger grains, undermining the pursuit of a fine-grain structure through FSP.

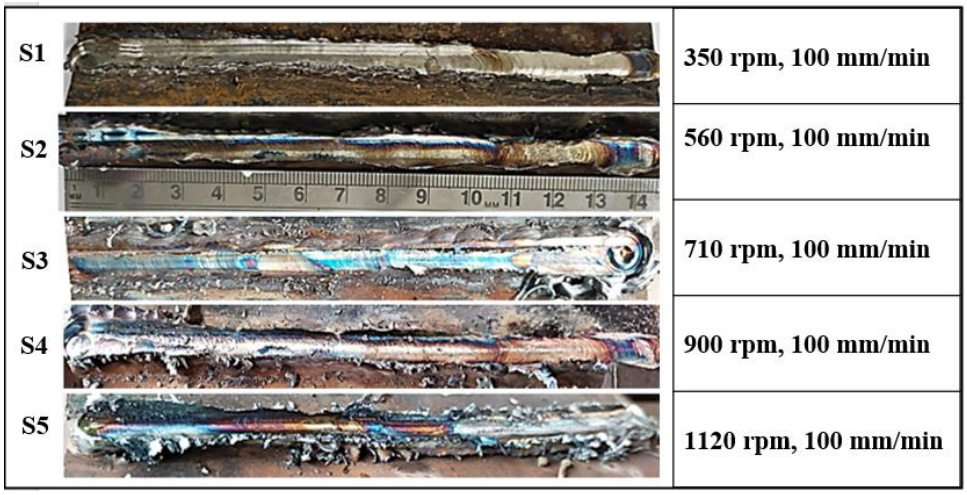

Figure 4.5: FSP processed sample at different rpm; (S1- 350, S2- 560, S3- 710, S4- 900, and S5-1120) with a constant feed of 100 mm/min

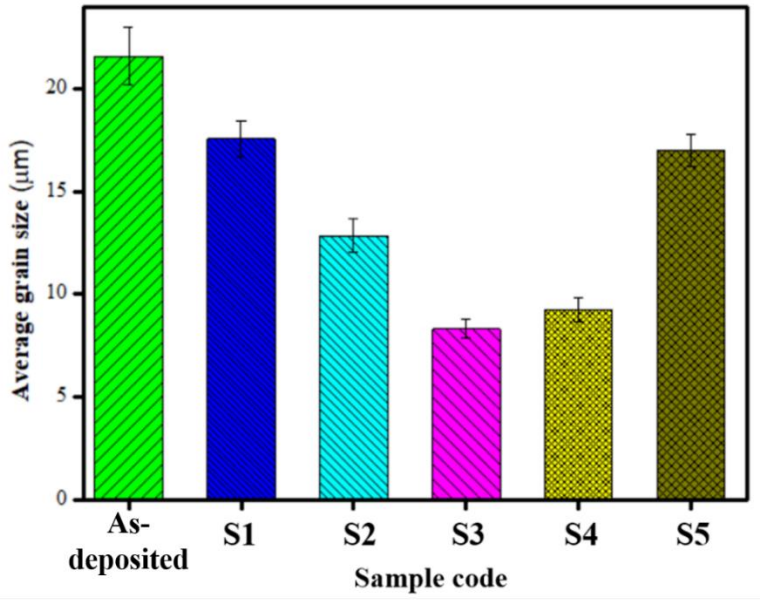

Figure 4.6: Average grain size (μm) of as-deposited and FSP samples (S1-350 rpm, S2-560 rpm, S3-710 rpm, S4-900 rpm and S5-1120 rpm)

Table 4.3: Friction stir processing parameters and their values

FSP parameters	Value
Speed	710 rpm
Feed	100 mm/min
Depth of plunge	0.5 mm
Shoulder diameter	16 mm

Tool tilt angle	1.5 degree
Tool material	Tungsten carbide
Tool shape	Pin less cylindrical flat shoulder

Once the FSP parameters are finalized, it is necessary to analyze the number of layers over which the FSP will be employed. This is because, a drastic reduction in height was observed from visual inspection of the single-layer processed sample. Thus, for multilayer deposition by WAAM, it becomes important to determine the appropriate number of layers after which FSP will be performed. This ensures the minimization of the effects of thermal cycling in the WAAM process and reduces the loss of height as a result of the FSP.

The Figure 4.7 (a-b) depicts the two, three, and four-layer samples, along with their cross-sections. The variation in height of the sample before and after FSP has been presented in Figure 4.7 (c). The reduction in sample height for the two, three, and four layer samples after FSP is observed to be 14.65 ± 1.5%, 8.4 ± 1.3%, and 6.4 ± 0.9%, respectively. The microhardness and residual stress results are presented in Figure 4.8 (a-b). These results show a significant increase in microhardness values and a reduction in residual stress after FSP is performed. In the two, three, and four-layer samples, percentage increases in hardness of 34.36 ± 5.4%, 49.15 ± 4.5%, and 31.16 ± 5.9%, respectively, are observed. Similarly, reductions in residual stress in the two, three, and four layer samples of 86.07 ± 7.4%, 89.27 ± 9.5%, and 42.85 ± 6.9%, respectively, are observed. After detailed analysis, it is concluded that performing FSP after three layers yields a better result.

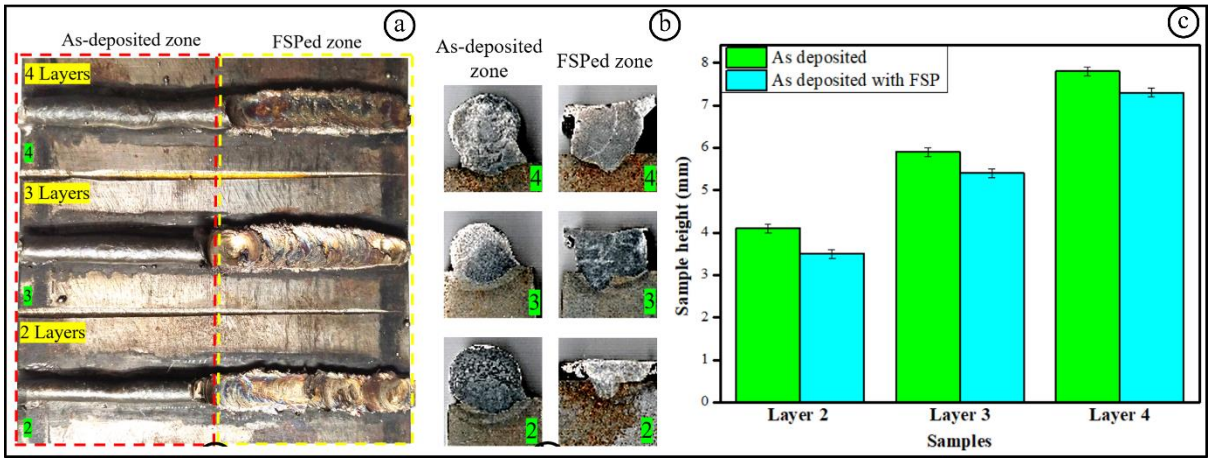

Figure 4.7: (a) samples with and without FSP, and (b) cross sectional view and (c) Sample height before and after

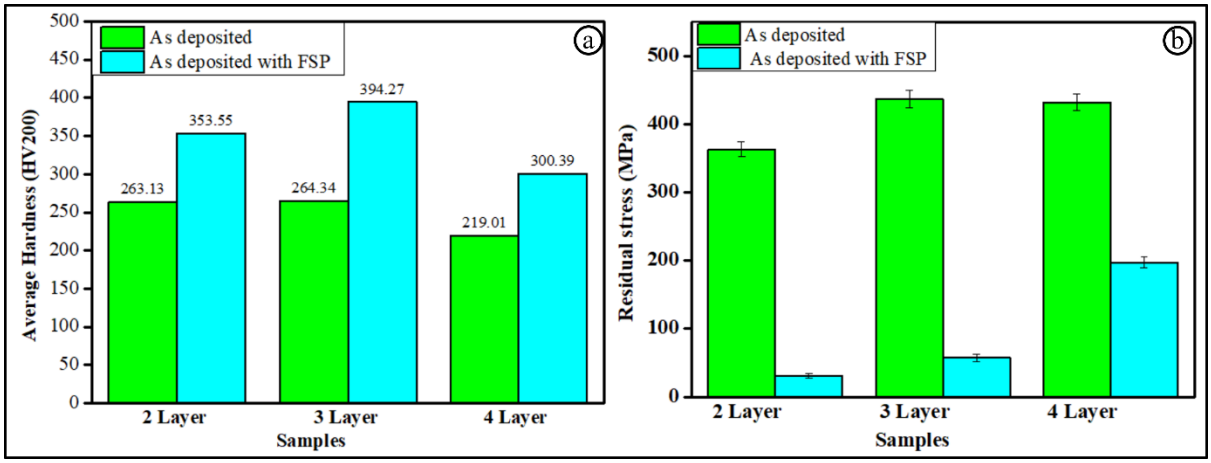

Figure 4.8: Hardness of as deposited with and without FSP and (b) Residual stress of as deposited with and without FSP

4.3 FGM SAMPLE PREPARATION STRATEGY

Two distinct deposition strategies were employed in the development of Nickel (Ni)-based Functionally Graded Materials (FGMs).

FGM Type-I: In the first approach, the deposition involved varying the proportions of nickel and chromium along the height of the specimen. This aimed to examine the influence of elemental variation on the mechanical and metallurgical properties of the resulting FGM. Subsequently, post-processing via friction stir processing (FSP) was implemented to further, investigate its effects on the mechanical and metallurgical behavior.

FGM Type-II: In this method, the deposition process entailed varying the percentages of nickel, chromium, and molybdenum along the height of the specimen. The objective was to assess the impact of continuous variation of alloying elements on the mechanical and metallurgical properties of the designed FGM. Additionally, FSP was applied with different cooling media to explore their effects on the engineered FGM.

These strategies not only enable a systematic examination of the influence of elemental variation on FGM properties. This investigation also provides insights into the role of post-processing techniques like FSP and the effects of different cooling media on the resultant material.

4.3.1 FGM Type-I: FGM by varying Ni and Cr Elements along the Deposition

In FGM Type-I, the composition of each layer was determined by using equations (i), (ii), and (iii). Details regarding the tailored alloy compositions of each layer for the development of the FGM and the combinations of wires utilized to achieve these compositions are outlined in Table 4.4.

For determination of percentage of nickel, Eq. (*i*) is used as given below

$$Ni\ (\%\ wt\ ) = \left[\frac{\frac{\pi d_i^2}{4}\times \%\ vol.\ of\ Ni\ in\ wire\ i \times n_i + \frac{\pi d_j^2}{4}\times \%\ vol.\ of\ Ni\ \ in\ wire\ j \times n_j + \frac{\pi d_k^2}{4}\times \%\ vol.\ of\ Ni\ \ in\ wire\ k \times n_k}{\left(\frac{\pi d_i^2}{4}+\frac{\pi d_j^2}{4}+\frac{\pi d_k^2}{4}\right)}\right] \quad \text{Eq. } (i)$$

for percentage of chromium, Eq. *(ii)* is used as given below

$$Cr\ (\%\ wt)\ = \left[\frac{\frac{\pi d_i^2}{4}\times \%\ vol.\ of\ Cr\ in\ wire\ i \times n_i + \frac{\pi d_j^2}{4}\times \%\ vol.\ of\ Cr\ in\ wire\ j \times n_j + \frac{\pi d_k^2}{4}\times \%\ vol.\ of\ Cr\ \ in\ wire\ k \times n_k}{\left(\frac{\pi d_i^2}{4}+\frac{\pi d_j^2}{4}+\frac{\pi d_k^2}{4}\right)}\right] \quad \text{Eq. } (ii)$$

and for percentage of molybdenum, Eq. *(iii)* is used as given below

$$Mo\ (\%\ wt) = \left[\frac{\frac{\pi d_i^2}{4}\times \%\ vol.of\ Mo\ in\ wire\ i \times n_i + \frac{\pi d_j^2}{4}\times \%\ vol.\ of\ Mo\ \ in\ wire\ j \times n_j + \frac{\pi d_k^2}{4}\times \%\ vol.of Mo\ in\ wire\ k \times n_k}{\left(\frac{\pi d_i^2}{4}+\frac{\pi d_j^2}{4}+\frac{\pi d_k^2}{4}\right)}\right] \quad \text{Eq. } (iii)$$

Where,

$d_i =$ diameter of wire i, $d_j =$ diameter of wire j, and $d_k = diameter\ of\ wire\ k$,

i, j *and k* represent the designation of wire1, wire 2 and wire 3 respectively

$n_i =$ number of wires of i grade wire and

$n_j =$ number of wires of j grade wire

$n_k = number\ of\ wires\ of\ k\ grade\ wire$

The compositions of the different layers are calculated by using the above equation. For example, the calculation for determining the composition of the elements in the sixth layer is as follows:

For % of Ni:

$$Ni\ (\%\ wt) = \left[\frac{\frac{\pi 1.2^2}{4}\times 100\times 1+\frac{\pi 1.6^2}{4}\times 57\times 1}{\left(\frac{\pi 1.2^2}{4}+\frac{\pi 1.6^2}{4}\right)}\right] = 72.48\%$$

Similarly, for % of Cr:

$$Cr\ (\%\ wt) = \left[\frac{\frac{\pi 1.2^2}{4}\times 0\times 1+\frac{\pi 1.6^2}{4}\times 21\times 1}{\left(\frac{\pi 1.2^2}{4}+\frac{\pi 1.6^2}{4}\right)}\right] = 13.44\%$$

and for % of Mo:

$$Mo\ (\%\ wt) = \left[\frac{\frac{\pi 1.2^2}{4}\times 0\times 1+\frac{\pi 1.6^2}{4}\times 14\times 1}{\left(\frac{\pi 1.2^2}{4}+\frac{\pi 1.6^2}{4}\right)}\right] = 8.96\%$$

Similarly, the composition of other layers has been calculated which are shown in Table 4.4

Table 4.4: Combination of wire and calculated compositions of each layer

Layer No.	Combination of wire in each layer			Composition ($(\%\ wt)$) (Ni: Cr: Mo)
	Wire1 (no. of wires)	Wire 2 (no. of wires)	Wire 3 (no. of wires)	
1	Ni (1)	-	-	100:00:00
2	Ni (1)	-	-	100:00:00
3	NiCr (1)	Ni (3)	-	95:05:00
4	NiCr (1)	Ni (2)	-	93.3:6.7:00
5	NiCr (1)	Ni (1)	-	90:10:00
6	NiCrMo (1)	Ni (1)	-	72.48:13.44:8.96
7	NiCrMo (3)	Ni (2)	-	68.7:15.3:10.2

8	NiCrMo (2)	Ni (1)	-	66.44:16.4:10.9
9	Inconel 625	NiCrMo (2)	Ni (1)	64.44:17.04:10.8
10	Inconel 625	NiCrMo (2),	NiCr (1)	63.35:20.47:10.28

4.3.2 FGM type-II: FGM by varying Ni, Cr and Mo Elements along the Deposition

Similarly, in FGM Type-II, the composition of each layer was determined by using equations (i), (ii), and (iii). The details regarding the tailored alloy compositions of each layer for the development of the FGM and the combinations of wires utilized to achieve these compositions are outlined in Table 4.5.

Table 4.5: Combination of wire and calculated compositions of each layer

Layer No.	Combination of wire in each layer		Composition ($(\% wt)$)
	Wire1 (no. of wires)	Wire 2 (no. of wires)	(Ni: Cr: Mo)
1	NiCr (1)	Ni (2)	93.33:6.67:00.00
2	NiCr (1)	Ni (1)	90.00:10.00:00.00
3	NiCr (1)	-	80.00:20.00:00.00
4	NiCrMo (1)	NiCr (3)	71.44:20.37:5.21
5	NiCrMo (1)	NiCr (2)	69.18:20.47:6.59
6	NiCrMo (1)	NiCr (1)	65.28:20.64:8.96
7	Inconel 625 (2)	NiCrMo(1)	57.53:21:11.88
8	Inconel 625 (1)	NiCrMo(1)	57.36:21:12.56
9	Inconel 625 (1)	-	58.00:20.00:10.00
10	Inconel 625 (1)	-	58.00:20.00:10.00

4.4 DEVELOPMENT OF FGM

4.4.1 Development of FGM by GTAW WAAM Process without FSP and with FSP

The FGM type-I was fabricated by using optimized GTAW process parameters and conditions along with FSP parameters as presented in Table 4.2 and 4.3, respectively. The deposition of tailored FGM was achieved by combining multiple feed wires wrapped around each other and manually fed to deposit layers. The specific combinations of wires are detailed in Table 4.4.

Two samples were deposited by using two different processing strategies, each consisting of ten layers. One sample was developed in as-deposited condition (Figure 4.9 (a), whereas the second sample was developed with FSP. The initial FSP was carried out after the deposition of four layers, however the optimized no of layer is three for FSP. This is because, during initial bead on plate deposition (first layer), the high degree of dilution is occurred. Thus, the first layer is considering as a reference for further deposition of beads, required for development of FGM. Subsequently, three more layers were deposited, followed by another FSP, and this process was repeated one more time (Figure 4.9 (b)). The thickness of each deposited layer varied from 1.5 to 2.7 mm depending on the number of wires used for the deposition. The overall FGM sample height of as-deposited condition and as deposited with FSP was 21±0.1 mm and 18.5±0.1mm, respectively.

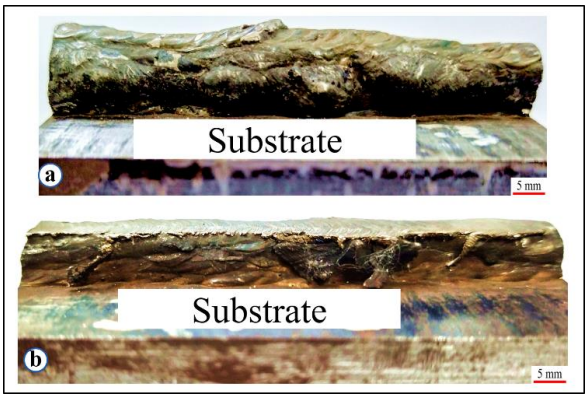

Figure 4.9: Developed FGM type-I sample in two different processing condition (a) as deposited condition and (b) as deposited with FSP condition

4.4.2 Development of FGM by GTAW-WAAM Process with FSP and Different Cooling Environment

The FGM Type-II was developed using an optimized GTAW process and FSP parameters, as presented in Tables 4.2 and 4.3. The deposition of tailored FGM was accomplished by combining multiple feed wires wrapped around each other and manually fed to deposit layers. The specific combinations of wires are detailed in Table 4.5. Three samples were deposited by using different processing strategies, each comprising of ten layers. One sample was developed in the as-deposited condition (Figure 4.10 (a)). In the second sample, after the deposition of four layers, the first FSP was performed in the presence of still air. Subsequently, three more layers were deposited, followed by another FSP, repeated once more. Similarly, a third sample

was also developed, but in this case, instead of FSP with air, FSP with flooded water was used. The FSP with air (FSP) sample exhibited a burnt-like texture (Figure 4.10 (b)) due to excessive heat input, whereas the FSP with water cooling (FSP-W) sample showed a smooth, shiny surface (Figure 4.10(c)). The thickness of each deposited layer varied from 1.5 to 2.7 mm depending on the number of wires used for the deposition. The overall FGM sample height of as-deposited condition and as deposited with FSP was 22±1.1 mm, 18.75±0.9mm, and 19.25±0.75mm respectively.

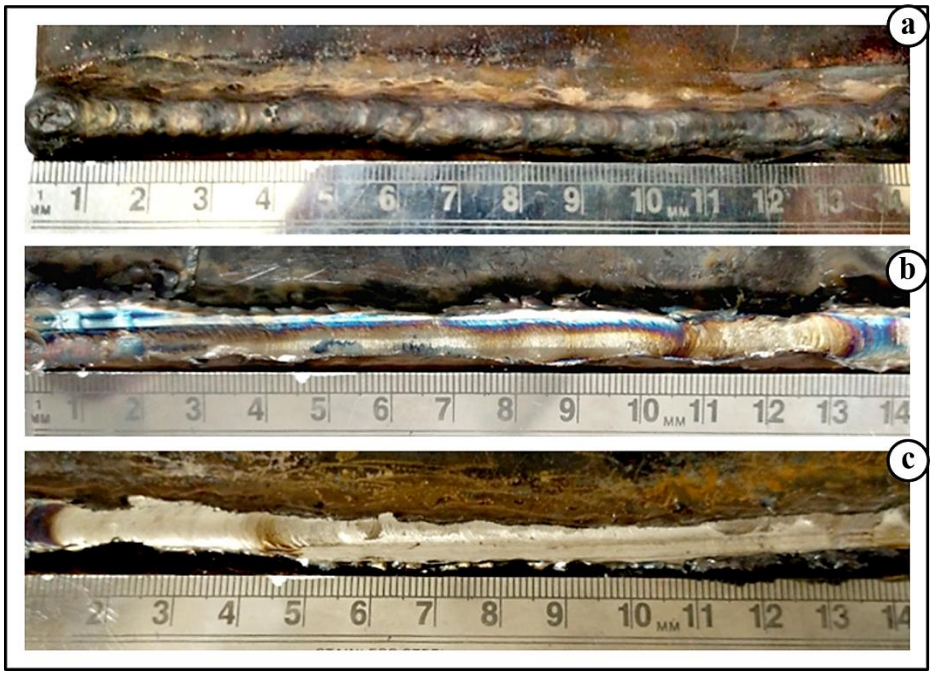

Figure 4.10: Developed FGM type-II sample in two different processing condition (a) as deposited condition, (b) FSP condition and (c) FSP-W condition

SUMMARY

This chapter provides detailed information on GTAW-WAAM and friction stir processing (FSP) setup for manufacturing of FGMs. The different strategies have been followed for FGMs development and they also discussed in details. In these strategies, two types of FGMs were developed, which were based on variation in compositions along the height of the samples. Further, on these developed FGMs, the friction stir processing (FSP) also carried out along with different cooling environment.

Chapter 5

METALLURGICAL AND MECHANICAL CHARACTERIZATION OF DEVELOPED FGMs AT OPTIMIZED PARAMETERS AND CONDITIONS

The detailed discussion on metallurgical and mechanical characterization of the developed FGM is presented in this chapter. This particular type of FGM exhibits variations in the percentages of Ni and Cr, while maintaining Mo at approximately constant levels. Two distinct samples were prepared for analysis: one in its as-deposited state, and the other subjected to additional processing through Friction Stir Processing (FSP).

5.1 METALLURGICAL CHARACTERIZATION OF FGM TYPE- I

After deposition, different specimens were extracted for microstructural and mechanical properties investigation from as-deposited and processed samples at different locations Figure 5.1 (a and b) respectively to examine mechanical and metallurgical behavior. Firstly, the extracted specimens are polished according to standard metallographic procedures, and then electrochemical etching is done by Keller's reagent containing perchloric acid and methanol with an 80:20 ratios. The OM and SEM have been used to check the metallurgical behavior of developed samples. The elemental distributions in the different regions of the specimens have been determined by EDS analysis. The typical XRD spectra has been used to identify the phase constitutions at a 10°/min scan rate.

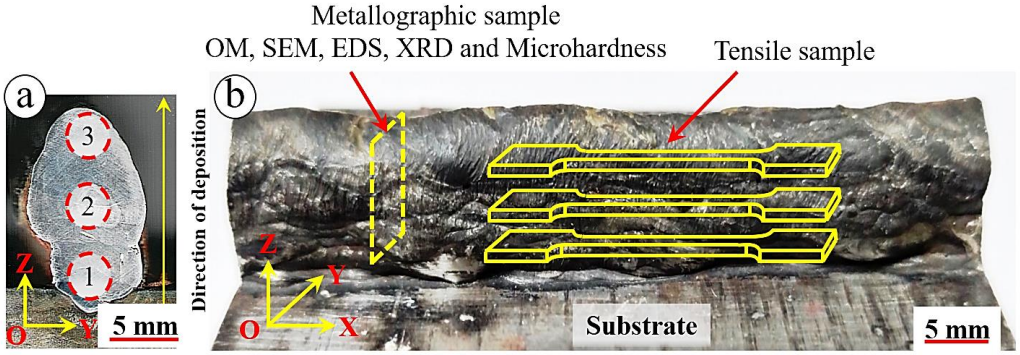

Figure 5.1: (a) Cross-sections of developed FGM showing examination locations, and (b) the sample extraction locations for metallurgical examination and tensile testing

5.1.1 Microstructural Investigation (OM/SEM)

Figure 5.2 (a) shows the micrographs of the as-deposited samples and the locations (1, 2, 3 and 4) where the microstructural examination has been conducted. Figure 5.2 (b) shows the microstructure of location -1 in which different layers and their interfaces are clearly observed in a curved shape pattern. The small equiaxed grain structure appears at this location as marked by a red circle of Figure 5.2 (b). This type of grain structure is observed in location -1 due to fast cooling associated and this region is very close to the substrate and hence, heat transfer is rapid from this location to the substrate region. As moved away from the substrate, columnar and dendritic grains started appearing, whose size initially increased along the deposition height, as clearly visible in locations- 2 & 3 of Figure 5.2 (c) and (d), respectively. The grain size continuously increases up to the deposited material's middle zone. The accumulation of heat in this zone and slow heat transfer are the reasons for such kind of grain growth patterns. Later, from this location, grain size decreased to the top layer due to an increased heat transfer rate [153], clearly visible at location- 4 in Figure 5.2 (e). The variation in the ratios of dendritic and columnar grains is observed at different locations of the deposited bead, which differentiates the effect of the compositional gradient on the developed FGM samples along the deposition direction.

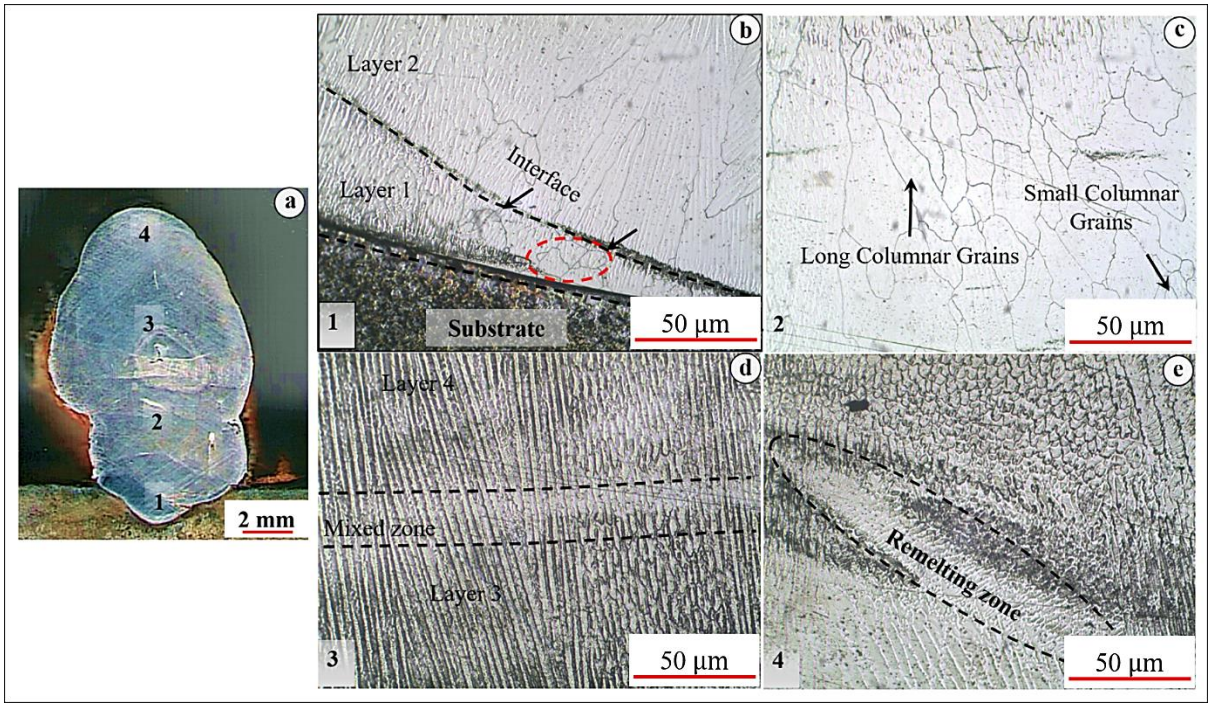

Figure 5.2: Microstructure evolution of as-deposited sample showing (a) cross sectional view, and microstructure at (b) location-1, (c) location-2, (d) location-3, and (e) location-4

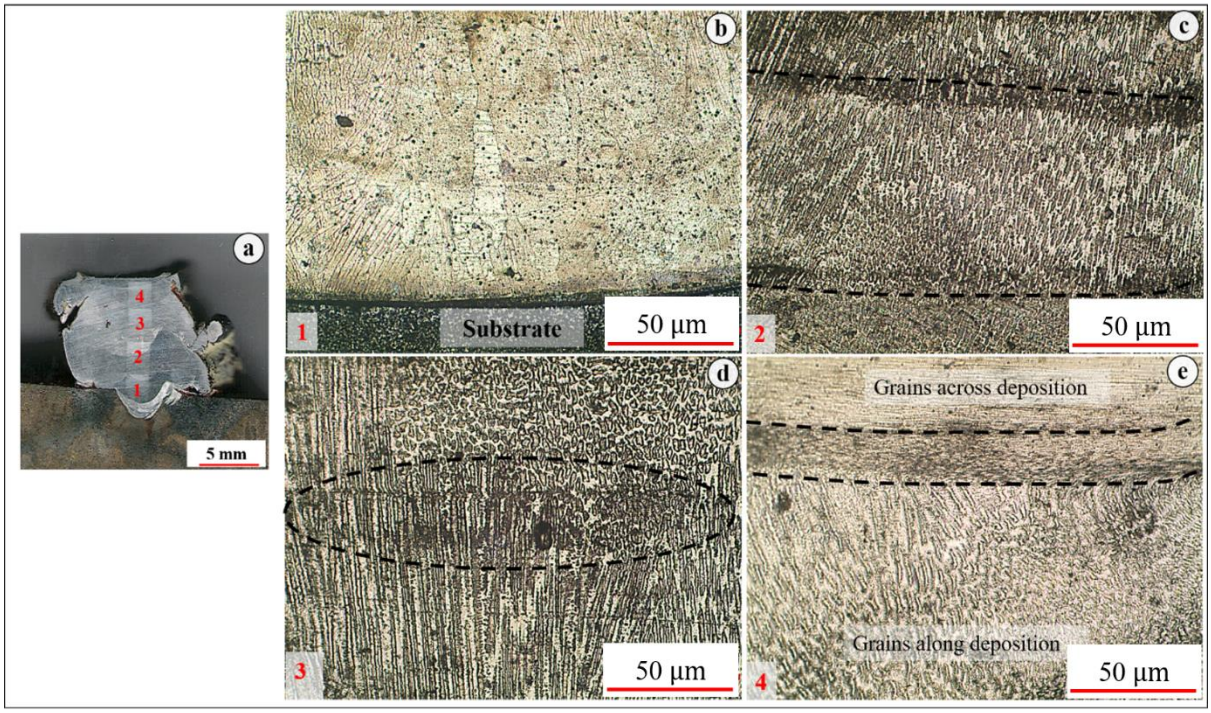

Figure 5.3: Microstructure evolution of FSP sample showing (a) cross sectional view, and microstructure at (b) location-1, (c) location-2, (d) location-3, and (e) location-4

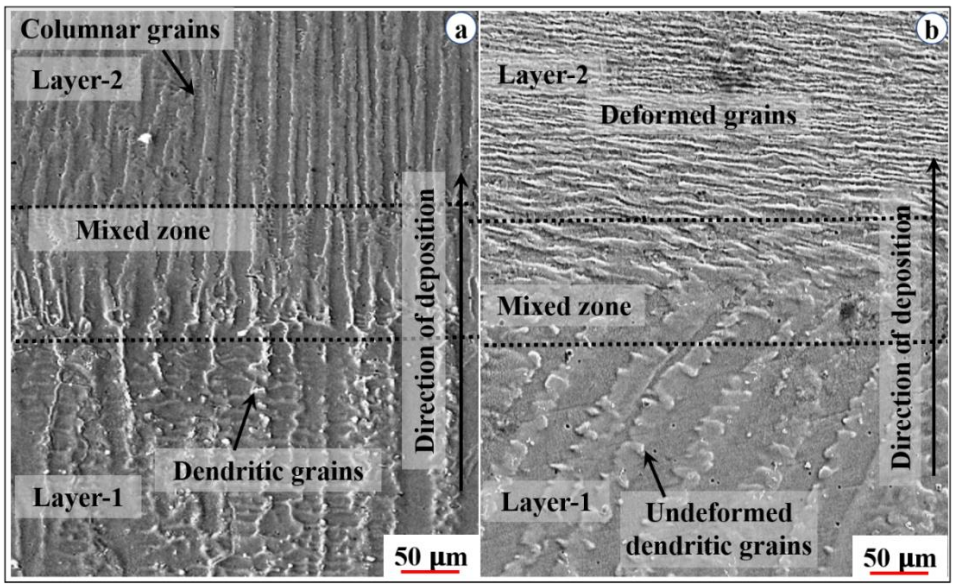

Figure 5.4: SEM micrograph of (a) as-deposited (b) as-deposited with FSP samples

The cross-sectional view of the sample after FSP is as shown in Figure 5.3 (a). The microstructures at different locations (1, 2, 3 and 4) similar to the processed samples, have also been studied in the FSP sample, as shown in Figure 5.3 (b-e). During FSP, due to high frictional heat input, plastic deformation above recrystallization temperature take place[154]. This

deformation causes a change in grain structure and their orientation. This results in a mixture of grains in the FSP sample. The Figure 5.3 (b) shows equiaxed grain in the bottom zone of a developed sample, while in other regions, i.e. locations- 2 and 3, the mixture of grains has appeared, as shown in Figure 5.3 (c) and (d), respectively. The deformed grains along the processing direction observed in the top layer at location- 4 as shown in Figure 5.3 (e).

The field emission scanning electron microscopy (FE-SEM) images of the as deposited sample at the two adjacent layer shows columnar grains oriented towards the deposition direction as shown in Figure 5.4 (a). After FSP, the grain orientation and their deformation changes to the direction of the tool motion (Figure 5.4 (b)).

5.1.2 EDS Analysis

The EDS mapping is conducted to check the concentration gradient of different constituent elements like Ni, Cr and Mo at different locations of the developed FGM from bottom to top. The EDS mapping results show that the concentration of the Ni is maximum in the first three layers (Figure 5.5 (a-f)), then it started decreasing, as clearly shown in Figure 5.6 (a-f). Similar to this, the EDS results also demonstrates the concentration change of Cr in deposited layers. The Cr concentration constantly increasing from bottom to top. Additionally, from the middle section of deposited sample, molybdenum also appears with almost constant concentration, as can see in Figure 5.7 (a-f).

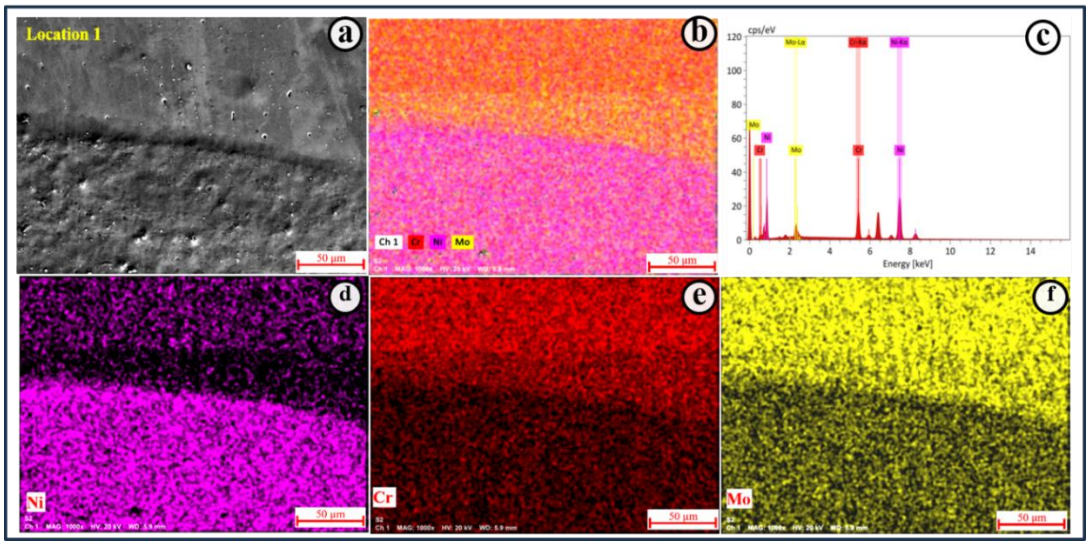

Figure 5.5: EDS analysis at location-1 showing (a) SEM of the deposited sample (b) EDS mapping, (c) EDS spectra, (d) distribution of Ni, (e) distribution of Cr and (f) distribution of Mo

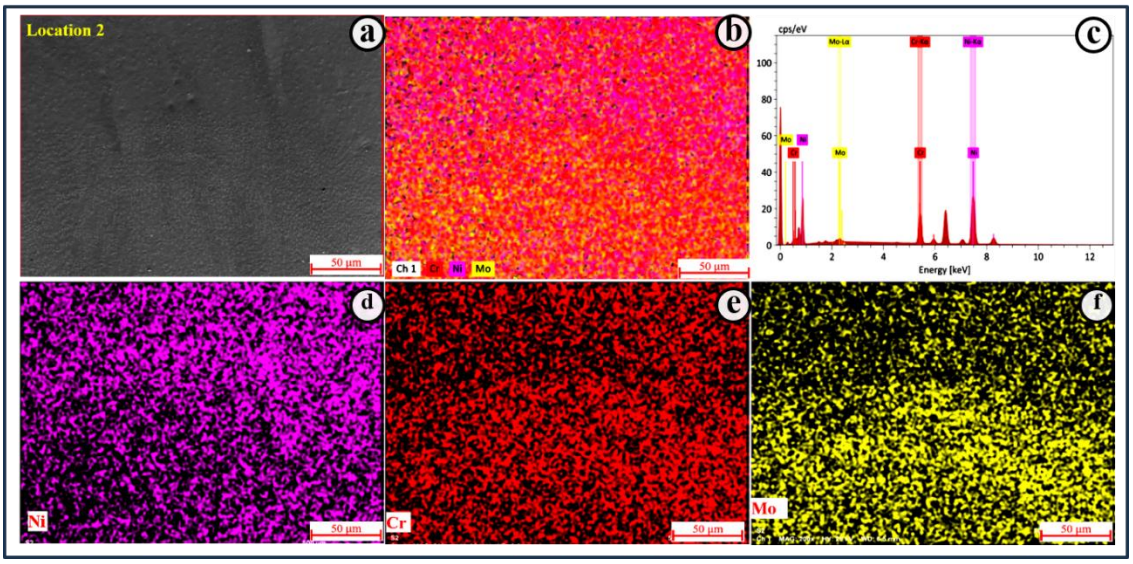

Figure 5.6: EDS analysis at location-2 showing (a) SEM of the deposited sample (b) EDS mapping, (c) EDS spectra, (d) distribution of Ni, (e) distribution of Cr and (f) distribution of Mo

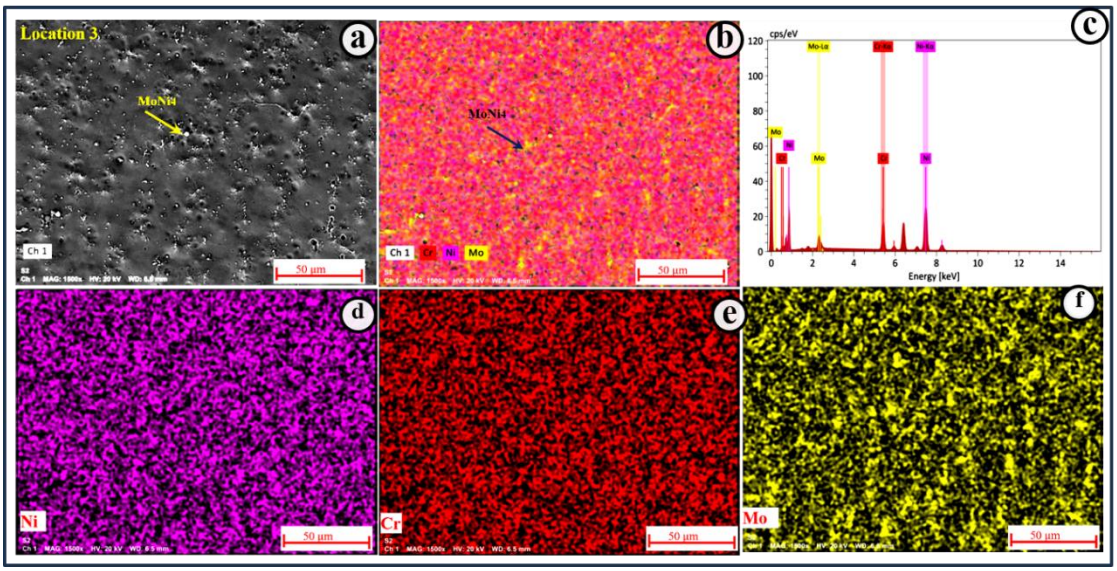

Figure 5.7: EDS analysis at location-3 showing (a) SEM of the deposited sample (b) EDS mapping, (c) EDS spectra, (d) distribution of Ni, (e) distribution of Cr and (f) distribution of Mo

The clear understanding for distribution of elements in both samples (as- deposited and FSP), elemental analysis has been done in three different locations. The Figure 5.8 a & b shows the percentage change in composition of alloying elements at different locations in as-deposited and FSP sample, respectively. The EDS results agree with the designed concentration of the element at the different layers as shown in Table 4.4.

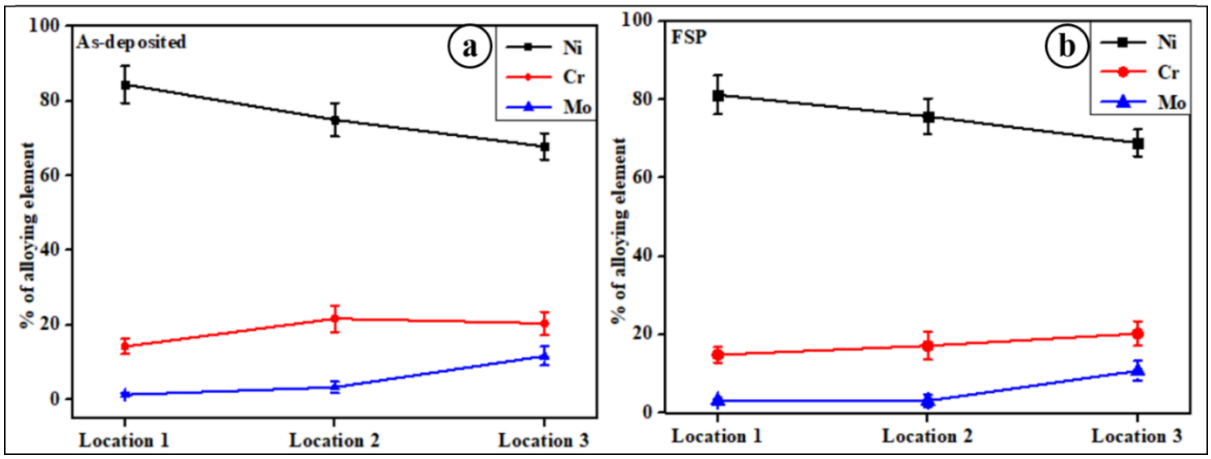

Figure 5. 8: % of alloying elements in (a) as-deposited and (b) FSP sample

5.1.3 EBSD Analysis

The EBSD analysis of the as-deposited and post-FSP samples have been carried out. The specimens are taken from the middle portion of the developed FGM samples. The EBSD analysis shows large columnar grains in the middle region of the as-deposited sample (Figure 5.9 (a)). The grain size of this zone is varying from 257 to 387 µm. This type of grain structure is evident in WAAM samples due to multiple thermal cycles during layer deposition. This phenomenon of large grain formation is eliminated during processing as shown in FSP sample, where the grains are deformed due to severe plastic deformation (Figure 5.9 (b)). As a result, fine grains are produced during processing that is much smaller than the as-deposited samples. The grain size in processed samples ranges from 17 to 35 µm. Thus, FSP is beneficial in reducing the grain size for improving the mechanical properties of produced FGM from WAAM processes.

The inverse pole figure (IPF) of the as-deposited samples, shows that the columnar grains are oriented in the building direction, and this orientation leads to the anisotropic mechanical properties. However, equiaxed grains produced during the post-deposition FSP, may leads to

the uniform properties in all directions. In order to see the aftermath effects of post-processing more accurately, the grain misorientation of as-deposited and post-processed samples are measured. The as-deposited samples show lower grain boundary misorientation (Figure 5.9 (c)), whereas the post-processed sample shows higher angle misorientation, as shown in Figure 5.9 (d). From the grain size distribution and misorientation, it is clear that post-processed samples show equiaxed misoriented small grains as compared to as-deposited samples.

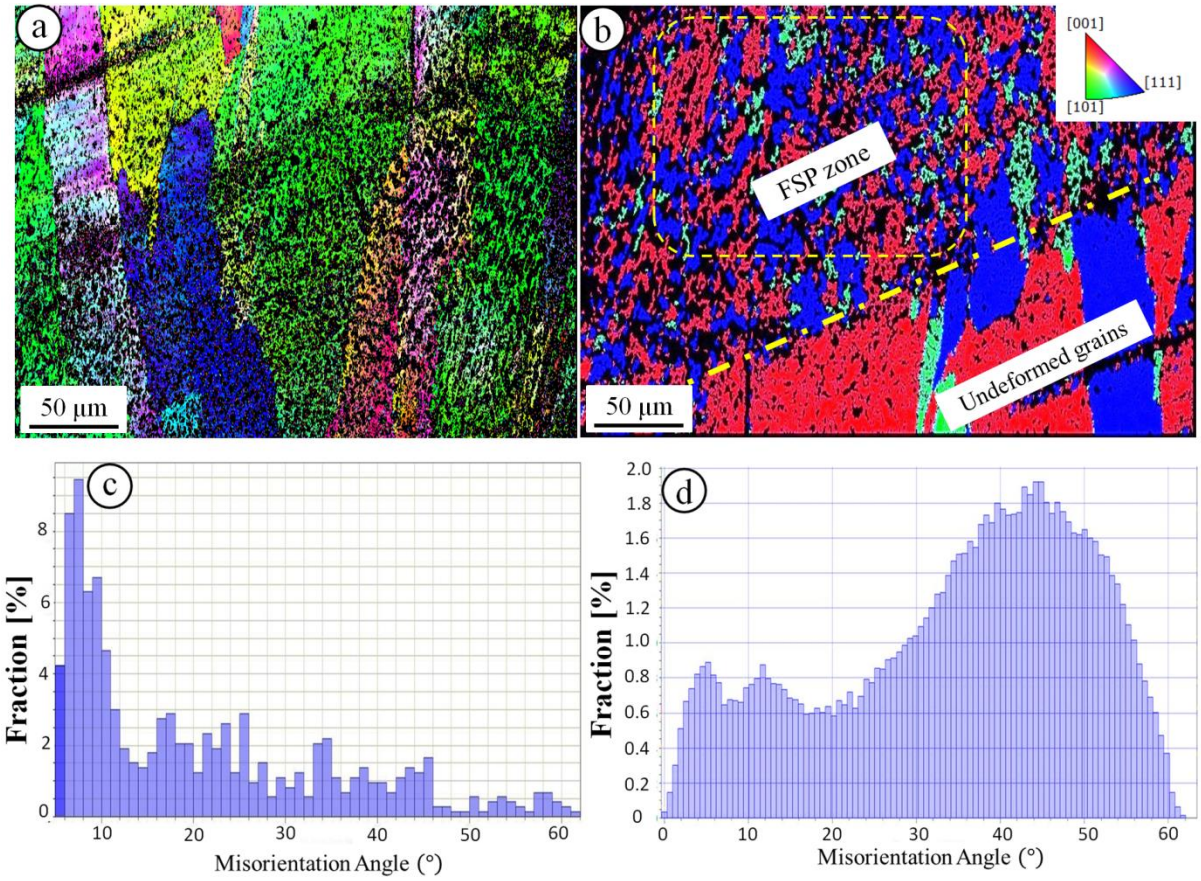

Figure 5.9: EBSD analysis of (a) as-deposited, (b) FSP, misorientation in (c) as-deposited and (d) FSP samples

5.1.4 XRD Analysis

The Figure 5.10 (a) shows the typical XRD spectra of the as-deposited samples, in which γ-Ni and $CrNi_3$ peaks with the crystallographic planes (111), (002), and (022) are observed at 44.13°, 51.41°, and 75.67° diffraction angles, respectively. The intensity of the γ-Ni peak along (002) is more as compared to (111) and (022) planes. The XRD spectra of FSP sample is as shown in Figure 5.10 (b), in which γ-Ni, α-Cr, and $MoNi_4$ peaks with the crystallographic planes (111),

(002), and (022) is observed at 43.88°, 51.12°, and 75.20° diffraction angles respectively. In FSP sample, γ-Ni, α-Cr and $MoNi_4$ peaks are more intensifying as compared to those in as-deposited samples. This is because of FSP provides high-temperature deformation during the processing and promote formation of these precipitates. These intermetallic compounds ($MoNi_4$ and $CrNi_3$) are also noticeable in EDS results, as shown in Figure 5.7(a).

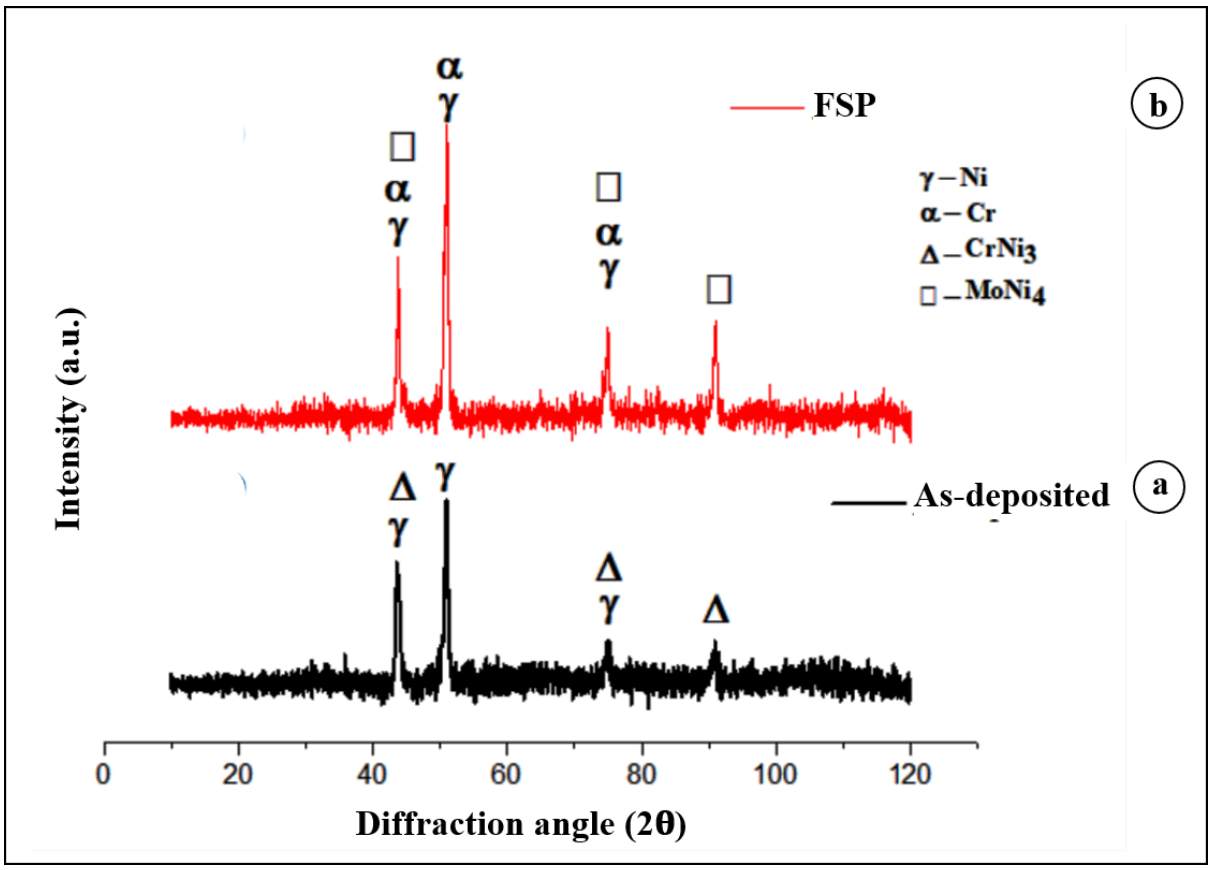

Figure 5.10: The XRD spectra of (a) as-deposited and (b) FSP samples

5.2 MECHANICAL CHARACTERIZATION

5.2.1 Vicker's Microhardness Investigation

The microhardness tests have been performed on as-deposited and FSP samples along the height and width in interval of 0.5 mm, as shown in (yellow dots) of Figure 5.11 (a and b). The unique characteristic of FSP like homogeneity is one of the important considerations and it has been assessed by doing measurement of the microhardness throughout the deposition direction. The microhardness along the deposition direction of as-developed and FSP is shown in Figure 5.12 (a). It is observed that the microhardness gradually increased from bottom to top in both

the samples. The microhardness graph indicates a slight increase in hardness near the substrate for FSP samples, in comparison to that of as-deposited sample. But after fifth layer, a significant change in microhardness is observed which may be because of the presence of molybdenum precipitates ($MoNi_4$), as clearly observed in the XRD result. It happens due the percentage of Ni is almost constant, and the variation in percentage of Mo and Cr is considerably less, up to fifth layer but after fifth layer significant presence of Mo precipitates, change in hardness was observed. Similarly, the average microhardness of different locations is shown in Figure 5.12 (b), which shows very slight increase in microhardness of as-deposited and FSP samples at location-1 and 2 but significant increase is observed at location-3 in both the samples.

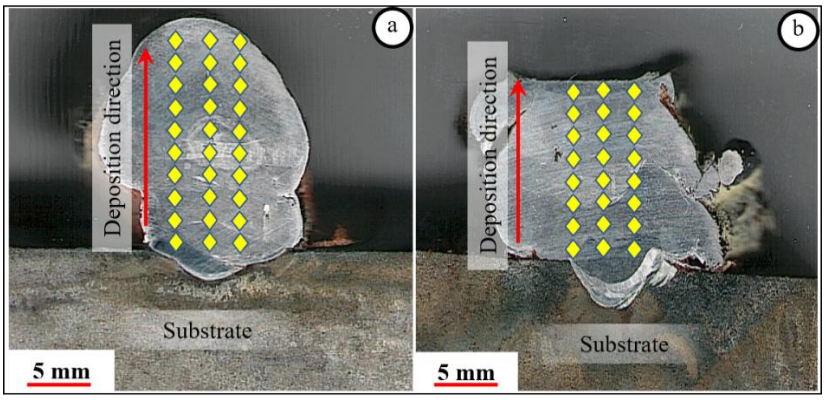

Figure 5.11: Location of microhardness measurement in (a) as deposited and (b) FSP samples

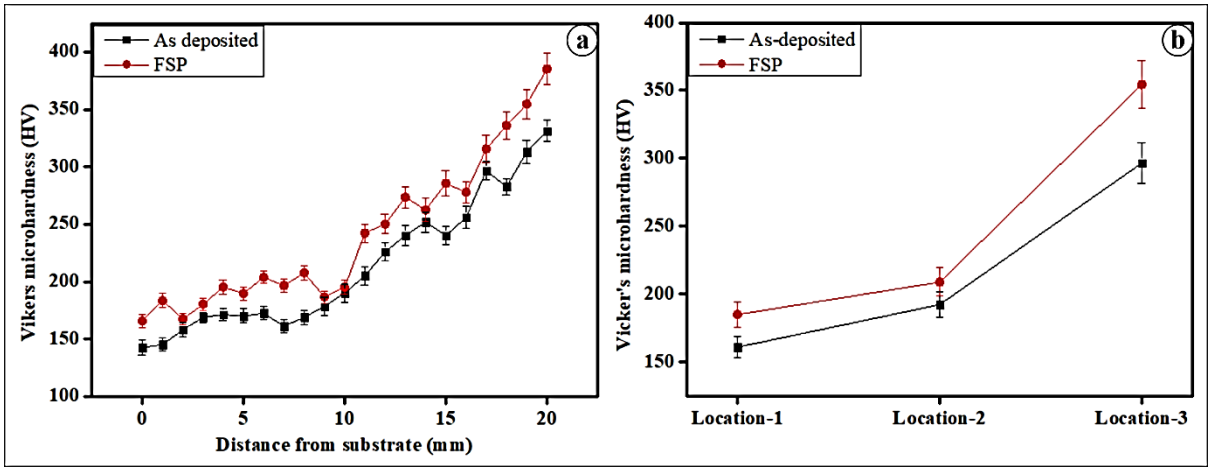

Figure 5.12: (a) Vicker's microhardness profile along the deposition direction, and (b) average microhardness at different locations

5.2.2 Tensile Strength Assessment

The tensile testing has been performed to obtain the mechanical properties of fabricated samples at different locations. The dimension of tensile sample and fabricated sample before and after uniaxial tensile testing are shown in Figure 5.13 a, b & c, respectively. The stress-strain curves of as-deposited and FSP samples are shown in Figure 5.14. The higher UTS and % strain has been observed at location-3 as compared to locations-1 and 2. There is no significant difference in UTS and elongation is observed at location-1 and 2. At both locations-1 and 2, the percentage of Ni is almost constant, and the variation in percentage of Mo and Cr is considerably less, so the tensile properties at locations-1 and 2 remain the same. The FSP samples show uniform UTS at all locations, however, the enhancement in elongation is observed at location-3 as compared to location-1 and 2 as shown in Figure 5.14 d, e & f.

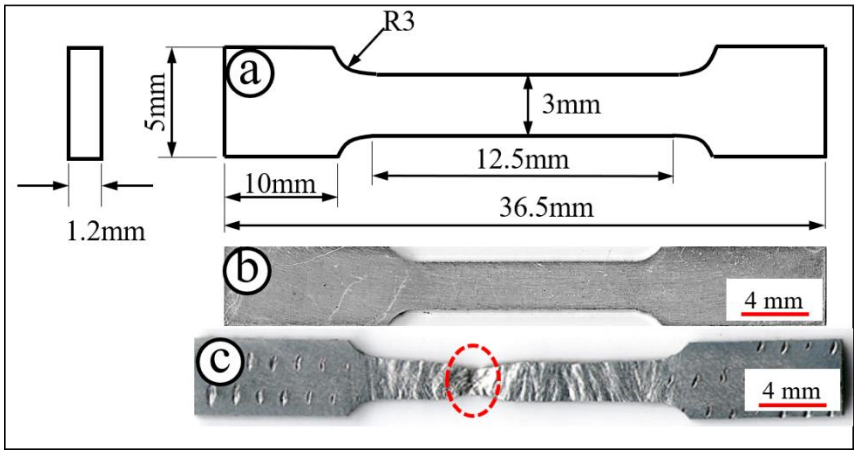

Figure 5.13: (a) Dimension of tensile sample and (b) fabricated tensile sample before testing and (c) fabricated tensile sample after testing

For more understanding about the mechanical behaviour of the developed sample, a comparison of mechanical properties of fabricated FGM with pure IN625 WAAM deposited samples has been done and presented in Table 5.1. The tensile strength of fabricated FGM samples is higher than that of deposited pure IN625 and it is comparable with published data as shown in Table 5.1.

Table 5.1: Comparison of mechanical properties of fabricated sample with published research articles data

Mechanical properties	Deposited IN625 [26]	Developed FGM
Tensile strength (MPA)	739	715-877
% elongation	37	31-42
Hardness (HV)	197	147-335

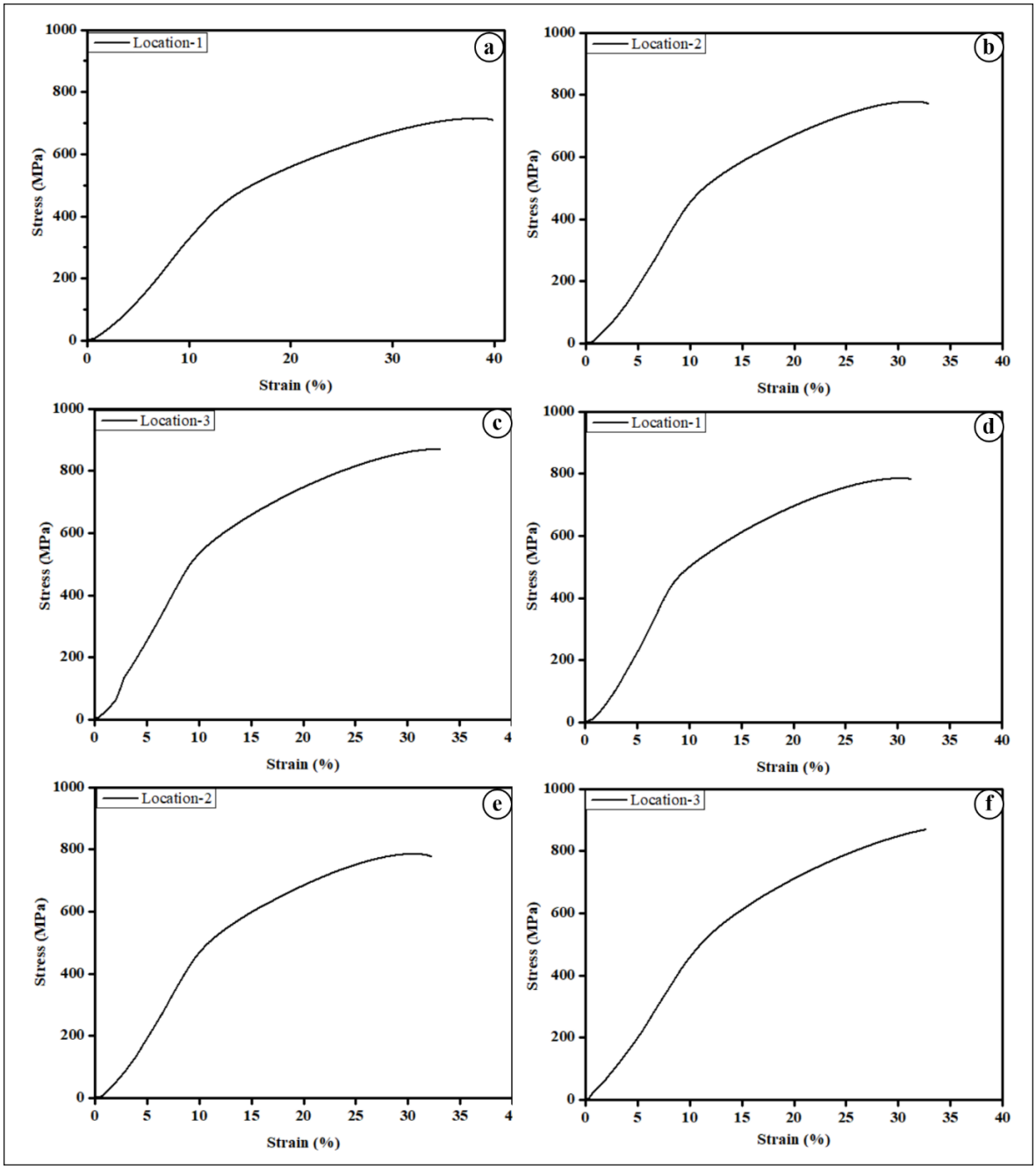

Figure 5.14: Stress-strain curves of as-deposited sample at (a) location-1, (b) location-2 and (c) location-3 and FSP sample at (d) location-1, (e) location-2, and (c) location-3

5.3 METALLURGICAL CHARACTERIZATION OF FGM TYPE-II

The FGM Type-II samples were developed in different processing conditions and specimens were extracted at different locations to examine mechanical and metallurgical examination. The location of sample extraction is shown in Figure 5.15 (a and b). Firstly, the extracted samples were polished according to standard metallographic procedures, and then electrochemical etching was done by Keller's reagent containing perchloric acid and methanol with an 80:20 ratio. The tensile specimens have also been extracted from different locations of developed samples, as shown in Figure 5.15 (a).

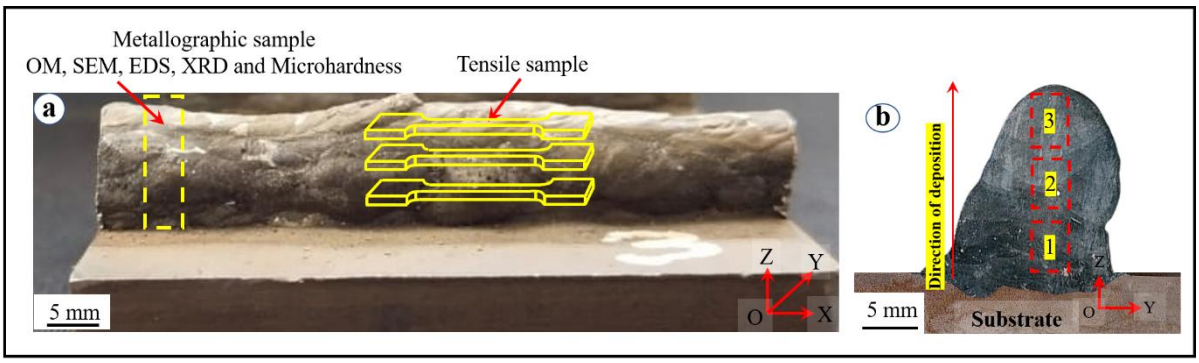

Figure 5.15: (a) The sample extraction locations for microstructural examination and tensile testing, and (b) cross-sections of developed FGM showing examination locations

5.3.1 Microstructural Investigation (OM and Grain Size)

The WAAM deposited FGM sample has been subjected to macro and microscopic examination. The Figure 5.16 (a, b and c) shows the microstructure of as-deposited, FSP and FSP-W samples, respectively at three different locations (1, 2 and 3). As-deposited walls exhibit dendrites and columnar grains as a result of varying solidification patterns within the layers [155]. In this sample near to substrate, a course columnar grains are first observed, and then their size gradually decreases at location-2 and as they approach to top layer, the grain sizes increase again at location-3 and along with this dendritic structure has been observed, as shown in Figure 5.16 (a-1, 2 and 3). However, in the FSP, little large columnar and equiaxed grains appeared due to recrystallization caused by high temperature frictional deformation in air-cooled environment, as shown in Figure 5.16 (b- 1,2 and 3). The small columnar and equiaxed grains have been observed in FSP-W sample due to recrystallization and quenching

effect during frictional deformation in the water-cooled environment, as shown in Figure 5.16 (c-1,2 and 3).

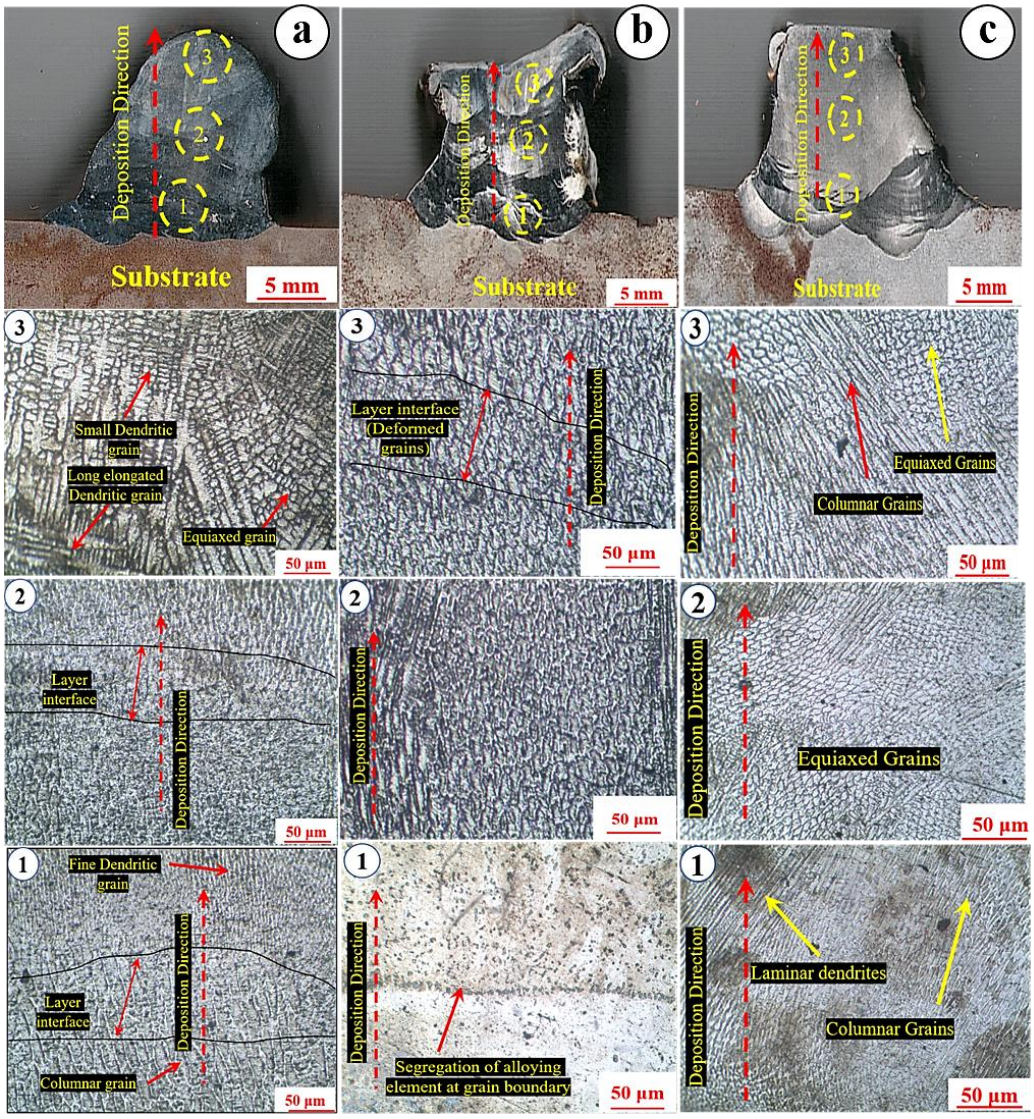

Figure 5.16: Macro and microstructure evolution of (a) As-deposited, (b) FSP and (c) FSP-W

The Figure 5.17 (a) shows the average grain size distribution along the deposition height in all samples. It is observed that the size of grains along the deposition height in the as-deposited sample initially decreases and then slightly increases while FSP and FSP-W show continuous increase in grain size. This variation in grain size occurred due to variation of cooling rate which decreases as the distance from substrate increases. The grain size is also depending on the post deposition processing and it is observed that in FSP condition, grain size is higher in location-1 and 2, however it is lower in location-3 than as deposited and FSP-W samples.

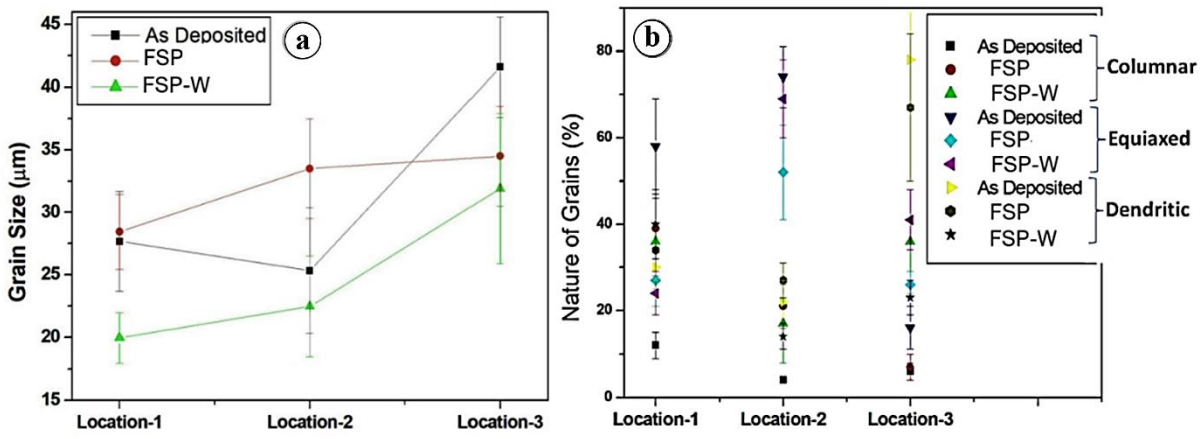

Figure 5.17: (a) Average grain size distribution and (b) nature of grains (%)

It is also observed that the grain structure is different at different spots of deposited material. This variation in grain structure occurred due to different cooling rate. This cooling rate causes formation of mixture of grain structure during deposition. So far to obtain a proper understanding about the nature of grain structure at different spots, percentage of different grain structures have been measured along the deposition height for all samples. This percentage has been calculated with the help of multiple micrographs taken from optical microscopy at three different locations (i.e. Location-1, Location-2 and Location-3) and their average grain size is presented in Figure 5.17 (b). It is observed that columnar grains are increases from bottom to top in all samples due to larger heat accumulation and lower cooling rate. However, large variation in grain size was observed in as-deposited sample. In FSP sample, minimum variation with large grain size was observed. The FSP-W sample showed smaller grain size at every location as compared to as-deposited and FSP samples.

5.3.2 SEM Analysis

The microstructural evolution of the deposited FGM with different processing conditions is shown in Figure 5.18. The Figure 5.18 (a) shows the microstructure of the as-deposited sample. The SEM image, shows a clear distinct boundary between two patterns of grain structures. The bottom region shows large columnar grains, formed due to one-direction heat transfer in the deposited sample. However, the top zone shows similar type of grain structure but lower in size. This difference in grain structure is occurred during multilayer deposition of material where next layer deposited on the previously deposited layer. This causes, the bottom zone of newly deposited layer cools faster and shows smaller columnar grains. A small region of the

remelted zone is also observed In between these two grains where defused like of grain structure is observed.

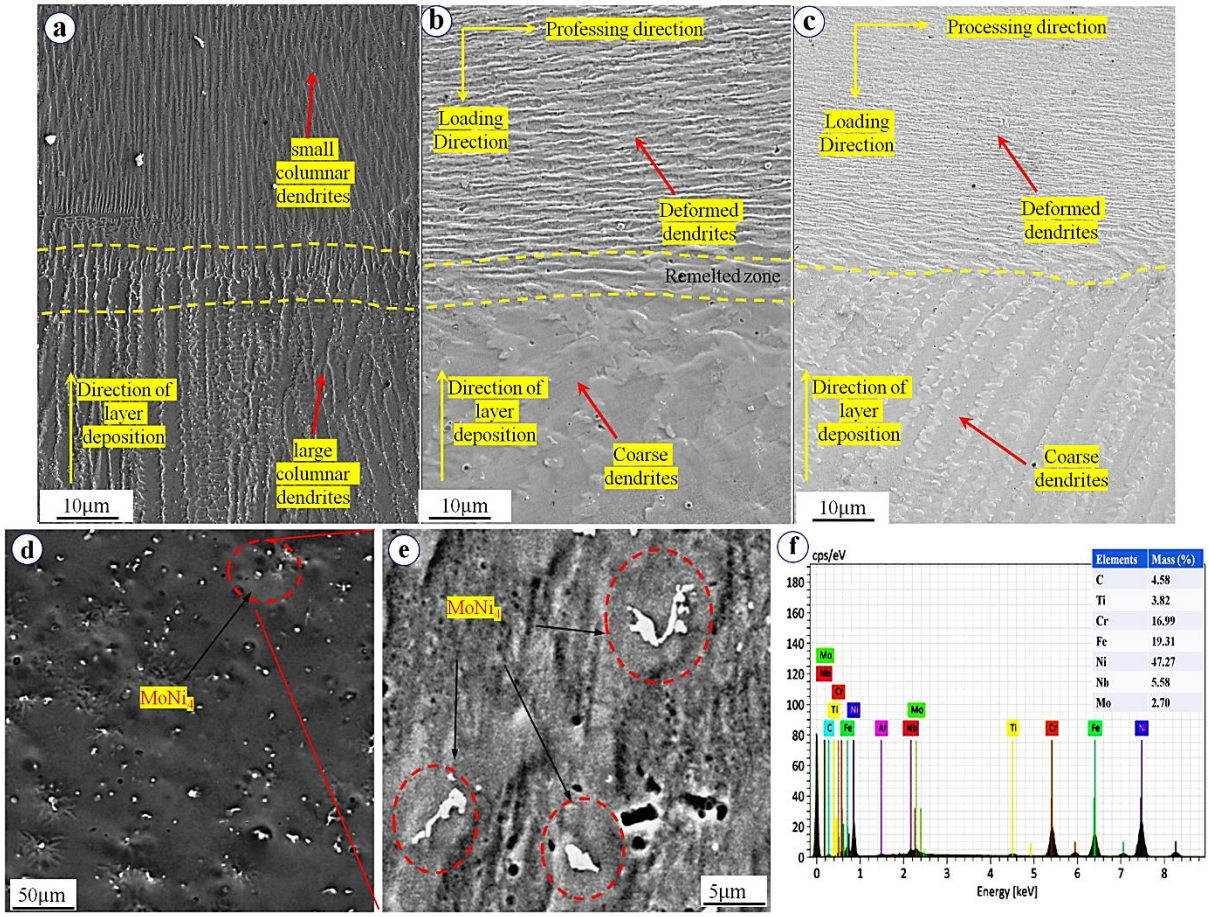

Figure 5.18: Microstructure of (a) as deposited, (b) FSP, (c) FSP-W samples (d) precipitates distribution in deposited material (e) precipitates at higher magnification and (f) elemental mapping

In the case of WAAM with FSP, new grains formation occurred with orientation along the processing direction as shown in Figure 5.18 (b). The change in the orientation of the new grains was observed due to plastic deformation and recrystallization of the material during FSP[137]. The grain size of newly formed dendrites is smaller in the case of water-cooling samples over FSP due to faster cooling associated (Figure 5.18 (c)).

The Figure 5.18(d) shows the irregular precipitate distributed in the deposited sample. The higher magnification images of these precipitates are presented in Figure 5.18 (e). The elemental mapping of these precipitates by EDS analysis (Figure 5.18 (f)) shows A_2B type

Laves phase. This indicates that principal elements such as Cr, Mo, and Ti are abundant in Laves phase. Laves particles have been identified as Ni + Mo and Ni + Ti, which aligns with the A_mB_n (A: Ni, Cr and B: Mo, Ti) such as Ni_4Mo form of Laves phase [156].

5.3.3 EDS Analysis

In order to obtain a clear indication of compositional gradient and deformation behaviour in the fabricated wall, the composition analysis has been carried out in all conditions. The Figure 5.19 (a) shows as-deposited sample along which EDS mapping from the substrate to the top layer. The Figure 5.19 (b) shows a low magnification SEM image of sample used for EDS mapping. The Figure 5.19 (c) shows variations in the concentration of different alloying elements in the deposited sample along the deposition height. It is clear from this image that the variation of elements is there in different layers. This elemental variation is obvious because of variation in the concentration of alloying elements during deposition. The EDS analysis also shows that micro-segregation of alloying elements is not present in the deposited sample. However, the concentration gradient of different elements is present during different layers of the deposited sample. The concentration of each element is also mapped with EDS analysis. The Figure 5.19 (d) shows, that the concentration gradient of Ni which is decreasing along the height, along with that, Ni-rich bands also appeared in EDS mapping, which may be due to dilution and macro segregation in between layers due to remelting of the deposited layer. But other alloying elements like, chromium and molybdenum gradually increase along the height of the fabricated sample, which is as shown in Figure 5.19 (e) and Figure 5.19 (f), respectively. The segregation of these elements is not visible much by EDS analysis.

The Figure 5.20 (a) shows, the different bands of deposited layers in FSP sample. In this sample due to friction and pressure, deformation occurred of the deposited material. The deformation regions are properly visualized and represented by the red dotted line. The EDS mapping has been done along the height of the deposited sample (Figure 5.20 (b)) to identify the effect of high temperature and pressure deformation on the distribution of alloying elements. The Figure 5.20 (c) shows, the EDS mapping of different alloying elements like Ni, Cr and Mo along the height. The nickel percentage towards deposition direction decreases, but the variation is more uniform due to reheating, while high-temperature deformation as compared to as-deposited sample as shown in Figure 5.20 (d). A similar pattern is correspondingly observed in the case of distribution of Cr and Mo elements as shown in Figure 5.20 (e and f), respectively.

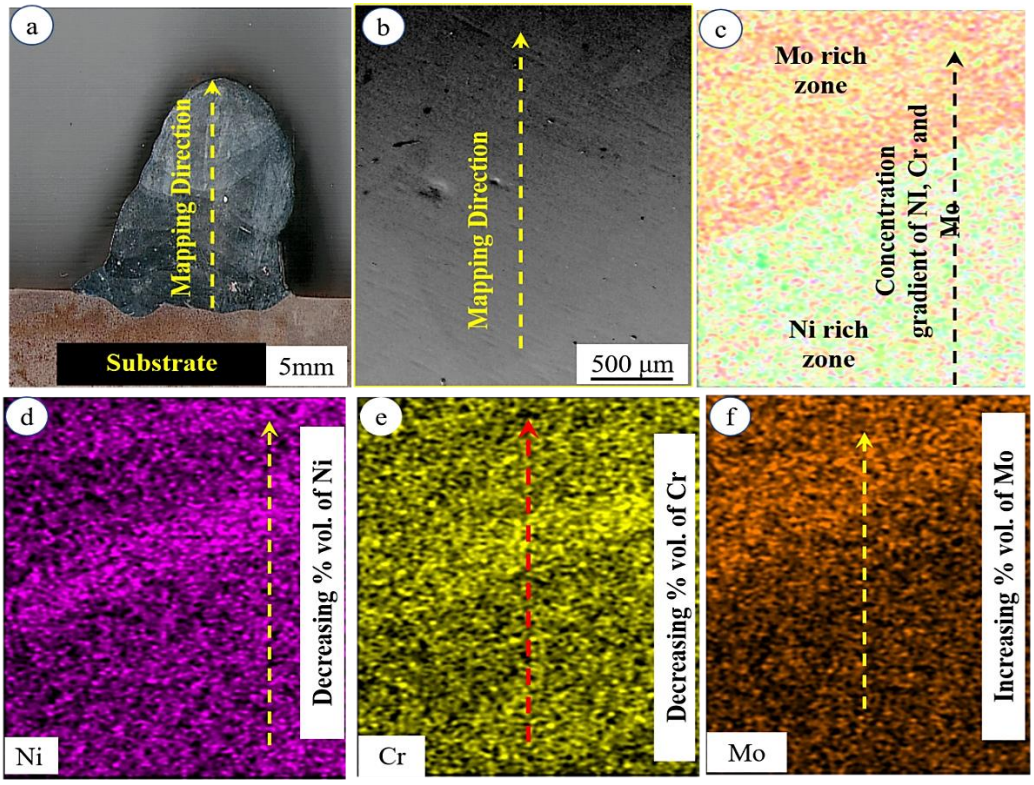

Figure 5.19: (a) Macrostructure of the deposited sample, (b) SEM of the deposited sample (c) EDS mapping, (d) variation of Ni, (e) variation of Cr and (f) variation of Mo

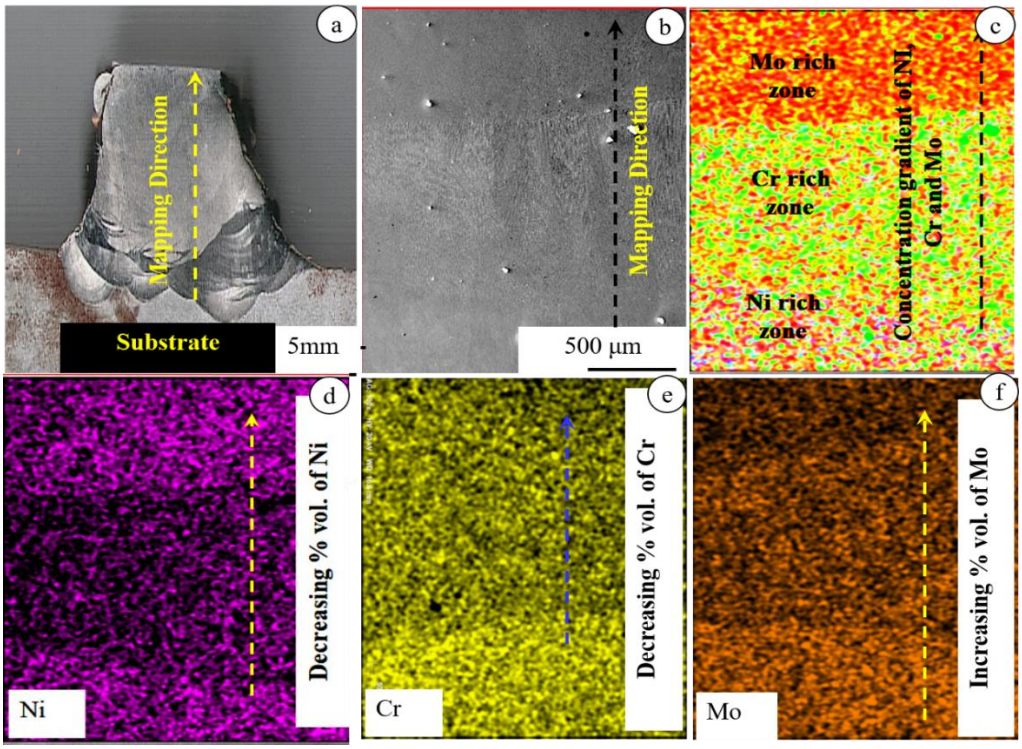

Figure 5.20: (a) Macrostructure of FSP sample, (b) SEM of FSP sample, (c) EDS mapping, (d)

variation of Ni, (e) variation of Cr and (f) variation of Mo

The Figure 5.21 (a) shows the deposited sample at high temperature and high-pressure deformation with water cooling conditions. The EDS mapping (Figure 5.21 (b)) reveals the distribution of the constituent alloying elements (Ni, Cr and Mo) along the deposition height is as shown in Figure 5.21 (c). The nickel percentage along the deposition height decreases similarly to other samples. Nevertheless, the variation is more uniform as compared to as-deposited and FSP samples as shown in Figure 5.21 (d), is also true with other alloying elements like Cr and Mo, as shown in Figure 5.21 (e and f).

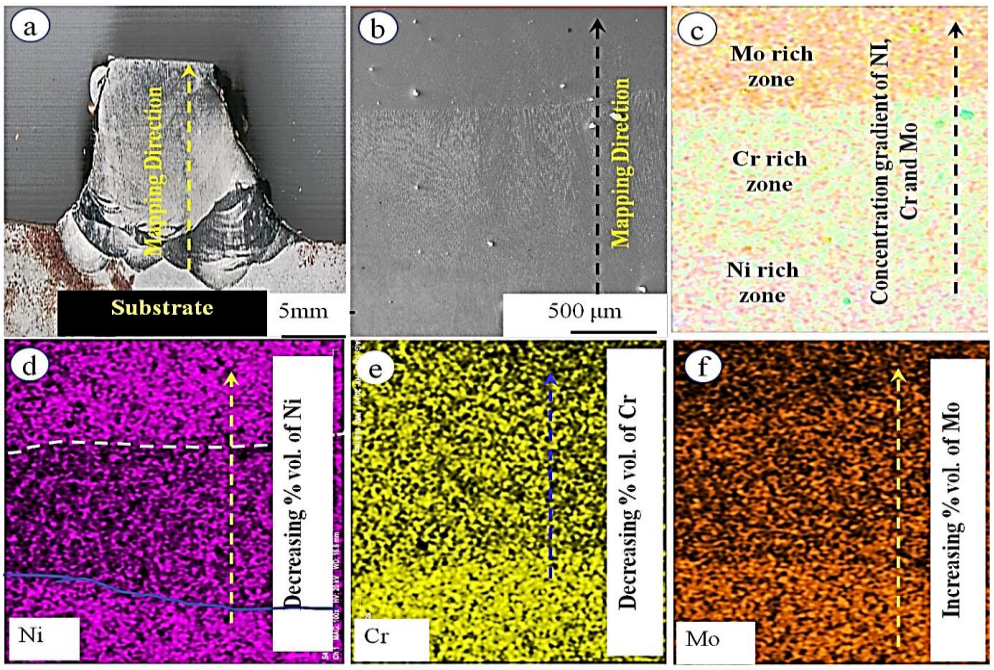

Figure 5.21: (a) Macrostructure of FSP-W sample, (b) SEM of FSP-W sample, (c) EDS mapping, (d) variation of Ni, (e) variation of Cr and (f) variation of Mo

5.3.4 XRD Analysis

The X-ray diffraction (XRD) analysis has been performed for phase analysis in all deposited samples. The XRD analysis for as-deposited, FSP and FSP-W samples is shown in Figure 5.22 a, b and c respectively. The XRD peaks in the case of as-deposited sample appears due to the presence of $MoNi_4$, $Ni_{3.28}Ti_{0.72}$ and Ni in (111), (022) and (002) crystal plane, but the intensity of peak along (002) is more as compared to (111) and (022) (Figure 5.22 (a)). In the case of FSP, peaks appeared due to the presence of $Mo_{0.4}Ni_{3.6}$, Cr_1Ni_3 and $Ni_{3.28}Ti_{0.72}$ in (111), (022) and (002) crystal planes (Figure 5.22 (b)). The maximum intensity peak is present in the (002)

plane, but this peak is much larger than as-deposited sample, which might be due to high deformation at elevated temperatures. In the case of the FSP-W sample the peaks appeared due to existence of $Cr_{0.4}Ni_{0.6}$, $Ni_{0.906}Ti_{0.094}$ in (111), (022) and (002) crystal planes (Figure 5.22 (c)). In this case, maximum peak intensity appeared at the (111) crystal plane, and it is more significant than as-deposited and FSP samples, while a relatively lower peak appears at the (002) and (022) crystal plane.

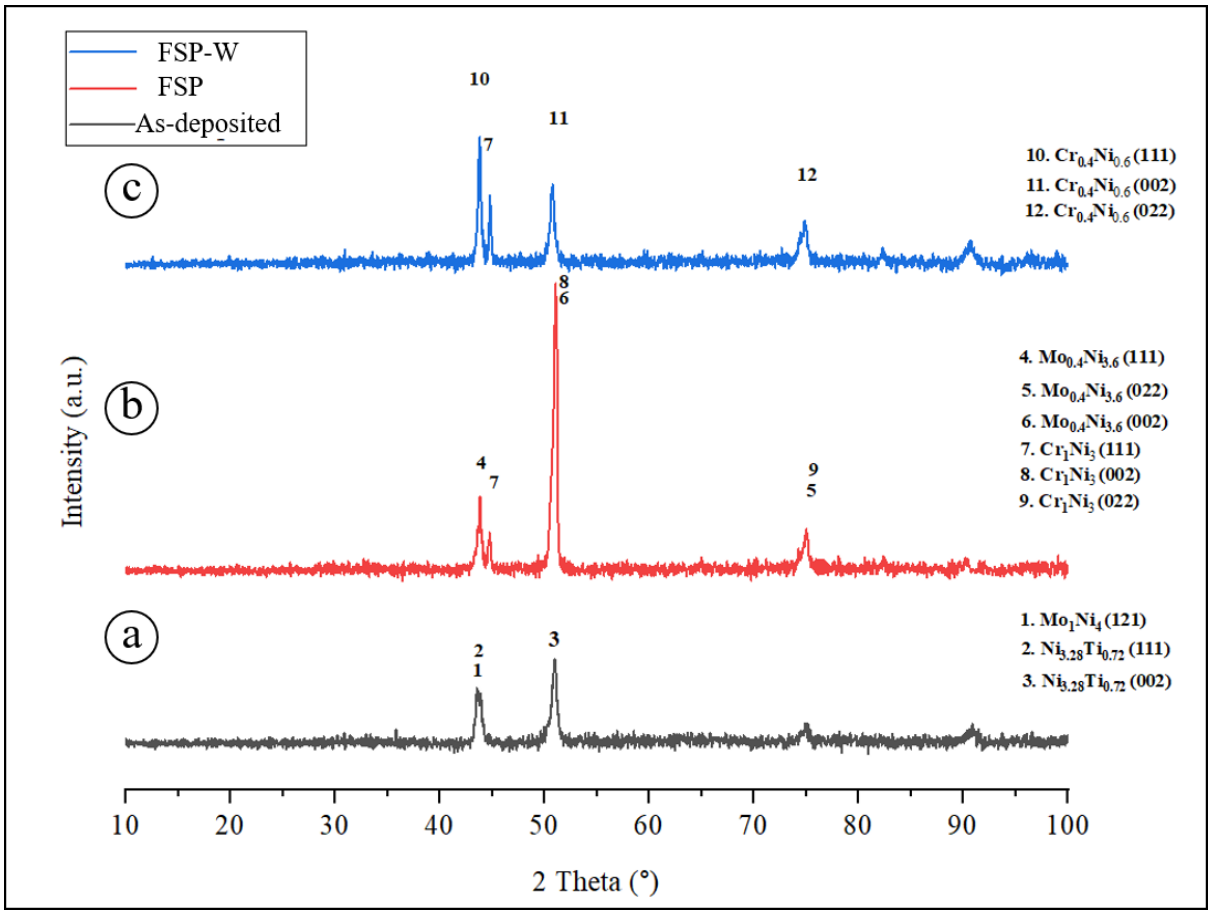

Figure 5.22: The XRD spectra of (a) as-deposited, (b) FSP and (c) FSP-W

5.4 MECHANICAL CHARACTERIZATION OF FGM TYPE-II

5.4.1 Vicker's Microhardness Investigation

The Vicker's microhardness distribution of the deposited samples along the deposition direction from the substrate to the top layer of the sample has been measure and presented in Figure 5.23 (a, b and c). The microhardness profiles of the deposited sample shows, that the microhardness increases from the substrate to the top in all samples. The increase in hardness in as-deposited sample (Figure 5.23 (a)), occurred due to decrease in concentration of Ni and

increased concentration of Cr and Mo. The FSP sample exhibits similar hardness trends (Figure 5.23 (b)), but its hardness slightly higher than as-deposited sample. This is the result of frictional deformation and recrystallization of deposited material. However, the FSP-W sample exhibits highest hardness (Figure 5.23 (c)) amongst all samples across the deposition height. This increase in hardness is because of frictional deformation in presence of water cooling causes a quenching effect in the deformation zone, which causes higher grain refinement as observed from microstructural analysis and hence higher hardness has been achieved as compared to other processing condition.

To observe actual variation in the hardness, average hardness at different locations of sample was also been measured. The Figure 5.24 shows the average hardness at three different locations of deposited sample. Figure 5.24 (a) shows, the average hardness al location-1 in all samples. The hardness of as-deposited and FSP shows almost similar hardness trend. However, FSP-W samples shows higher hardness. At location-2, the hardness is little higher in FSP sample as compared to as-deposited sample and highest hardness is observed in FSP-W sample (Figure 5.24 (b)). A similar hardness trend is also observed at location 3 (Figure 5.24 (c)).

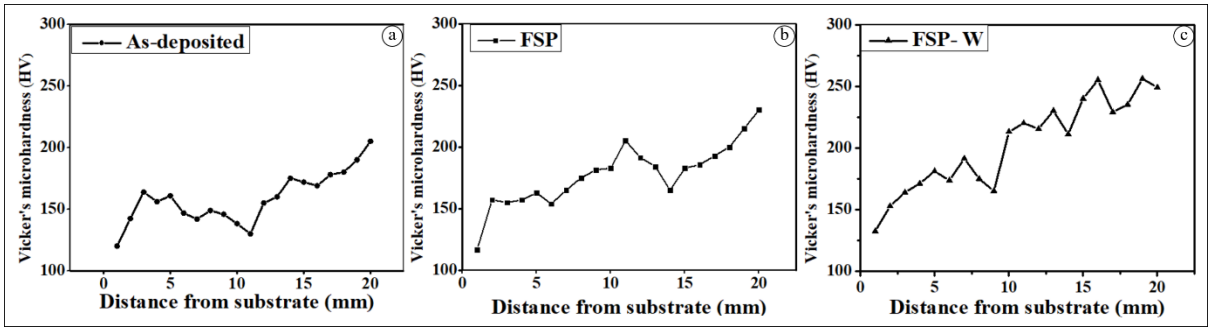

Figure 5.23: Microhardness distribution along the deposition direction from the substrate to the top layer, (a) as deposited, (b) FSP, (c) FSP-W

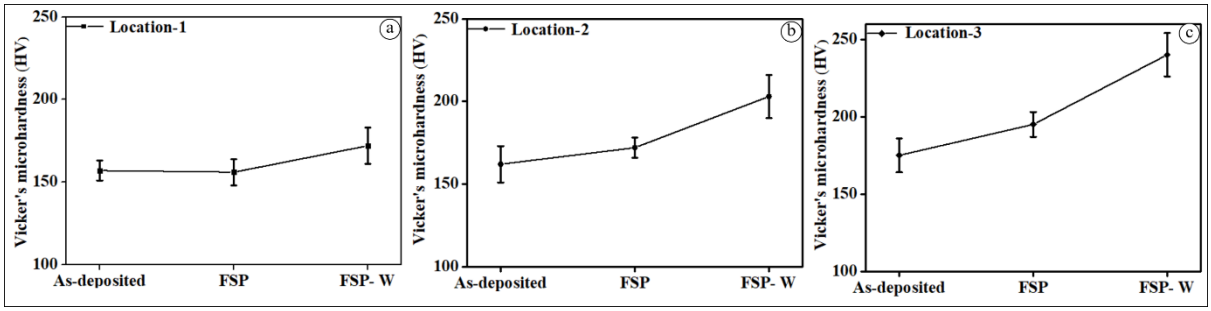

Figure 5.24: Average microhardness at (a) location-1, (b) location-2 and (c) location-3

5.4.2 Tensile Strength Assessment

The Figure 5.25 (a, b and c) shows the stress-strain diagram for as-deposited, FSP and FSP-W samples, respectively. These images clearly show that the stress–strain behaviour varies at different locations of the deposited samples. It is due to the compositional variation of the alloying elements and the post-deposition processing conditions. Figure 5.25 (a) shows that the UTS and percentage elongation increase along the deposition height (i.e., from location 1 to location 3) in the case of the as-deposited sample. Similar trend is also observed in the FSP sample but location 3 exhibits higher percentage elongation than other locations, as shown in Figure 5.25 (b). Figure 5.25 (c) shows that at location 3, the highest UTS is observed in all samples compared to other locations. This is because of presence of alloying elements and frictional deformation along with water cooling promotes grain refinement, which increase the strength of the deposited material.

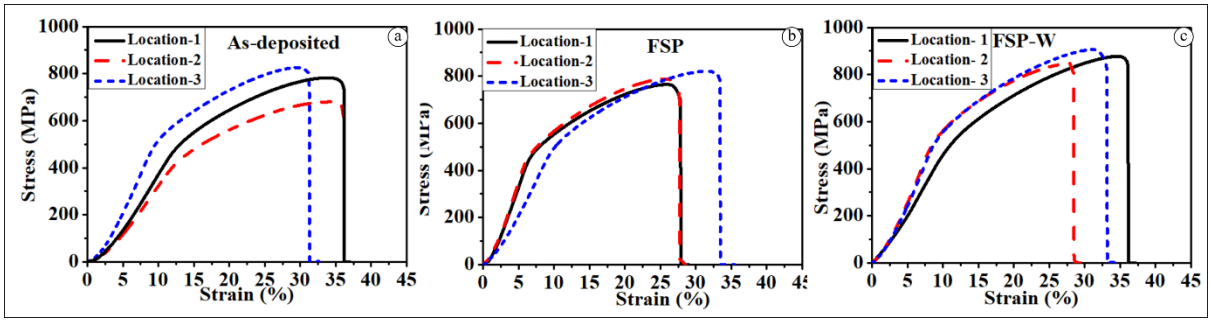

Figure 5.25: Stress-Strain diagram along the deposition direction from substrate to the top layer (a) as deposited, (b) FSP, and (c) FSP-W

The fracture surfaces of the developed samples were investigated using Scanning Electron Microscopy (SEM). At low magnifications, the SEM micrographs reveal the entire fracture surfaces of tensile samples in their as-deposited state (Figure 5.26 (a)), following FSP (Figure 5.26 (b)), and after FSP-W (Figure 5.26 (c)). These samples exhibit a cone-shaped deformation prior to the final fracture, indicating significant deformation before final failure of tensile specimen. This observation is further correlated with tensile test results, which demonstrate a considerable elongation (greater than 30%) before fracture. Figure 5.26 (d-f) present a higher magnification view of the fracture surfaces for as-deposited, FSP, and FSP-W conditions, respectively. At these magnifications, the presence of dimples of various sizes on the fracture surfaces confirms the ductile nature of the failure. These dimples typically form when cracks are initiated at specific locations within the sample and propagate under tensile stress. It has been noted that secondary precipitates sometimes serve as nucleation sites for cracks due to

their brittleness, thereby initiating the failure process in the material. This analysis not only highlights the critical role of processing conditions in determining the mechanical behavior of materials but also underscores the importance of microscopic examination in understanding failure mechanisms.

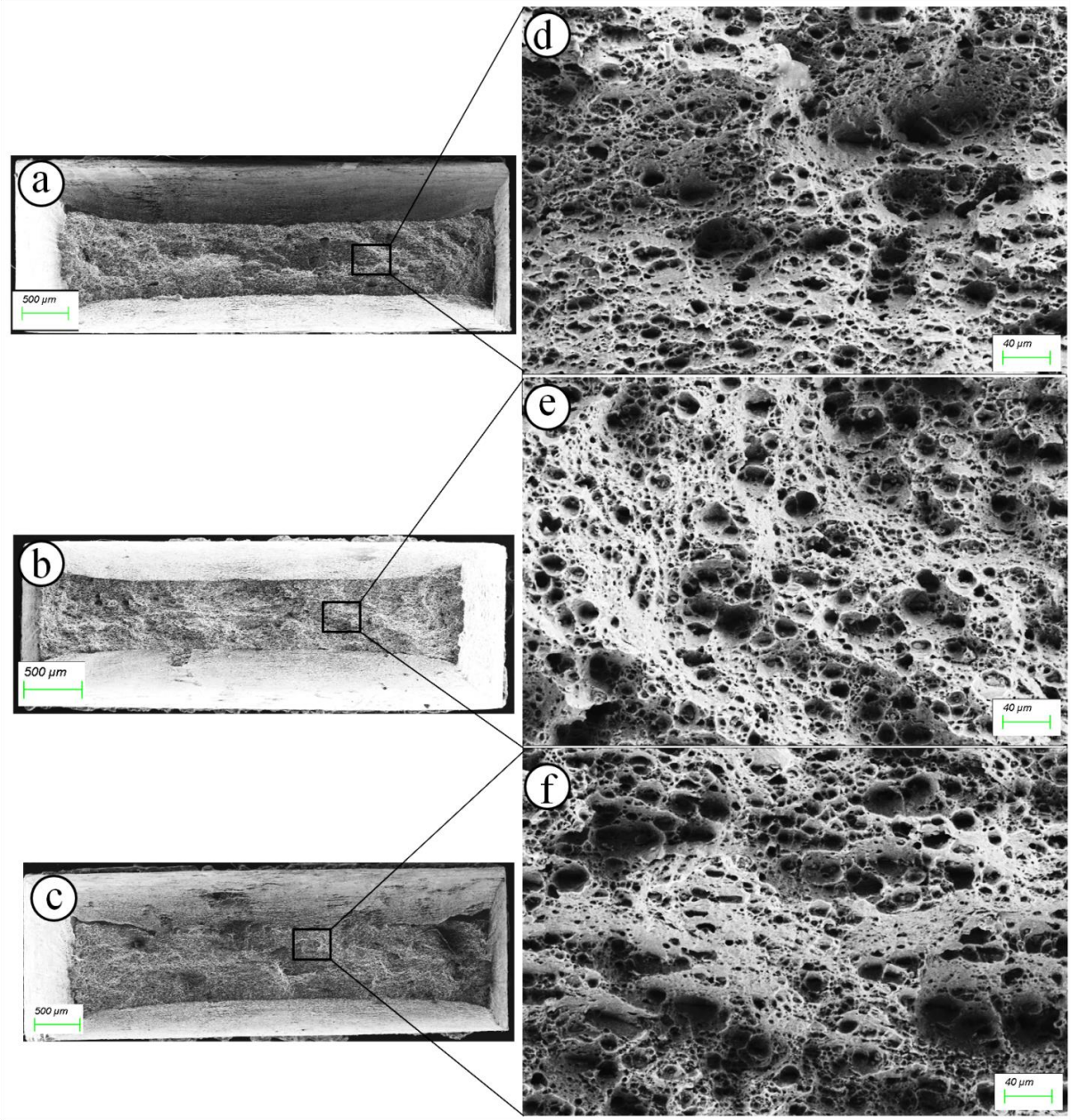

Figure 5.26: Fracture surface of tensile sample at low magnification in (a) as-deposited, (b) FSP, (c) FSP-W, and at high magnification (d) as-deposited, (e) FSP and (f) FSP-W

SUMMARY

In this chapter, the discussion on developments of two types of Ni based FGMs with different processing conditions by using the gas tungsten arc welding-wire and arc additive manufacturing process (GTAW-WAAM) have been highlighted and discussed in details. The variation in the composition of the proposed FGM has been achieved by feeding different combinations of wire. The effect of gradual variation of compositional elements on mechanical and metallurgical properties have been studied and presented. The friction stir processing (FSP) was applied as a post process treatment. The effect of FSP on fabricated FGM at different active cooling environment has also been studied.

Chapter 6

DEVELOPMENT OF TRIMETALLIC FGMS BY USING GMAW AND THEIR CHARACTERIZATIONS

6.1 INTRODUCTION

The SS316L is a kind of austenitic stainless steel widely recognized for its exceptional resistance to corrosion, favorable mechanical characteristics, and outstanding ductility[80]. The duplex steel is a mixed phases material that combines the properties of austenitic and ferritic stainless steel. It results in a synergistic blend of corrosion resistance and superior mechanical strength[157]. The material has favorable mechanical strength and demonstrates notable resistance against stress corrosion cracking. The Inconel 718 (IN718) is a nickel-based superalloy known, for its remarkable strength and resistance to corrosion and oxidation at elevated temperatures. In cryogenic applications, Inconel alloy and stainless steel are commonly used in thermal and nuclear plants [61]. Due to their distinct joint properties, duplex stainless steel and Inconel alloys are frequently utilised in subsea applications [158]. This study utilized stainless steel (ER316L), duplex steel (ER2205), and IN718 metal wires, as these alloys are commonly employed under specific operational conditions in various contemporary industrial sectors [153]. The Wire and Arc Additive Manufacturing (WAAM) process was employed to develop a trimetallic Functionally Graded Material (FGM).

6.2 EXPERIMENTAL SETUP OF GMAW-WAAM

The customized setup has been developed in-house, for depositing the layer, as depicted in Figure 6.1. This setup comprises a 2D motion-controlled work table, enabling movement along the X and Y axis and a welding torch capable of motion along the Z-axis, as illustrated in Figure 6.1 (a). An AC/DC gas metal arc welding (GMAW) welding transformer (Make: REMSWEGS MARKETING PVT. LTD; Model: ZUPER ARC-300) was utilized for layer deposition. The welding machine includes a welding torch, wire feed controller, and an argon gas cylinder, as shown in Figure 6.1(b). A mild steel plate measuring 200 mm x 100 mm x 16 mm served as the substrate onto which the multi-layered FGM was deposited.

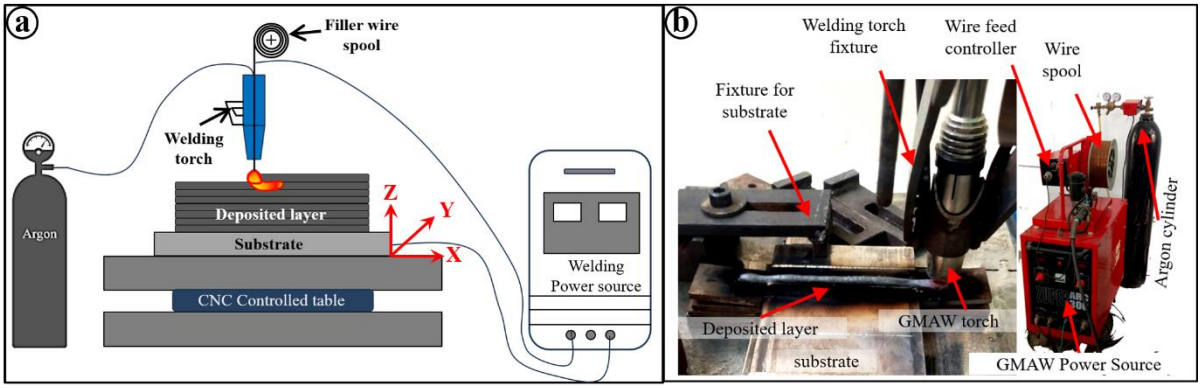

Figure 6.1: (a) Schematic representation of GMAW-WAAM setup, and (b) GMAW-WAAM machine

6.3 FGM SAMPLE PREPARATION STRATEGY

In this study, a trimetallic FGM was developed using ER316L, ER2205 and IN718 wires with a diameter of 1.2 mm by GMAW-WAAM. The nominal compositions of these wires are presented in Table 6.1. The sequence of material deposition was meticulously chosen to ensure a gradual increase in strength from the bottom to the top of the developed trimetallic FGM Table 6.2. Initially, SS316L was deposited, succeeded by ER2205 and then IN718, with each material comprising five consecutive layers.

Table 6.1: Chemical compositions of wire spool

Alloys	Cr	Ni	Mo	Mn	C	Balance
Stainless steel (ER316L) (wt. %)	19.43	13.17	2.43	1.37	0.076	Fe
Duplex steel (ER2205) (wt. %)	22.45	5.78	2.64	1.76	0.56	Fe
Inconel 718 (IN718) (wt. %)	53.25	19.21	3.1	5.21	0.3	Fe

Table 6.2: Mechanical properties of wire spool

Mechanical properties	Hardness (HV)	Tensile strength (MPa)	Yield strength (MPa)	%Elongation
ER316L	206 ± 4.7	575 ± 9	395 ± 9.6	38 ± 2.1
ER2205	230 ± 5.1	665 ± 15.3	408 ± 9.6	26 ±2
Inconel 718	217 ± 5.1	1305 ± 11.3	1032 ± 7.6	25 ± 3.1

6.4 DEVELOPMENT OF TRIMETALLIC FGMs

The GMAW process parameters for the deposition of materials were selected based on the trial experiments and presented in Table 6.3. The welding grade argon with 99% purity was used as a shielding gas with a flow rate of 12 *l*/min during the deposition. Five layers of each material were sequentially deposited, commencing with the deposition of ER316L onto the substrate, followed by ER2205, and concluding with IN718, all while maintaining a 6 mm gap between the torch and substrate. The welding current used was 145 A for the initial layers and gradually decreased to 140 A up to 15 layers. The welding torch speed was maintained 7 mm/s, and the wire feed was adjusted between 1.2-1.5 m/min. Each layer thickness of approximately 2±0.5 mm was obtained during deposition. The final built dimension of the deposited FGM was 200 mm x 7 mm x 27 mm (Figure 6.2).

Table 6.3: Welding parameters for fabrication of FGM

Parameters	Current (DC) (A)	Voltage (V)	Welding torch Travel speed (mm/s)	Wire feed speed (m/min)	Shielding gas	Shielding gas flow rate (*l*/min)
Value	140–145	23-27	7	1.2-1.5	Argon	12

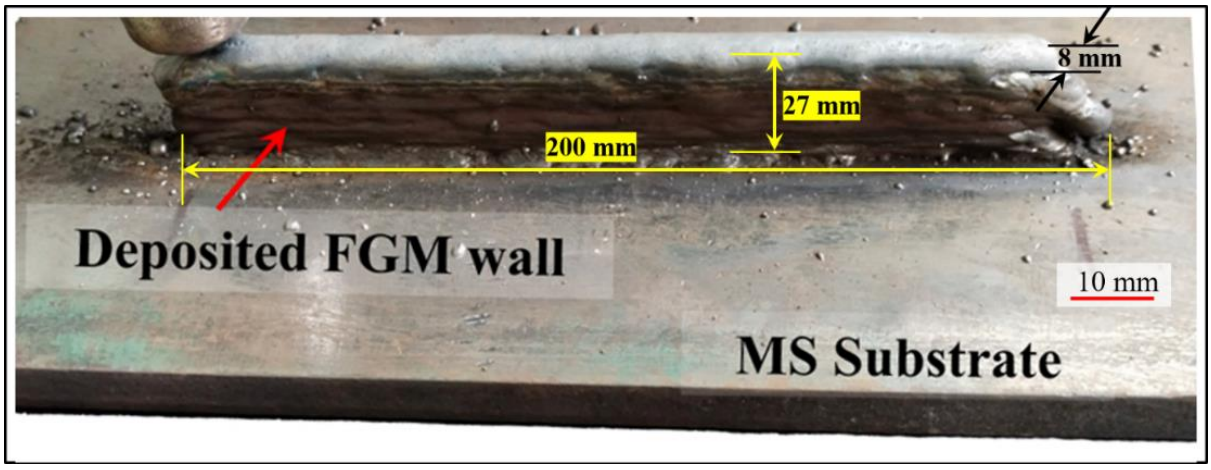

Figure 6. 2: GMAW-WAAM deposited trimetallic FGM sample

6.5 METALLURGICAL CHARACTERIZATION

After fabrication, various samples were extracted for metallurgical and mechanical characterization, as depicted in Figure 6.3 (a and b). The dimensions of tensile sample are schematically illustrated in Figure 6.3 (c). The extracted samples underwent grinding and polishing procedures following metallographic standards. Subsequently, the FGM sample underwent electrochemical etching using a solution comprising perchloric acid and methanol in an 80:20 ratio to reveal the microstructure. Microstructural analysis of the deposited FGM sample was conducted using OM and SEM. EDS was employed to measure elemental distributions within various sections of the specimens. Microhardness testing was performed using a 200 g load and 15 s dwell time. Furthermore, miniature tensile tests were carried out along and across the built direction to investigate the tensile behaviour of the developed trimetallic FGM.

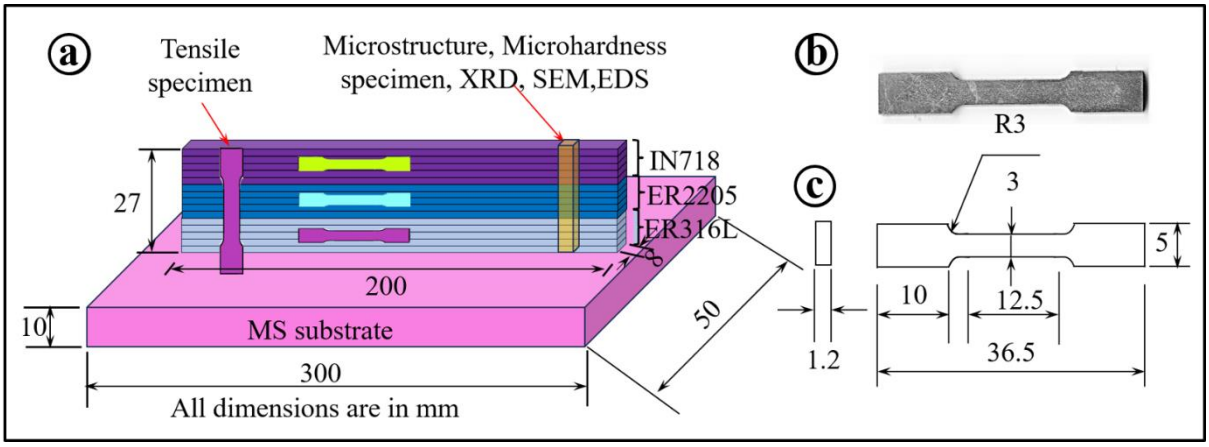

Figure 6.3: (a) schematic diagram of specimen extraction, (b) tensile test specimen and (c) dimensions of tensile sample

6.5.1 Microstructural Investigation (OM/SEM)

The developed FGM sample's macrograph illustrates the molten pool's spread toward the edges during deposition, causing the curvature of the inter-layer boundaries, as depicted in Figure 6.4 (a). The macrograph of the deposited trimetallic FGM sample displays a sharp interface between ER2205 and IN718, with the light region representing IN718 and the dark regions corresponding to ER2205 and ER316L. However, the interface between stainless steel and duplex steel is not discernible in the macrograph. The OM micrographs at various location of trimetallic FGM are presented in Figure 6.4 (b-g). The microstructure of the trimetallic FGM

revealed equiaxed grains, cellular structure, columnar and acicular dendrite grain morphologies[80]. The pores are observed near the substrate, which might be due to rapid solidification, in complete fusion and entrapment of gas takes place as shown in the microstructure of SS zone (Figure 6.4 (b-c)) [159]. In the duplex steel region, acicular dendritic grains are observed, and their size decreases near the interface region, as shown in Figure 6.4 (d-e). In the Inconel region, cellular dendrites, equiaxed dendrites, and columnar grains are observed (Figure 6.4 (f-g)). For better understanding, SEM micrography was performed. The fabricated samples along with SEM micrographs at various locations of the trimetallic FGM sample are presented in Figure 6.5 (a-g). Specifically, Figure 6.5 (a) depicts the fabricated sample showing location of microstructural evaluation. Figure 6.5 (b) illustrates the microstructure of the stainless-steel region, where clusters of austenite (γ) grains are oriented along the built direction, and δ-ferrite is observed at the grain boundary region. Notably, the formation of acicular δ-ferrite was observed to occur more readily than skeletal δ-ferrite at the melting boundary, attributed to the rapid dissipation of heat from the interface [160]. Figure 6.5 (c) depicts the interface between stainless steel and duplex steel, highlighted by the yellow dotted line. A sharp boundary is visible at the interface due to the different alloy compositions. The grain orientation is different, possibly attributed to solidification and temperature gradient variations. Figure 6.5 (d) displays a micrograph of duplex steel, where the white region corresponded to the austenite phase (γ), while the dark black region corresponded to the ferrite phase (α). In this region, the needle-shaped grains are visible, indicating the martensite structure. Figure 6.5 (e) depicts the interface between ER2205 and IN718, displaying a sharp boundary resulting from the substantial difference in principal alloying elements. In IN718 region, the distinct metal carbide type precipitates [MC type precipitates] of nickel (Ni), molybdenum (Mo), and niobium (Nb) become evident, and it is highlighted with red dotted circle in Figure 6.5 (e & f) and its magnified view (Figure 6.5 (g)) shows the presence of laves phase (light grey phase), as well as inclusions rich in titanium (Ti) and niobium (Nb)[47].

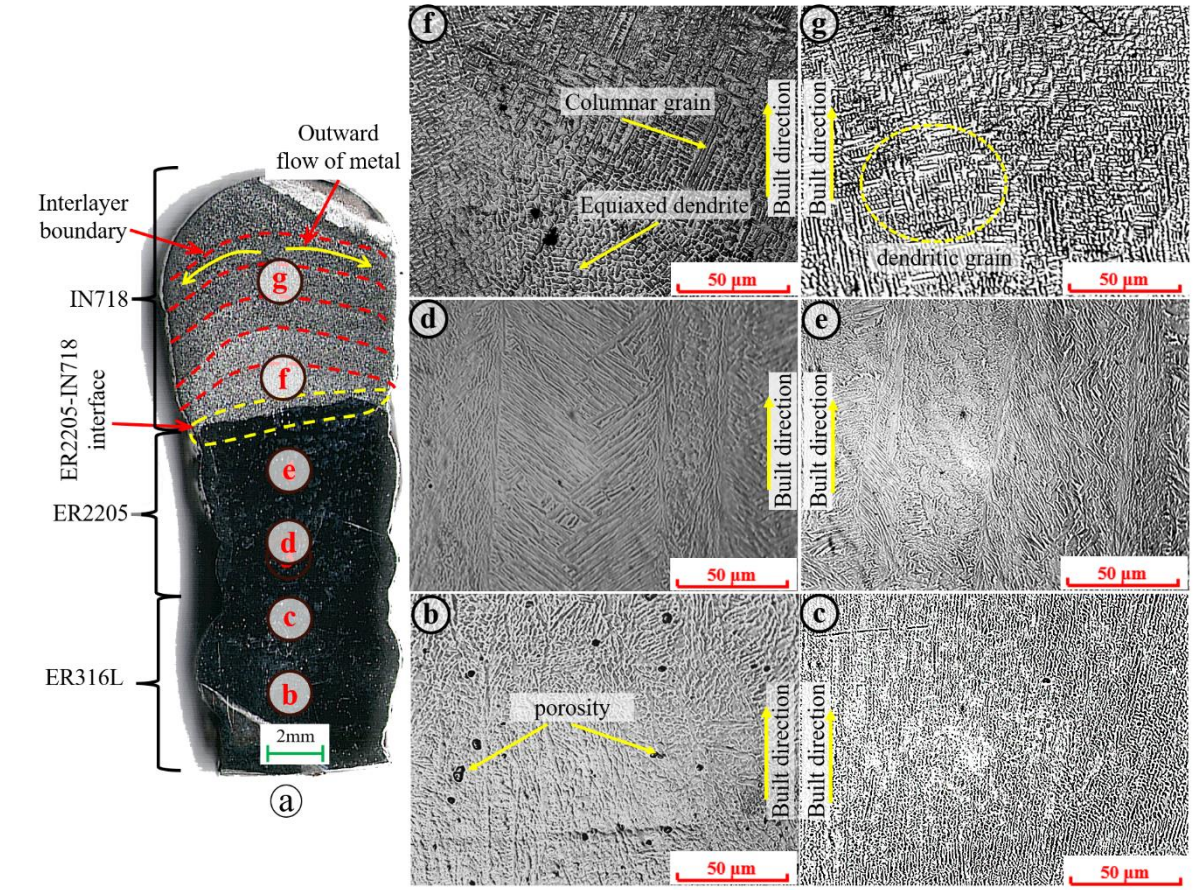

Figure 6.4: (a) Fabricated trimetallic FGM sample, Microstructure at different location (b and c) ER316L zone, (d and e) ER2205 zone and (f and g) IN718 zone

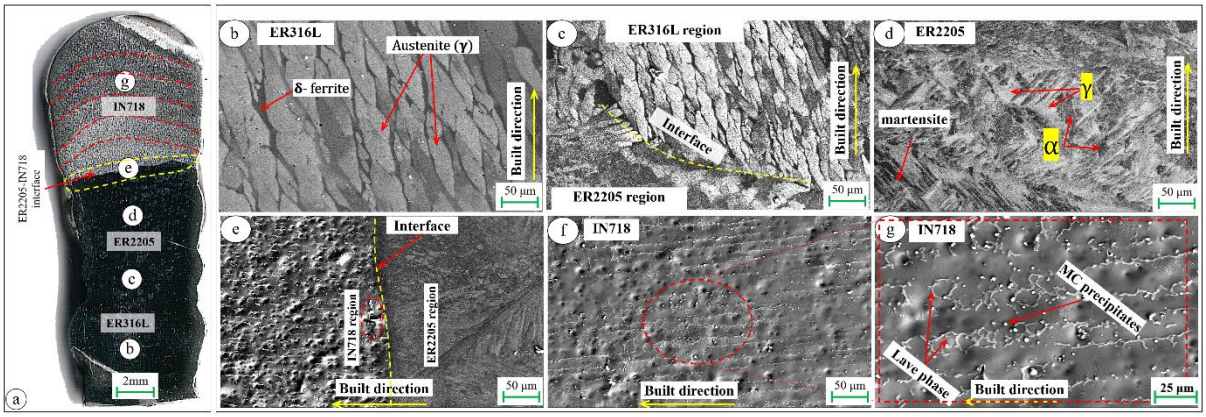

Figure 6.5: (a) Trimetallic FGM sample showing the location of microstructural evaluation at (b) ER316L, (c) the interface of ER316L and ER2205, (d) ER2205, (e) the interface of ER2205 and IN718, (f) IN718, and (g) magnified microstructure of IN718

6.5.2 EBSD Analysis

The electron backscatter diffraction (EBSD) analysis of the trimetallic FGM sample was also conducted, focusing on samples extracted from the interface between IN718 and ER2205 regions (Figure 6.6 (a)). In the EBSD analysis, distinct grain characteristics were observed in the different regions. Large columnar grains are observed in IN718 region, whereas, equiaxed and cellular structured grains in the ER2205 region (Figure 6.6 (b)). The observed grain structures in ER2205 are consistent with those commonly found in WAAM samples due to the influence of multiple thermal cycles during layer deposition. The EBSD micrograph of the trimetallic FGM sample revealed an absence of defects at the interface. Also, a transition in grain morphology from fine grains to large columnar grains was observed at the interface along the built direction. In ER2205 zone the inclination of grains with deposition height is more while as in IN718 zone its inclination is less. The grain boundary map, depicted in Figure 6.6 (c) provided insights the misorientation at different material in the deposited sample. The misorientation angles of most of the grains are more than 15° as shown in Figure 6.6 (d) depicting excess amount of high angle boundary.

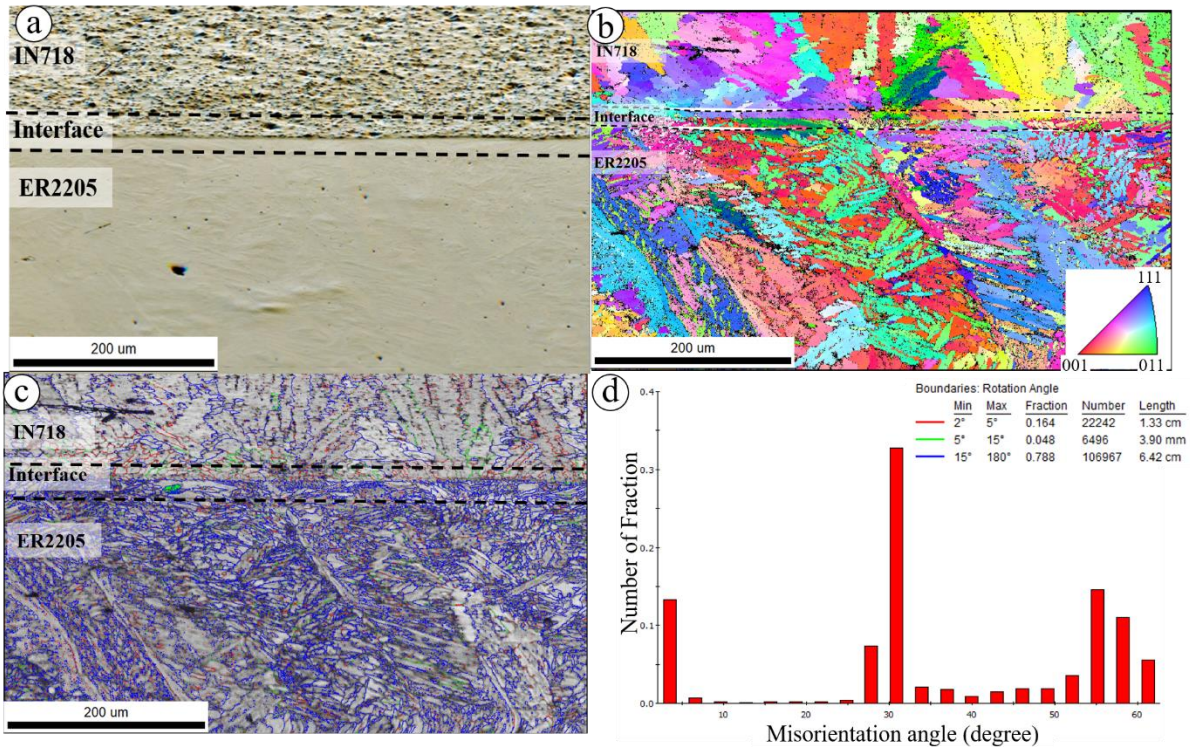

Figure 6.6: EBSD micrograph of (a) ER2205-IN718 interface, (b) color contrast, (c) grain boundary map and (d) misorientation angle v/s number of fraction histogram

6.5.3 EDS Analysis

EDS analysis was conducted to gain an insight into the mixing behaviour of the compositional gradient at different locations within the deposited trimetallic FGM, and the results can be seen in Figure 6.7 and 6.8. Figure 6.7 (a-i) represent the result of spatial arrangement of the primary alloying elements in the IN718 material. The precipitates of the metal carbides of niobium (Nb), titanium (Ti), and molybdenum (Mo), are clearly depicted by red circles in Figure 6.7 (a). These results align with findings reported in the existing literature [51]. The presence of these precipitates may be observed in the elemental distribution depicted in Figure 6.7 (d, h and i) inside the nickel matrix. The titanium and niobium-rich carbo-nitride has also been reported in various experimental studies on IN718 materials [160, 161]. The Laves phase indicates the elemental segregation resulting from a significant heat input and a gradual cooling rate [162] during the deposition through WAAM.

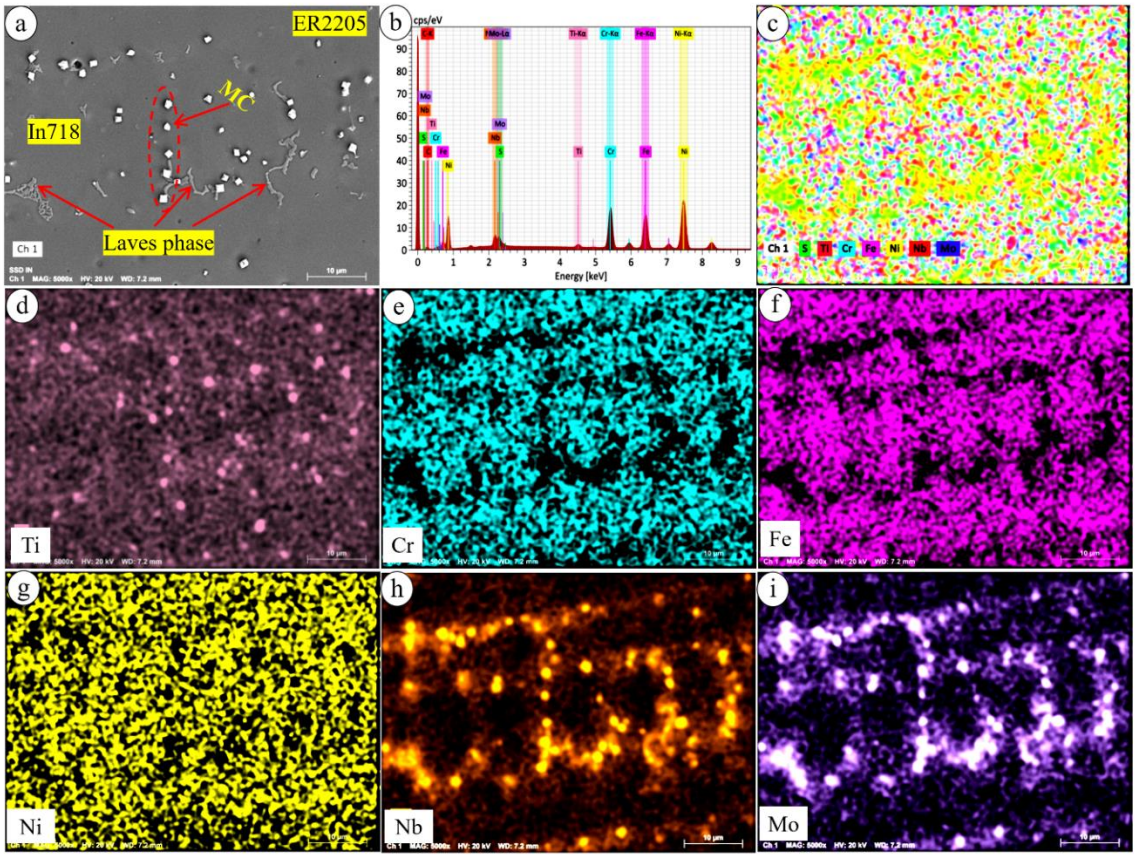

Figure 6.7: EDS mapping of IN718: (a) SEM image showing precipitates and Laves phase (b) mapping of the element, (c) EDS element peaks and individual mapping of elements (d) titanium, (e) chromium, (f) iron, (g) nickel, (h) niobium, and (i) molybdenum

The presence of NbC is anticipated in the microstructure during the initial stages of solidification in the IN718 alloy before forming the Laves phase [163]. Conversely, distinct grain boundaries are not readily apparent in the Inconel region. However, it may be inferred that the presence of precipitate segregation likely gives the presence of some grain boundaries (Figure 6.8 (a)). Figure 6.8 (c) illustrate the EDS line mapping of ER2205-IN718 interface. It is observed in the interface zone that the iron content is diluting with rising concentration of nickel; and the chromium and molybdenum concentrations, on the other hand, display slight variations that remain relatively consistent. A concentration gradient of the constituent element from ER2205 to IN718 at this particular site is shown in Figure 6.8 (b, e, f and h).

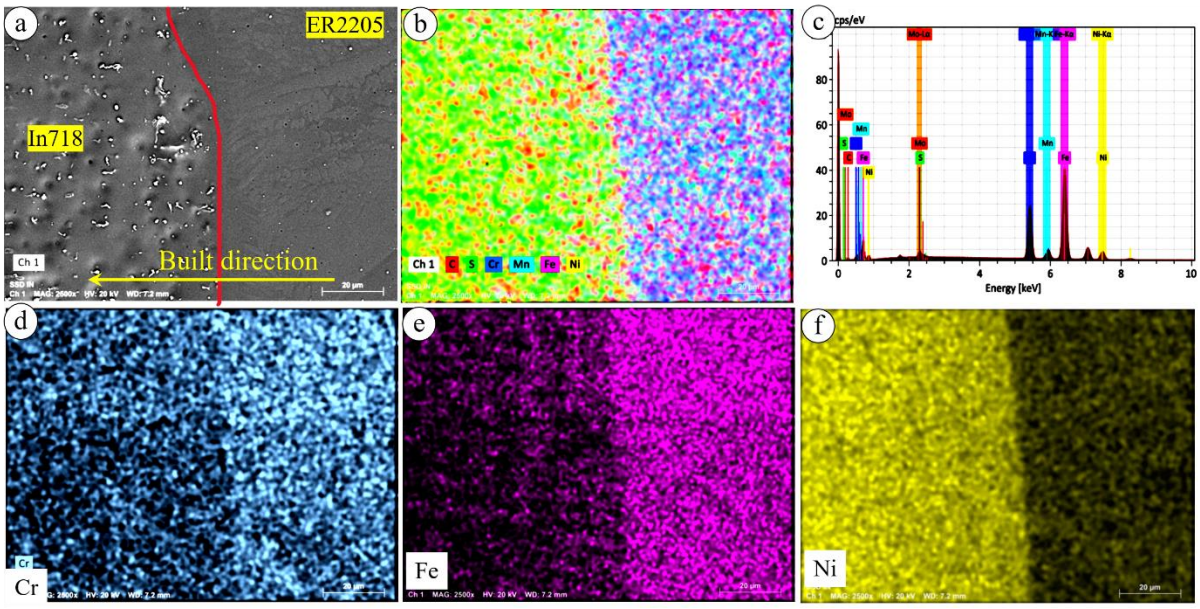

Figure 6.8: EDS mapping at ER2205-IN718 interface zone: (a) SEM image, (b) mapping of the element, (c) EDS element peaks of (d) chromium, (e) iron and (f) nickel

6.5.4 Temperature Profile

The temperature profile throughout the material deposition process was monitored using a thermocouple, which is attached to the substrate 10 mm away from the deposition center line and illustrated in Figure 6.9 (a). The corresponding temperature variations recorded by this thermocouple are presented in Figure 6.9 (b). The graph provides a comprehensive representation of the thermal profile, detailing temperature changes over time during the deposition process. The graph shows a sharp linear increase in temperature leading to a peak temperature, followed by a pronounced and gradual decrease. The thermal profile serves as a

critical parameter that provides heating and cooling rates during deposition of various layers. From the graph, it is observed that peak temperature decreases with each subsequent layer, attributable to the increasing distance from the thermocouple attachment point.

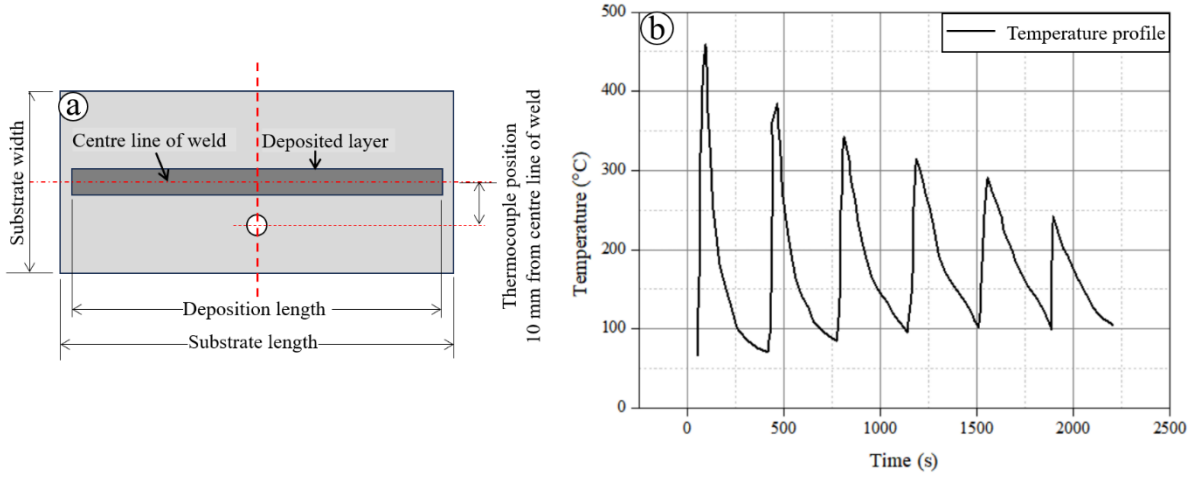

Figure 6.9: (a) Schematic representation of location of thermocouple during fabrication of FGM and (b) temperature profile

6.6 MECHANICAL CHARACTERIZATION

6.6.1 Vicker's Microhardness Investigation

Figure 6.10 (a) illustrates the locations where hardness measurements were conducted, along the built direction and across it. The microhardness values measured at different locations along and across the built direction are presented in Figure 6.10 (b). The hardness was measured along the width with a 1 mm gap and was found to be approximately the same value. The hardness profile along the build direction in the regions of ER316L and ER2205 exhibits an increment. However, a decrease in hardness (Figure 6.10 (b)) is observed at the interface between ER2205 and IN718 (Figure 6.10 (d) and Figure 6.11). This phenomenon is likely a consequence of significant composition variations at the interface, as evident in Figure 6.10 (c) and Figure 6.10 (e), where there is a transition from ER2205 to IN718, resulting in a reduction in iron and chromium content. Kim et al. also observed a similar decrease in hardness at the interface on the IN718 side [131]. Subsequently, within the IN718 zone, there is a resurgence in hardness, it happens due to the presence of MC-type precipitates within the IN718 zone Figure 6.7 (a). The average hardness values for ER316L, ER2205, and IN718 were measured to be 229.17 ± 2 HV, 250.49 ± 3 HV, and 233.25 ± 2.7 HV, respectively.

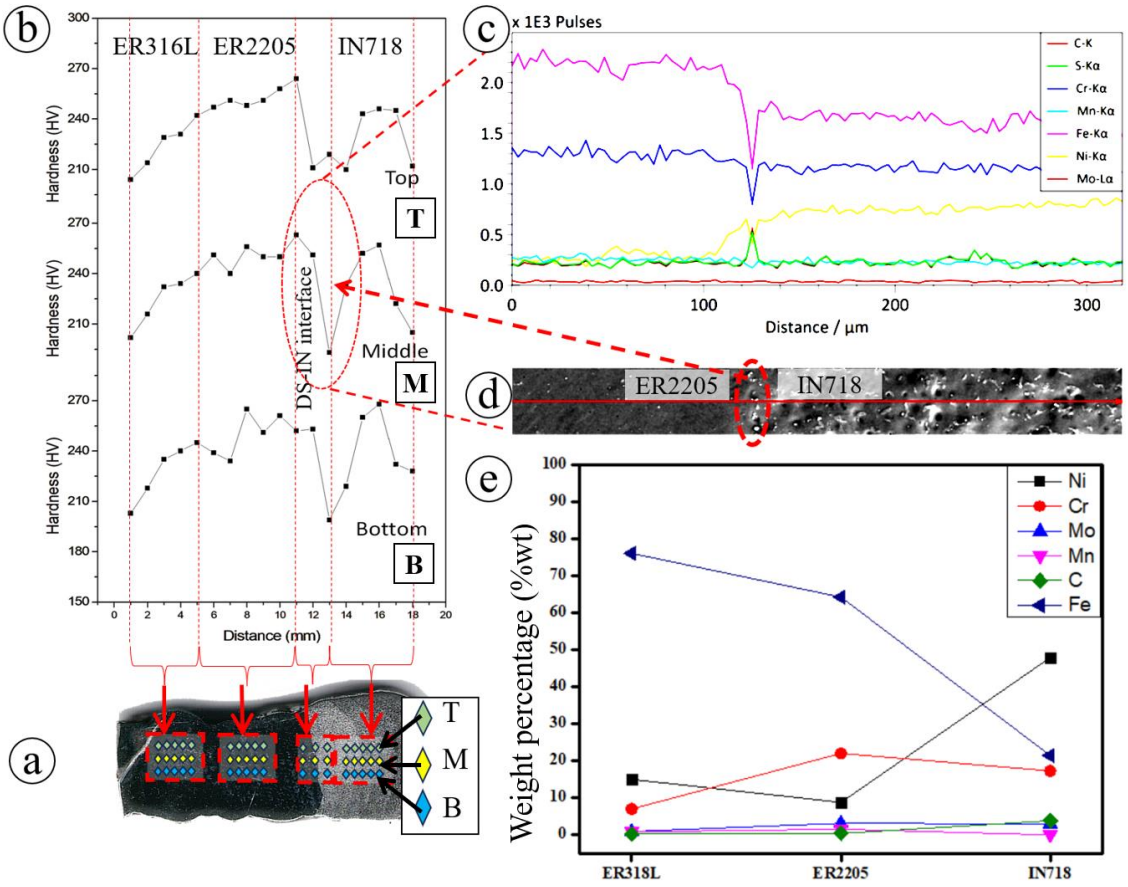

Figure 6.10: Microhardness profile along the built direction, (b) location of hardness reading, (c) line mapping, (d) location of line mapping and (e) principal alloying element profile

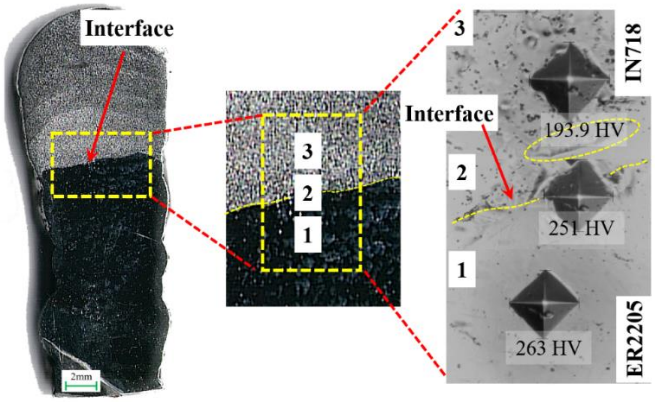

Figure 6.11: Hardness at the interface of ER2205-IN718

6.6.2 Tensile Strength Assessment

The tensile samples were extracted across the deposition height at three distinct locations and along the deposition height, as illustrated in Figure 6.1 (c). Three samples for each set were extracted and tested. The uniaxial tensile test results for ER316L, ER2205, and IN718, considering both orientations, are presented in Figure 6.12 (a-d). The stress-strain curves elucidate variations in the tensile strength of the deposited FGM at different locations, a consequence of the distinct mechanical properties inherent in the constituent materials. Specifically, ER316L exhibited a higher elongation but lower tensile strength compared to other materials, as depicted in Figure 6.12 (a). The increase in % elongation may happen due to presence of cluster of austenite γ-phase along with long columnar grains while as variation in strength may happens due to presence of α-ferrite phase at the grain boundary (Figure 6.5 (b)). ER2205 displayed higher tensile strength and lower elongation than ER316L, as indicated in Figure 6.12(b). It happens because the orientation of grain is slightly deviated from its deposition height as clearly visible in EBSD micrograph (Figure 6.6 (b)). The highest tensile strength was observed in IN718, as presented in Figure 6.12(c) which is obvious because of inherent mechanical property of IN718 and presence of precipitates. The tensile results of individual materials are in line with the published literature [153]. The sample along the deposition height exhibits tensile strength higher than ER316L and lower than IN718, as illustrated in Figure 6.12 (d) it is because of different grain morphology present throughout the FGM wall due to change in composition of material and cyclic heat supply during deposition. For a more apparent viewpoint, the average tensile data is also presented in Figure 6.12 (e), which shows gradual increase in tensile strength and decrease in % elongation along the height, which satisfied the objective of fabrication of trimetallic FGM. In along the built direction the sample fails at ER316L-ER2205 interface (Figure 6.12 (f)). The tensile properties of deposited material across the built direction are also comparable with the published results of bimetallic FGM of SS316 and IN625 alloy [124]. A comprehensive comparison of the mechanical properties of the WAAM fabricated ER316L, ER2205, and IN718-based trimetallic FGM with the respective feedstock wire is provided in Table 6.4. The tensile characteristics of the fabricated trimetallic FGM were compared to the respective feedstock wires of ER316L, ER2205, and IN718. For ER316L, the fabricated FGM exhibited a decrease of 17.06% in tensile strength (from 580 MPa to 481.05 MPa) and an increase of 18.91% in strain (from 38% to 45.19%). Similarly, ER2205 showed a 10.27% reduction in tensile strength (from 655 MPa to 587.70 MPa) but a notable 53.2% increase in strain (from 25% to 38.3%). In the case of

IN718, there was a substantial 33.22% decrease in tensile strength (from 1314 MPa to 877.40 MPa) and a minor 3.66% decrease in strain (from 27% to 26.01%). The sample tested along the build height of the fabricated FGM shows tensile strength of 550.66 MPa and 34.12% strain.

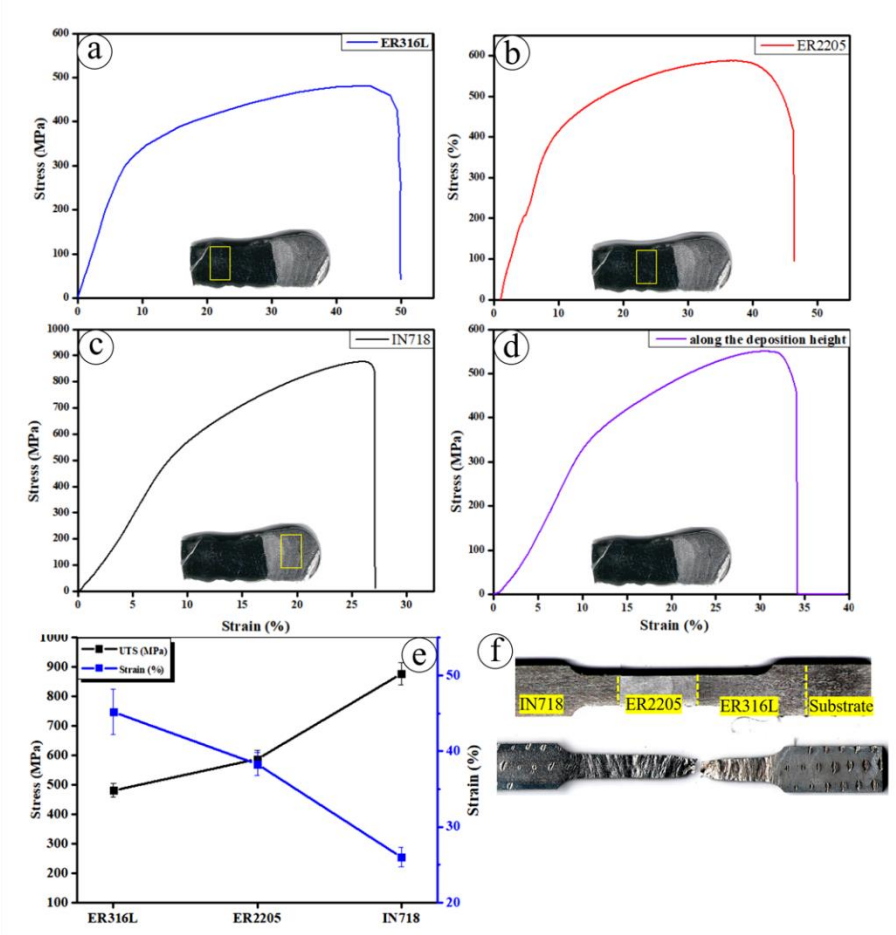

Figure 6.12: Stress-strain curve of (a) ER316L, (b) ER2205, (c) IN718, (d) along the built direction, and (e) maximum tensile strength and % strain along the built direction and (f) tensile samples before and after test

Table 6.4: Comparisons of tensile properties of trimetallic FGM with feedstock wire

Material	Tensile strength (MPa)			Strain (%)		
	Feedstock Wire	Fabricated FGM	% change in tensile strength	Feedstock Wire	Fabricated FGM	% change in strain
ER316E	580	481.05	-17.06	38	45.19	+18.91

ER2205	655	587.70	-10.27	25	38.3	+53.2
IN718	1314	877.40	-33.22	27	26.01	-3.66
Along the height	--	550.66	--	--	34.12	--

6.6.2.1 Fracture Surfaces of Tensile Sample

The fracture surfaces of the tensile samples were examined using scanning electron microscopy (SEM) and are depicted in Figure 6.13 (a-d). The observed fracture surfaces exhibit a mixed mode of failure. In the case of the IN718 sample, the fracture surface appears flat and featureless, indicating low deformation prior to fracture (Figure 6.13 (a)).

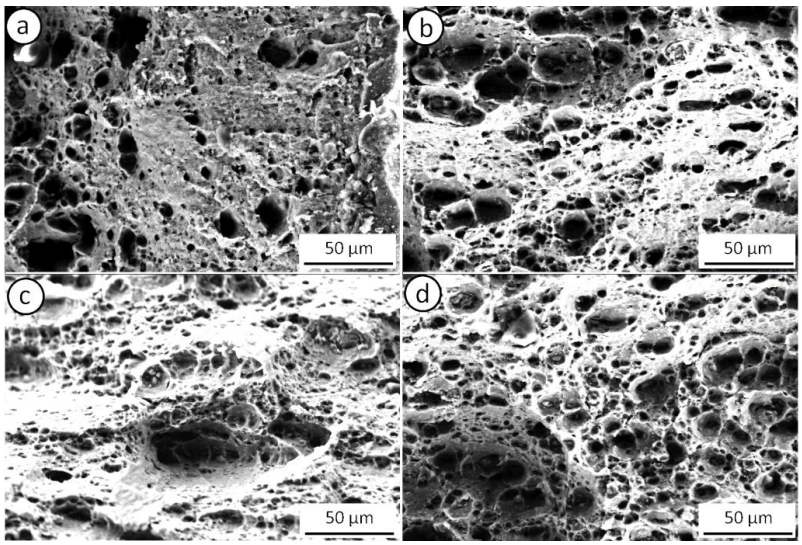

Figure 6.13: Fracture surfaces of tensile samples across the built direction of (a) IN718, (b) ER2205, (c) ER316L and (d) fracture surfaces of tensile samples along the built direction

However, the ER2205 and ER316L samples display a ductile failure mode on the tensile samples, characterized by the presence of dimples of various shapes and sizes as illustrated in Figure 6.13 (b) and Figure 6.13 (c), respectively. The fracture surface of tensile sample tested along the built direction also shows dimples, resembling the fracture surface of ER316L Figure 6.13 (d). This similarity arises because the tensile sample along the built direction fails from the ER316L region, leading to the consistent appearance of dimples on the fracture surface.

SUMMARY

This chapter demonstrates the successful fabrication of a trimetallic FGM incorporating ER316L, ER2205, and IN718 through the GMAW-based WAAM process. The intentional

manipulation of mechanical properties was achieved by depositing the three materials sequentially in the order of ER316L-ER2205-IN718. This particular sequence was adopted to methodically attain a gradual variation in mechanical properties from the bottom to the top of the fabricated structure.

Chapter 7

CONCLUSIONS AND RECOMMENDATIONS OF FUTURE WORK

The development of functionally graded material with graded composition using a multi-wire feed system with gas tungsten arc welding-wire arc additive manufacturing (GTAW-WAAM) has yet to be extensively explored. In this study, an attempt is made to develop Ni-based FGMs. The different materials like, pure nickel, nichrome 80:20, ERNiCrMo-10, and Inconel 625, were used to develop FGMs. The FGMs were fabricated under different processing conditions. To address of the challenge of high heat associated in WAAM processing, a novel post-processing technique known as friction stir processing (FSP) was successfully applied after FGM. Additionally, an active cooling strategy with FSP was demonstrated within the context of WAAM. Subsequently, the developed FGMs underwent comprehensive characterization for their metallurgical and mechanical properties. The major conclusions from this study and opportunities for future research in this area are presented in the following sections.

7.1 CONCLUSIONS

This research successfully fabricated two types of Ni-based FGM utilizing GTAW-WAAM and one trimetallic FGM by using GMAW-WAAM. The findings from all FGM types highlight significant advancements and insights into their metallurgical and mechanical properties.

7.1.1 The Findings from FGM Type-I

The Ni-Cr-Mo based functionally graded material with varying composition of nickel and chromium samples have been fabricated successfully by GTAW-WAAM process. After that metallurgical and mechanical characterization was performed. The following conclusions can be drawn:

i. Columnar and dendritic grains were observed in the as-deposited sample. In contrast, to the FSP sample, the grain orientation changed from being along the deposition direction to across it due to frictional deformation. These changes occurred due to plastic deformation and recrystallization, leading to the formation of fine grains.

ii. The XRD analysis of the developed FGMs reveals the formation of γ-Ni, CrNi3, α-Cr and MoNi4 phases. In FSP sample, the γ-Ni, α-Cr and MoNi4 peaks are more intense than those in the as-deposited samples. This is because FSP provides high temperature distortion during processing and promotes the formation of these precipitates.

iii. The EBSD analysis of as-deposited showed the grain size varied from 257 to 387 µm. This type of grain structure is evident in WAAM samples due to multiple thermal cycles during layer deposition. However, the grain size in FSP samples ranges from 17 to 35 µm. It is happened due to high temperature frictional deformation in FSP sample. Thus, FSP is beneficial in reducing the grain size for improving the mechanical properties of produced FGM from WAAM processes.

iv. The microhardness varies from 142.43±6.5 HV to 331.08±9.2 HV and 165.83±5. HV to 385.19±14 HV from bottom to top in as-deposited and FSP samples respectively. This increasing trend in the microhardness values are due to the increase in concentration of $CrNi_3$ and $MoNi_4$ precipitates. However, the influence of FSP processing helps to further rise in microhardness values of the samples.

v. The tensile strength of as-deposited and FSP samples varies from bottom to top. The FSP processed samples shows upside trend as compared to the as-deposited.

7.1.2 The Findings from FGM Type-II

The Ni-Cr-Mo based functionally graded material with varying composition of nickel and chromium and molybdenum samples have been fabricated successfully by GTAW-WAAM process. The developed samples have been analyzed by results of metallurgical and mechanical characterizations. The following conclusions can be drawn:

i. A gradual compositional gradient of nickel from 93.33 % (bottom layer) to 58.20% (top layer) and molybdenum from zero to 12.5 % with almost constant chromium percentage is achieved along the height of the deposited wall.

ii. The microhardness gradually increases from bottom to top in all cases, due to the increase in molybdenum content. The microhardness values are ranges from 114 ±6.5 – 205 ± 9.2 HV, 116 ± 6.8 – 230 ± 10.3 HV and 164 ± 7.2 – 256 ± 12.23 HV for as-deposited, FSP and FSP-W samples, respectively.

iii. In the as-deposited sample, large columnar and dendritic grains were observed. However, in the FSP sample, finer and deformed grains were evident. Additionally, in

the FSP-W sample, faster grain refinement occurred, resulting in maximum microhardness.

iv. The XRD analysis of as-deposited FGMs reveals the presence of $MoNi_4$ and $Ni_{3.28}Ti_{0.72}$ precipitates in the (111) and (022) crystal planes. The FSP sample exhibits $Mo_{0.4}Ni_{3.6}$, $CrNi_3$, and $Ni_{3.28}Ti_{0.72}$ precipitates in the (111), (022), and (002) crystal planes. Conversely, the FSP-W sample demonstrates the existence of $Cr_{0.4}Ni_{0.6}$ and $Ni_{0.906}Ti_{0.094}$ precipitates in the (111), (022), and (002) crystal planes.

v. The average ultimate tensile strength (UTS) at location-1, where molybdenum is almost negligible, were found 793 MPa, 715 MPa and 875 MPa, respectively for as-deposited, FSP and FSP-W samples. As moving upward at location-2 where molybdenum percentage is in the range of 5 to 9%, the UTS decreases by 3.25 % and 3.5 % in the case of as-deposited and FSP samples while it increases in FSP-W samples by 3.67 %. At location-3 (with 10-12.5% Mo), the UTS increases by 3 %, 12.56 % and 3.42 % for as-deposited, FSP and FSP-W samples, respectively.

7.1.3 The Findings from Trimetallic FGM:

ER316L, ER2205 and IN718 based trimetallic FGM was fabricated by using GMAM-WAAM process. After that metallurgical and mechanical characterization was performed. The following conclusions can be drawn:

i. ER316L exhibited large austenitic (γ) grains with the presence of δ-ferrite phase at the grain boundaries. Similarly, ER2205 displayed a complex microstructure comprising austenite (γ), α-ferrite phases, and martensite phase.

ii. The ER2205 and IN718 showcased a distinct interface, evident in energy-dispersive X-ray spectroscopy (EDX) data, with higher Fe content and lower Ni content in the ER2205 region, and vice versa in the IN718 zone.

iii. Within the IN718 zone, nodular-shaped Laves phases were observed, along with the presence of metal carbides containing Ti, Nb and Mo.

iv. The average microhardness values along the deposition direction increased by approximately 9.29% for ER2205 and 1.78% for IN718 compared to ER316L.

v. The tensile strength along the deposition direction was recorded as 481.05 ±10 MPa in ER316L, 587.7 ± 17 MPa in ER2205, and 877.4 ± 23 MPa in IN718, all exhibiting lower values than their respective feedstock wires. Despite the reduced tensile strength, % elongation is increased by 18.91% and 53.2 % in ER316L and ER2205 respectively

while as in IN718 it is decreased by 3.66 % as compare to feed stock material. The tensile strength and % elongation of trimetallic FGM along the deposition height is 550.66 MPa and 34.12% respectively.

7.2 FUTURE SCOPE

The successful fabrication of FGMs by using multi wire feed system with GTAW-WAAM and trimetallic FGM by using GMAW-WAAM opens avenues for further research and development in several areas. The following suggestions are drawn from current work:

1 Exploration of additional alloy combinations and deposition sequences to achieve tailored material properties for specific applications.

2 Investigation of alternative post-processing techniques, such as surface modification, to further improve material performance.

3 Assessment of the corrosion resistance and fatigue behaviour of the fabricated FGM to evaluate their suitability for real-world applications.

4 Integration of advanced characterization techniques, such as transmission electron microscopy (TEM), to gain deeper insights into microstructural evolution and defect formation during additive manufacturing processes.

Overall, the findings of this research contribute to the advancement in additive manufacturing technology and its applications in fabricating complex, functionally graded materials with tailored mechanical properties.

REFERENCES

1. Mahamood, R.M., et al., *Functionally graded material: an overview.* 2012.

2. Shabana, Y. and N.J.C.p.b.e. Noda, *Thermo-elasto-plastic stresses in functionally graded materials subjected to thermal loading taking residual stresses of the fabrication process into consideration.* 2001. **32**(2): p. 111-121.

3. Tishkevich, D., et al., *Formation and corrosion properties of Ni-based composite material in the anodic alumina porous matrix.* 2019. **804**: p. 139-146.

4. Katz-Demyanetz, A., et al., *Powder-bed additive manufacturing for aerospace application: Techniques, metallic and metal/ceramic composite materials and trends.* 2019. **6**: p. 5.

5. Wang, S.J.J.o.c.m., *Fracture mechanics for delamination problems in composite materials.* 1983. **17**(3): p. 210-223.

6. Shariat, B.S., et al., *Functionally graded shape memory alloys: Design, fabrication and experimental evaluation.* 2017. **124**: p. 225-237.

7. Kumar, P., et al., *Recent trends and future outlooks in manufacturing methods and applications of FGM: a comprehensive review.* 2023. **38**(9): p. 1033-1067.

8. Zhang, C., et al., *Additive manufacturing of functionally graded materials: A review.* 2019. **764**: p. 138209.

9. Tarlochan, F.J.J.A.M.E., *Functionally graded material: a new breed of engineered material.* 2012. **1**(5): p. 1-2.

10. Qu, H., et al., *Microstructure and mechanical property of laser melting deposition (LMD) Ti/TiAl structural gradient material.* 2010. **31**(1): p. 574-582.

11. Parthasarathy, J., B. Starly, and S.J.J.o.M.P. Raman, *A design for the additive manufacture of functionally graded porous structures with tailored mechanical properties for biomedical applications.* 2011. **13**(2): p. 160-170.

12. Chen, B., et al., *Development and characterization of 316L/Inconel625 functionally graded material fabricated by laser direct metal deposition.* 2020. **123**: p. 105916.

13. Mannan, S., J. Paul Knox, and S.J.R.S.o.s. Basu, *Correlations between axial stiffness and microstructure of a species of bamboo.* 2017. **4**(1): p. 160412.

14. Sola, A., D. Bellucci, and V.J.B.a. Cannillo, *Functionally graded materials for orthopedic applications–an update on design and manufacturing.* 2016. **34**(5): p. 504-531.

15. Patricio, M.T., et al., *Relationship between microstructure, phase transformation, and mechanical behavior in Ti–40Ta alloys for biomedical applications.* 2021. **14**: p. 210-219.

16. Yuan, L., S. Ding, and C.J.B.m. Wen, *Additive manufacturing technology for porous metal implant applications and triple minimal surface structures: A review.* 2019. **4**: p. 56-70.

17. Rajan, T. and B.J.I.J.o.A.E.A. Pai, *Development in manufacturing processes of functionally graded materials.* 2009. **2**(5): p. 4-74.

18. Makwana, A.B., K.C. Panchal, and A.H.J.I.J.o.A.M.E. Gandhi, *Stress analysis of functionally graded material plate with cut-out.* 2014. **4**(5): p. 495-500.

19. Ichikawa, K., *Functionally graded materials in the 21st century: a workshop on trends and forecasts*. 2001: Springer Science & Business Media.

20. Udupa, G. and K. Gangadharan. *Future applications of carbon nanotube reinforced functionally graded composite materials*. in *IEEE-international conference on advances in engineering, science and management (ICAESM-2012)*. 2012. IEEE.

21. Mahmoud, D., M.A.J.J.o.M. Elbestawi, and M. Processing, *Lattice structures and functionally graded materials applications in additive manufacturing of orthopedic implants: a review.* 2017. **1**(2): p. 13.

22. Cooley, W.G., *Application of functionally graded materials in aircraft structures.* 2005.

23. Zoli, M.J.P.B.C.M., *Polaronic features in the Su–Schrieffer–Heeger model.* 2003. **329**: p. 1554-1555.

24. Niino, M., K. Kisara, and M. Mori. *Feasibility study of FGM technology in space solar power systems (SSPS)*. in *Materials Science Forum*. 2005. Trans Tech Publ.

25. El-Galy, I.M., B.I. Saleh, and M.H.J.S.A.S. Ahmed, *Functionally graded materials classifications and development trends from industrial point of view.* 2019. **1**: p. 1-23.

26. Ngo, T.D., et al., *Additive manufacturing (3D printing): A review of materials, methods, applications and challenges.* 2018. **143**: p. 172-196.

27. Lu, L., et al., *Microstructure and mechanical properties of a functionally graded material from TA1 to Inconel 625 fabricated by dual wire+ arc additive manufacturing.* 2021. **298**: p. 130010.

28. Loh, G.H., et al., *An overview of functionally graded additive manufacturing.* 2018. **23**: p. 34-44.

29. Yan, L., Y. Chen, and F.J.A.M. Liou, *Additive manufacturing of functionally graded metallic materials using laser metal deposition.* 2020. **31**: p. 100901.

30. Conner, B.P., et al., *Making sense of 3-D printing: Creating a map of additive manufacturing products and services.* 2014. **1**: p. 64-76.

31. Singh, P.K., et al., *Effect of Build Orientation on Metallurgical and Mechanical Properties of Additively Manufactured Ti-6Al-4V Alloy.* 2023: p. 1-18.

32. Zhang, Y. and A.J.A.M. Bandyopadhyay, *Direct fabrication of compositionally graded Ti-Al2O3 multi-material structures using Laser Engineered Net Shaping.* 2018. **21**: p. 104-111.

33. Chowdhury, S., et al., *Laser powder bed fusion: a state-of-the-art review of the technology, materials, properties & defects, and numerical modelling.* 2022. **20**: p. 2109-2172.

34. Du Plessis, A., et al., *Effects of defects on mechanical properties in metal additive manufacturing: A review focusing on X-ray tomography insights.* 2020. **187**: p. 108385.

35. Frazier, W.E.J.J.o.M.E. and performance, *Metal additive manufacturing: a review.* 2014. **23**: p. 1917-1928.

36. Mansoura, A., et al., *Selective Laser Melting of Stainless Steels: A review of Process, Microstructure and Properties.* 2024: p. 1-29.

37. Horn, T.J. and O.L.J.S.p. Harrysson, *Overview of current additive manufacturing technologies and selected applications.* 2012. **95**(3): p. 255-282.

38. Wang, F., et al., *Microstructure and mechanical properties of wire and arc additive manufactured Ti-6Al-4V.* 2013. **44**: p. 968-977.

39. Meng, W., et al., *Additive manufacturing of a functionally graded material from Inconel625 to Ti6Al4V by laser synchronous preheating.* 2020. **275**: p. 116368.

40. Rock, C., et al., *Additive manufacturing of pure Mo and Mo+ TiC MMC alloy by electron beam powder bed fusion.* 2020. **72**: p. 4202-4213.

41. Unocic, R., J.J.M. DuPont, and m.t. B, *Process efficiency measurements in the laser engineered net shaping process.* 2004. **35**: p. 143-152.

42. Rännar, L.E., A. Glad, and C.G.J.R.P.J. Gustafson, *Efficient cooling with tool inserts manufactured by electron beam melting.* 2007. **13**(3): p. 128-135.

43. Stenbacka, N., I. Choquet, and K. Hurtig. *Review of arc efficiency values for gas tungsten arc welding*. in *IIW Commission IV-XII-SG212, Intermediate Meeting, BAM, Berlin, Germany, 18-20 April, 2012*. 2012.

44. Heralic, A., *Monitoring and control of robotized laser metal-wire deposition*. 2012, Chalmers University of Technology.

45. Williams, S.W., et al., *Wire+ arc additive manufacturing.* 2016. **32**(7): p. 641-647.

46. Ralph, B., *Method of making decorative articles*. 1925, Google Patents.

47. Wu, B., et al., *A review of the wire arc additive manufacturing of metals: properties, defects and quality improvement.* 2018. **35**: p. 127-139.

48. Martina, F., et al., *Residual stress of as-deposited and rolled wire+ arc additive manufacturing Ti–6Al–4V components.* 2016. **32**(14): p. 1439-1448.

49. Wu, B., et al., *The effects of forced interpass cooling on the material properties of wire arc additively manufactured Ti6Al4V alloy.* 2018. **258**: p. 97-105.

50. Satish Kumar, P., L. Suvarna Raju, and L. Siva Rama Krishna. *A review on wire arc additive manufacturing (WAAM) fabricated components of Ti6AL4V and steels*. in *International Conference on Emerging Trends in Engineering (ICETE) Emerging Trends in Smart Modelling Systems and Design*. 2020. Springer.

51. Seow, C.E., et al., *Wire+ Arc Additively Manufactured Inconel 718: Effect of post-deposition heat treatments on microstructure and tensile properties.* 2019. **183**: p. 108157.

52. Colegrove, P.A., et al., *Application of bulk deformation methods for microstructural and material property improvement and residual stress and distortion control in additively manufactured components.* 2017. **135**: p. 111-118.

53. Neubrand, A. and J.J.I.J.o.M.R. Rödel, *Gradient materials: An overview of a novel concept.* 2021. **88**(5): p. 358-371.

54. Koizumi, M. *Recent progress of functionally gradient materials in Japan*. in *16th annual conference on composites and advanced ceramic materials*. 1992.

55. Koizumi, M.J.C.p.b.e., *FGM activities in Japan.* 1997. **28**(1-2): p. 1-4.

56. Jha, D., T. Kant, and R.J.C.s. Singh, *A critical review of recent research on functionally graded plates.* 2013. **96**: p. 833-849.

57. Saleh, B., et al., *Review on the influence of different reinforcements on the microstructure and wear behavior of functionally graded aluminum matrix composites by centrifugal casting.* 2020. **26**: p. 933-960.

58. Jamaludin, S.N.S., et al., *A review on the fabrication techniques of functionally graded ceramic-metallic materials in advanced composites.* 2013. **8**(21): p. 828-840.

59. Ruys, A., et al., *Functionally graded electrical/thermal ceramic systems.* 2001. **21**(10-11): p. 2025-2029.

60. Hofmann, D.C., et al., *Compositionally graded metals: A new frontier of additive manufacturing.* 2014. **29**(17): p. 1899-1910.

61. Rodriguez, J., et al., *Functionally graded SS 316L to Ni-based structures produced by 3D plasma metal deposition.* 2019. **9**(6): p. 620.

62. Li, W., et al., *Comprehensive studies of SS316L/IN718 functionally gradient material fabricated with directed energy deposition: Multi-physics & multi-materials modelling and experimental validation.* 2023. **61**: p. 103358.

63. Wang, H., et al., *Fracture mechanism of a dissimilar metal welded joint in nuclear power plant.* 2013. **28**: p. 134-148.

64. Samal, M., et al., *Investigation of failure behavior of ferritic–austenitic type of dissimilar steel welded joints.* 2011. **18**(3): p. 999-1008.

65. Yeh, T.-K., et al., *Stress corrosion cracking in dissimilar metal welds with 304L stainless steel and Alloy 82 in high temperature water.* 2013. **63**: p. 7-11.

66. Reichardt, A., *Additive Manufacturing of Metal-Based Functionally Graded Materials*. 2017: University of California, Berkeley.

67. Udupa, G., S.S. Rao, and K.J.P.M.S. Gangadharan, *Functionally graded composite materials: an overview.* 2014. **5**: p. 1291-1299.

68. Li, L. and Y. Li. *Development and trend of ceramic cutting tools from the perspective of mechanical processing*. in *IOP Conference Series: Earth and Environmental Science*. 2017. IOP Publishing.

69. Lengauer, W., K.J.J.o.a. Dreyer, and compounds, *Functionally graded hardmetals.* 2002. **338**(1-2): p. 194-212.

70. Saleh, B., et al., *30 Years of functionally graded materials: An overview of manufacturing methods, Applications and Future Challenges.* 2020. **201**: p. 108376.

71. Borisov, E., et al., *Structure and properties of Ti/Ti64 graded material manufactured by laser powder bed fusion.* 2021. **14**(20): p. 6140.

72. Shah, K., et al., *Parametric study of development of Inconel-steel functionally graded materials by laser direct metal deposition.* 2014. **54**: p. 531-538.

73. Lin, X., T.M.J.M.S. Yue, and E. A, *Phase formation and microstructure evolution in laser rapid forming of graded SS316L/Rene88DT alloy.* 2005. **402**(1-2): p. 294-306.

74. Terrazas, C.A., et al., *Multi-material metallic structure fabrication using electron beam melting.* 2014. **71**: p. 33-45.

75. Popoola, P., et al., *Laser engineering net shaping method in the area of development of functionally graded materials (FGMs) for aero engine applications-a review.* 2016. **2**: p. 64.

76. Standard, A.J.A.I.F.-a., *Standard terminology for additive manufacturing technologies.* 2012: p. 1-9.

77. Bayode, A., E. Akinlabi, and S.L. Pityana, *Fabrication of stainless steel based FGM by laser metal deposition*. 2018, De Gruyter.

78. Gunasekaran, J., P. Sevvel, and I.J.J.M.T.P. Solomon, *Metallic materials fabrication by selective laser melting: A review.* 2021. **37**: p. 252-256.

79. Bobbio, L.D., et al., *Additive manufacturing of a functionally graded material from Ti-6Al-4V to Invar: Experimental characterization and thermodynamic calculations.* 2017. **127**: p. 133-142.

80. Yoo, S.-W., C.-M. Lee, and D.-H.J.M. Kim, *Effect of Functionally Graded Material (FGM) Interlayer in Metal Additive Manufacturing of Inconel-Stainless Bimetallic Structure by Laser Melting Deposition (LMD) and Wire Arc Additive Manufacturing (WAAM).* 2023. **16**(2): p. 535.

81. Wang, F., S. Williams, and M.J.T.i.j.o.a.m.t. Rush, *Morphology investigation on direct current pulsed gas tungsten arc welded additive layer manufactured Ti6Al4V alloy.* 2011. **57**: p. 597-603.

82. Artaza, T., et al., *Design and integration of WAAM technology and in situ monitoring system in a gantry machine.* 2017. **13**: p. 778-785.

83. Colegrove, P. and S.J.C.U. Williams, *High deposition rate high quality metal additive manufacture using wire+ arc technology.* 2013.

84. Almeida, P. and S. Williams. *Innovative process model of Ti-6Al-4V additive layer manufacturing using cold metal transfer (CMT)*. in *2010 International solid freeform fabrication symposium*. 2010. University of Texas at Austin.

85. Aiyiti, W., et al., *Investigation of the overlapping parameters of MPAW-based rapid prototyping.* 2006. **12**(3): p. 165-172.

86. Pumphrey, T.J.W.D. and Fabrication, *Arc-welding fume control.* 1999. **72**(2): p. 48.

87. !!! INVALID CITATION !!! {}.

88. Moore, K., et al., *Gas metal arc welding control: Part I: Modeling and analysis.* 1997. **30**(5): p. 3101-3111.

89. Wang, H., et al., *Rapid prototyping of 4043 Al-alloy parts by VP-GTAW.* 2004. **148**(1): p. 93-102.

90. Hardy, E.J.N.E.R., *Welding.* 2009. **30**(2): p. 123-137.

91. Hongyuan, S., et al., *Weld formation control for arc welding robot.* 2009. **44**: p. 512-519.

92. O'brien, R., *Welding handbook: welding processes*. Vol. 2. 1987: Woodhead Publishing Limited.

93. Cai, W., et al. *A state-of-the-art review on solid-state metal joining*. in *International Manufacturing Science and Engineering Conference*. 2018. American Society of Mechanical Engineers.

94. Yu, C., et al., *Effect of welding residual stress on plastic buckling of axially compressed cylindrical shells with patterned welds.* 2012. **226**(10): p. 2381-2392.

95. Overlay, C.W.J.L.C., Verhaeghe G., Raghunathan S. Houston: Stainless Steel World America, Texas, *Influence of welding process and parameters on dilution and corrosion resistance/Kumar V.* 2010: p. 64-71.

96. Guo, N., et al., *Effect of rotating arc process on molten pool control in horizontal welding.* 2014. **19**(5): p. 385-391.

97. Weber, A.J.A., *Welding With Digital Controls-New technology allows more precision and less variation.* 2008. **51**(2): p. 44.

98. Bucur, G., A.J.A.o.D. Moise, and Proceedings, *INDUSTRIAL SOLUTION FOR ARC WELDING CONTROL SYSTEM.* 2009.

99. Hu, S.J., E.J.T.M.S.D.H.M. Kannatey-Asibu, Measurement,, and Control, *Assembly and Welding Processes and Their Monitoring and Control.* 2017: p. 8.

100. Chen, B. and S.J.A.A. Chen, *Multi-sensor information fusion in pulsed GTAW based on fuzzy measure and fuzzy integral.* 2010. **30**(3): p. 276-285.

101. Quanying, D., C. Shanben, and L.J.T.I.J.o.A.M.T. Tao, *Inspection of weld shape based on the shape from shading.* 2006. **27**: p. 667-671.

102. Li, Y., C. Su, and J.J.R.i.E. Zhu, *Comprehensive review of wire arc additive manufacturing: Hardware system, physical process, monitoring, property characterization, application and future prospects.* 2022. **13**: p. 100330.

103. Veiga, C., J.P. Davim, and A.J.R.A.M.S. Loureiro, *Properties and applications of titanium alloys: a brief review.* 2012. **32**(2): p. 133-148.

104. Donachie, M.J. and S.J. Donachie, *Superalloys: a technical guide*. 2002: ASM international.

105. Reed, R.C., *The superalloys: fundamentals and applications*. 2008: Cambridge university press.

106. Pandey, S.M., et al., *Study of dry wear behavior and morphological characteristic of 60% Mo-20% NiCr-10% CrC-10% Mo+ Fe based alloy coating by atmospheric plasma spray technique.* 2017. **3**(3): p. 393-406.

107. Mankins, W. and S. Lamb, *Nickel and nickel alloys.* 1990.

108. Dinda, G.P., et al., *Laser aided direct metal deposition of Inconel 625 superalloy: Microstructural evolution and thermal stability.* 2009. **509**(1-2): p. 98-104.

109. Wang, Z., et al., *The microstructure and mechanical properties of deposited-IN718 by selective laser melting.* 2012. **513**: p. 518-523.

110. Huebner, J., et al., *Microstructure of laser cladded carbide reinforced Inconel 625 alloy for turbine blade application.* 2017. **43**(12): p. 8677-8684.

111. Li, S., et al., *Microstructure characteristics of Inconel 625 superalloy manufactured by selective laser melting.* 2015. **31**(9): p. 946-952.

112. Froes, F., R. Boyer, and B. Dutta, *Introduction to aerospace materials requirements and the role of additive manufacturing*, in *Additive manufacturing for the aerospace industry*. 2019, Elsevier. p. 1-6.

113. Sundararaman, M. and P.J.M.c. Mukhopadhyay, *Overlapping of γ' precipitate variants in Inconel 718.* 1993. **31**(4): p. 191-196.

114. Cozar, R. and A.J.M.T. Pineau, *Morphology of y'and y" precipitates and thermal stability of inconel 718 type alloys.* 1973. **4**: p. 47-59.

115. Singh, R., et al., *Evaluating the feasibility of using biodegradable castor oil as a dielectric medium during micro-electrical discharge machining of Inconel 718.* 2023. **32**(14): p. 6465-6477.

116. Gibson, I., et al., *Additive manufacturing technologies*. Vol. 17. 2021: Springer.

117. Strondl, A., et al., *Investigations of MX and γ'/γ "precipitates in the nickel-based superalloy 718 produced by electron beam melting.* 2008. **480**(1-2): p. 138-147.

118. Ramkumar, K.D., et al., *Effect of Mo-rich fillers in pulsed current gas tungsten arc welding of Inconel 718 for improved strength and hot corrosion resistance.* 2017. **26**: p. 5620-5640.

119. Griffith, M.L., et al. *Multi-material processing by LENS*. in *1997 International Solid Freeform Fabrication Symposium*. 1997.

120. Lin, X., et al., *Laser rapid forming of SS316L/Rene88DT graded material.* 2005. **391**(1-2): p. 325-336.

121. Carroll, B.E., et al., *Functionally graded material of 304L stainless steel and inconel 625 fabricated by directed energy deposition: Characterization and thermodynamic modeling.* 2016. **108**: p. 46-54.

122. Sasikumar, R., et al., *Wire arc additive manufacturing of functionally graded material with SS 316L and IN625: Microstructural and mechanical perspectives.* 2022. **38**: p. 230-242.

123. Zhang, J., et al., *Transition Strategy Optimization of Inconel625-HSLA Steel Functionally Graded Material Fabricated by Wire Arc Additive Manufacturing.* 2023. **29**(3): p. 767-776.

124. Rodrigues, T.A., et al., *Wire and arc additive manufacturing of 316L stainless steel/Inconel 625 functionally graded material: development and characterization.* 2022. **21**: p. 237-251.

125. Martina, F., et al., *Microstructure of interpass rolled wire+ arc additive manufacturing Ti-6Al-4V components.* 2015. **46**(12): p. 6103-6118.

126. Martina, F., et al., *Residual stress of as-deposited and rolled wire+ arc additive manufacturing Ti–6Al–4V components.* Materials Science and Technology, 2016. **32**(14): p. 1439-1448.

127. Prado-Cerqueira, J., J. Diéguez, and A.J.P.M. Camacho, *Preliminary development of a wire and arc additive manufacturing system (WAAM).* 2017. **13**: p. 895-902.

128. Paskual, A., P. Álvarez, and A. Suárez, *Study on arc welding processes for high deposition rate additive manufacturing.* Procedia Cirp, 2018. **68**: p. 358-362.

129. Ahsan, M.R.U., et al., *Fabrication of bimetallic additively manufactured structure (BAMS) of low carbon steel and 316L austenitic stainless steel with wire+ arc additive manufacturing.* Rapid Prototyping Journal, 2020. **26**(3): p. 519-530.

130. Ding, D., et al., *Wire arc additive manufacturing of Ti6AL4V using active interpass cooling.* Materials and Manufacturing Processes, 2020. **35**(7): p. 845-851.

131. Ahsan, M.R., et al., *Effects of process parameters on bead shape, microstructure, and mechanical properties in wire+ arc additive manufacturing of Al0. 1CoCrFeNi high-entropy alloy.* 2021. **68**: p. 1314-1327.

132. Senthil, T., et al., *Mechanical and microstructural characterization of functionally graded Inconel 825-SS316L fabricated using wire arc additive manufacturing.* 2021. **15**: p. 661-669.

133. Ghanavati, R., et al., *Additive manufacturing of thin-walled SS316L-IN718 functionally graded materials by direct laser metal deposition.* 2021. **15**: p. 2673-2685.

134. Kim, Y.S., et al., *Bimetallic additively manufactured structure (BAMS) of Inconel 625 and austenitic stainless steel: effect of heat-treatment on microstructure and mechanical properties.* 2022. **121**(11-12): p. 7539-7549.

135. Zhang, R., et al., *Experimental studies on fabricating functionally gradient material of stainless steel 316L-Inconel 718 through hybrid manufacturing: directed energy deposition and machining.* 2022. **120**(11-12): p. 7815-7826.

136. Singh, P.K., S. Kumar, and P.K.J.M. Jain, *Surface Integrity of Cryogenically Finished Additively Manufactured and Conventional Ti-6Al-4V Alloy.* 2023. **13**(4): p. 693.

137. Rathee, S., et al., *Effect of tool plunge depth on reinforcement particles distribution in surface composite fabrication via friction stir processing.* 2017. **13**(2): p. 86-91.

138. Singh, P.K., et al., *Additive Manufacturing Technologies and Post-processing, Design Optimization, and Material Considerations for Reliable Printing.* 2023. **1**: p. 27-52.

139. Hönnige, J.R., P. Colegrove, and S.J.P.e. Williams, *Improvement of microstructure and mechanical properties in wire+ arc additively manufactured Ti-6Al-4V with machine hammer peening.* 2017. **216**: p. 8-17.

140. Santella, M., et al., *Effects of friction stir processing on mechanical properties of the cast aluminum alloys A319 and A356.* 2005. **53**(2): p. 201-206.

141. Pradeep, S., S.K. Sharma, and V. Pancholi. *Influence of friction stir processing parameters on anisotropic behavior property of 5086-o aluminum Alloy*. in *Materials Science Forum*. 2012. Trans Tech Publ.

142. Rhodes, C., et al., *Effects of friction stir welding on microstructure of 7075 aluminum.* 1997. **36**(1): p. 69-75.

143. Kumar, R., et al., *Friction-stir-spot welding of 3D printed ABS and PA6 composites: flexural, thermal and morphological investigations.* 2022. **8**(1): p. 909-916.

144. Mashinini, P.M., D. Hattingh, and H.J.A.M.R. Lombard, *Influence of Process Heat Input on Static and Dynamic Properties of Friction Stir Welded 3mm Ti6Al4V Alloy.* 2014. **1019**: p. 287-293.

145. Dhinakaran, V., et al., *Wire Arc Additive Manufacturing (WAAM) process of nickel based superalloys–A review.* 2020. **21**: p. 920-925.

146. Das, M., et al., *Review on High Performance Nickel based Super Alloy.* 2015. **5**(5): p. 286-291.

147. Kirby, G.N., et al., *The relative effects of chromium, molybdenum, and tungsten on the occurrence of σ phase in Ni-Co-Cr alloys.* 1974. **5**: p. 1477-1494.

148. Ramkumar, K.D., et al., *Investigations on the microstructure, tensile strength and high temperature corrosion behaviour of Inconel 625 and Inconel 718 dissimilar joints.* 2017. **25**: p. 306-322.

149. Singh, R., et al., *On SiC/Al2O3 reinforced HDPE 3D printed rapid tooling.* 2020. **33**: p. 1483-1487.

150. Czan, A., et al. *Analysis of residual stress in subsurface layers after precision hard machining of forging tools*. in *MATEC Web of Conferences*. 2018. EDP Sciences.

151. Rathee, S., et al., *Friction based additive manufacturing technologies: principles for building in solid state, benefits, limitations, and applications*. 2018: CRC Press.

152. Bhardwaj, N., et al., *Recent developments in friction stir welding and resulting industrial practices.* 2019. **5**(3): p. 461-496.

153. Kumar, P., R.K.R. Singh, and S.K.J.P.o.t.I.o.M.E. Sharma, Part C: Journal of Mechanical Engineering Science, *Effect of welding parameters on bead characteristics and mechanical properties of wire and arc additive manufactured inconel 718.* 2023. **237**(7): p. 1668-1691.

154. Rathee, S., et al., *A review of recent progress in solid state fabrication of composites and functionally graded systems via friction stir processing.* 2018. **43**(4): p. 334-366.

155. Siddiquee, A.N. and S.J.T.I.J.o.A.M.T. Pandey, *Experimental investigation on deformation and wear of WC tool during friction stir welding (FSW) of stainless steel.* 2014. **73**: p. 479-486.

156. Xu, F., et al., *Microstructural evolution and mechanical properties of Inconel 625 alloy during pulsed plasma arc deposition process.* 2013. **29**(5): p. 480-488.

157. Zhang, D., et al., *Additive manufacturing of duplex stainless steels-a critical review.* 2022. **73**: p. 496-517.

158. Dokme, F., M.K. Kulekci, and U.J.M. Esme, *Microstructural and mechanical characterization of dissimilar metal welding of Inconel 625 and AISI 316L.* 2018. **8**(10): p. 797.

159. Ng, G., et al., *Porosity formation and gas bubble retention in laser metal deposition.* 2009. **97**: p. 641-649.

160. Yadav, P.C., et al., *Controlled precipitation and recrystallization to achieve superior mechanical properties of severely deformed Inconel 718 alloy.* 2023. **295**: p. 127098.

161. Kumar, S.P., et al., *A review on properties of Inconel 625 and Inconel 718 fabricated using direct energy deposition.* 2021. **46**: p. 7892-7906.

162. Radhakrishna, C. and K.J.J.o.M.S. Prasad Rao, *The formation and control of Laves phase in superalloy 718 welds.* 1997. **32**: p. 1977-1984.

163. Knorovsky, G., et al., *INCONEL 718: A solidification diagram.* 1989. **20**: p. 2149-2158.

VISIBLE RESEARCH OUTPUT

Sr. No.	Title of Paper	Authors	Journal Name	Year or Status
1.	Effect of in-situ cooling during pressure and frictional deformation on mechanical and metallurgical properties of Ni-based functionally graded material developed by wire arc additive manufacturing	Manish Singh, Ratnesh Kumar Raj Singh, Dheeraj Gupta	Proceedings of the Institution of Mechanical Engineers, Part L: Journal of Materials: Design and Applications (SAGE Publications) Impact factor: 2.4	Published (2023) DOI: 10.1177/14644207231183096
2.	Investigation of frictional deformation on mechanical and metallurgical properties of Ni-based Functionally Graded Materials developed by WAAM	Manish Singh, Ratnesh Kumar Raj Singh, Dheeraj Gupta	Proceedings of the Institution of Mechanical Engineers, Journal of Materials Engineering and Performance (SAGE Publications) Impact factor: 2.3	Published (2024) DOI: 10.1007/s11665-024-09136-9
3.	Metallurgical and Mechanical Properties of Trimetallic Functionally Graded Materials Fabricated by Wire Arc Additive Manufacturing	Manish Singh, Ratnesh Kumar Raj Singh, Dheeraj Gupta	Journal of Alloys and Compounds Impact factor: 6.37	Revision submitted
4.	Impact of post-process friction stir processing (FSP) on residual stress in duplex steel deposited using Wire Arc Additive Manufacturing (WAAM)	Manish Singh, Ratnesh Kumar Raj Singh, Dheeraj Gupta		Manuscript ready for submission
5	Investigation of compositional variation on mechanical and metallurgical properties of Ni based FGM developed by GTAW process	Manish Singh, Ratnesh Kumar Raj Singh, Dheeraj Gupta		Manuscript ready for submission

APPENDIX

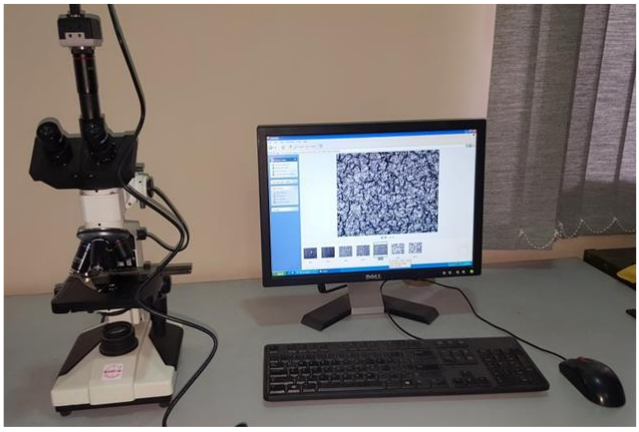

Figure A-1 Optical Microscopy (Make: Radical Scientific Equipment, Model: RMM-8T, Photo Courtesy: Surface Engineering and Tribology Research Lab, Mechanical Engineering Department, TIET, Patiala)

Figure A-2 Scanning Electron Microscopy (Make: Sigma - ZEISS Field Emission SEM, Photo Courtesy: Electron Microscopy laboratory, TIET, Patiala)

Figure A-3 X-Ray Diffractometer (XRD) (Make: SmartLab Rigaku, Japan, Model: SmartLab SE, Photo Courtesy: School of Physics and Materials Science, Thapar Institute of Engineering & Technology)

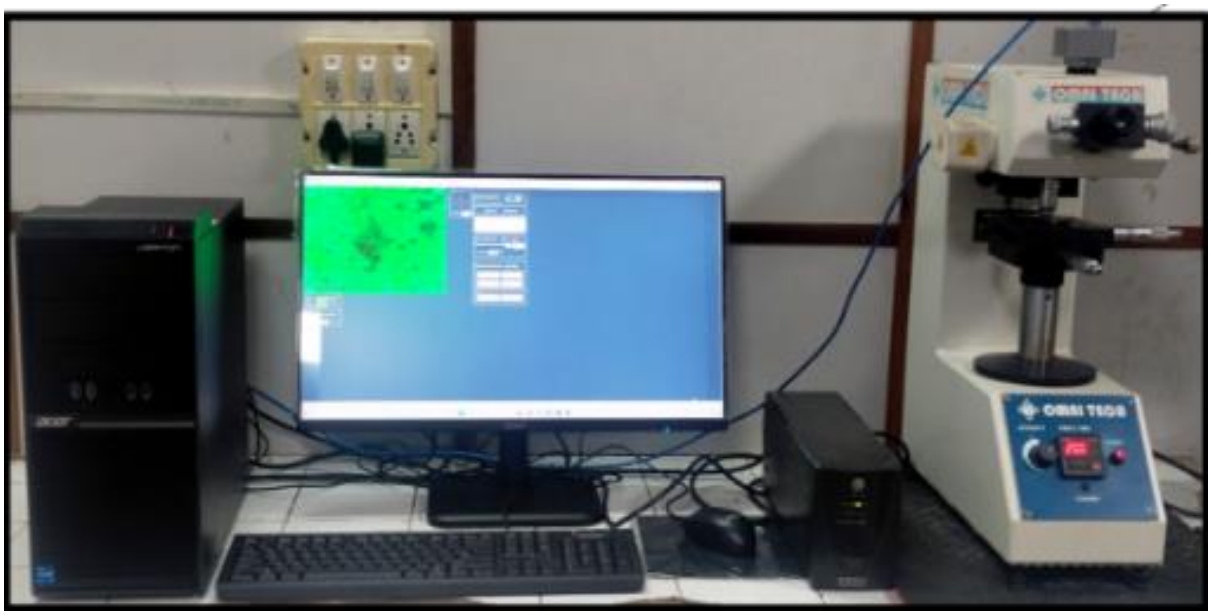

Figure A-4 Vicker's Micro-Hardness Tester (Make: Meta-Tech, Model: MVH1) Photo Courtesy: A.M. Lab, Thapar Institute of Engineering & Technology)

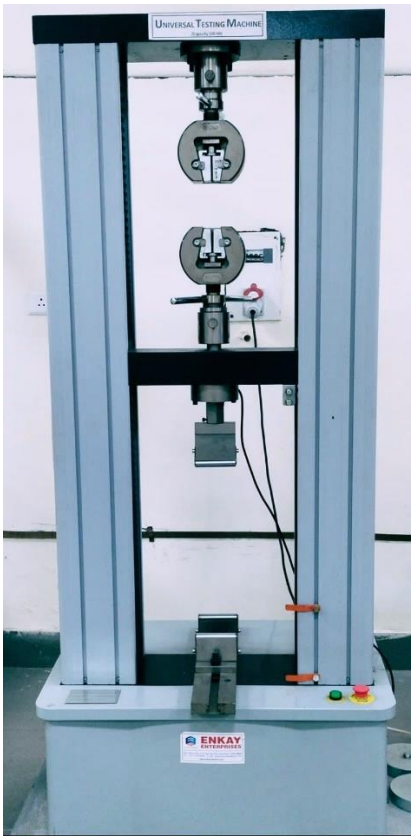

Figure A-5 Universal testing machine (Make: Enkay Enterprises, Model: EKE591 Series) Photo Courtesy: A.M. Lab, Thapar Institute of Engineering & Technology)